

Upconversion Nanoparticles: Stability, Surface Modification and Dye Sensitization

Inaugural-Dissertation
to obtain the academic degree
Doctor rerum naturalium (Dr. rer. nat.)

Submitted to the Department of Biology, Chemistry, Pharmacy
of Freie Universität Berlin

Maysoon Saleh

From
Amman, Jordan

2020, Berlin

This work was done under supervision of
Dr. Ute Resch-Genger
(Bundesanstalt für Materialforschung und -prüfung Berlin)

in the time frame of
June 2017 October 2020

at the
Bundesanstalt für Materialforschung und -prüfung

I hereby declare that this doctoral study was prepared autonomously and that no illegal help was used. Contributions of others, e.g., content, quotes, or figures are indicated by referring to the original work.

Berlin, December 2020_____ Maysoon Saleh

1.) Referee: Dr. Ute Resch-Genger

2.) Referee: Prof. Dr. Siegfried Eigler (FU Berlin)

Disputation at: 29.01.2021

Contents

ACKNOWLEDGEMENTS.....	VI
1. ABSTRACT.....	VIII
2. ZUSAMMENFASSUNG.....	X
3. INTRODUCTION AND MOTIVATION.....	1
3.1 Prologue.....	1
3.2 Motivation and Objectives	2
3.3 Upconversion Nanoparticles (UCNP).....	4
3.3.1 Selection of the Dopant Ions	5
3.3.2 Selection of Efficient Host Inorganic Crystals	4
3.3.3 Upconversion Mechanisms.....	7
3.4 Dye Sensitization of Upconverting Nanoparticles	8
3.4 Synthesis of Upconverting Nanoparticles	9
3.5 Surface Modification of Upconverting Nanoparticles	10
3.6 Silica Coating on Upconverting Nanoparticles.....	10
3.6.1 Coating Upconverting Nanoparticles with a silica shell using a reverse oil-in-water microemulsion method.....	13
3.6.3 Coating Upconverting Nanoparticles with a mesoporous silica shell.....	15
3.7 Stability of Upconverting Nanoparticles and Monitoring their Dissolution in Aqueous Media	16
4. SYNTHESIS, ANALYTICAL METHODS AND TECHNIQUES.....	17
4.1 Synthesis of UCNP	17
4.2 Structural Characterization of UCNP.....	17
4.2.1 Electron Microscopy.....	17
4.2.2 Dynamic Light Scattering (DLS).....	18
4.2.3 Surface Charge	19
4.3 Optical Spectroscopy.....	20
4.3.1 Fluorescence lifetimes	21
4.4 Analytical Measurements.....	22
4.4.1 Inductively Coupled Plasma-Optical Emission Spectrometry (ICP-OES)	22
4.4.2 Fluoride-Ion Selective Electrode (ISE)	23
5. SYNOPSIS OF RESULTS, CONCLUSIONS & OUTLOOK.....	25
6. MANUSCRIPTS: MAJOR CONTRIBUTIONS.....	29
6.1 Sensitization of upconverting nanoparticles with a NIR-emissive cyanine dye using a micellar encapsulation approach	29

6.2 Assessing the Protective Effects of Different Surface Coatings on NaYF ₄ :Yb ³⁺ , Er ³⁺ Upconverting Nanoparticles in Buffer and DMEM	40
7. PUBLICATIONS: MINOR CONTRIBUTIONS	68
7.1 Coating of upconversion nanoparticles with silica nanoshells of 5-250 nm thickness....	68
LIST OF ABBREVIATIONS.....	93
LIST OF PUBLICATIONS.....	95
REFERENCES.....	96

Acknowledgements

This work would not have been done without the help and support of many people. First of all, I would like to express my deepest thanks and gratitude to Dr. Ute Resch-Genger for her supervision throughout my time as a doctoral candidate. I deeply thank her, especially for her great support and stepping by to supervise my doctoral thesis during a time of hardship and hopelessness.

I would also like to thank Prof. Dr. Siegfried Eigler, for accepting to be my second reviewer and for his help and comments. His encouragement, support, fast and easy solutions to problems are highly appreciated.

Thanks are well paid to Prof. Dr. Christina Roth for her stimulating discussions, her encouragement and helpful advice during the preparation of my thesis.

I am deeply grateful to my direct supervisor, Dr. Bastian Rühle, for his great supervision and support during the entire time of my work at BAM. I strongly appreciate the very nice, helpful and interesting scientific discussions and knowledge he always provided generously. I am greatly indebted to him for his understanding, wisdom, patience and empathy.

I would like to thank my collaboration partners. Prof. Dr. Christina Graf and Dr. Cynthia Kembuan from Freie Universität Berlin (FUB), Ihor Panas from the National Academy of Sciences of Ukraine, and Dr. Jörg Radnik from BAM. This thesis benefited from the collaborative work we've done together. Thanks, are also well paid to Anke Schindler from FUB for her efforts in supervising me during the SEM measurements and for her being always there to solve technical problems regarding the SEM, her cooperation made work much easier. I would also like to thank Lydia Alnajjar for her excellent help with all administrative matters starting from registration for a doctoral program until thesis submission.

Many thanks to all colleagues in the Biophotonics group. I would specifically like to thank Maria Richter and Thomas Schneider, for their great assistance in arranging laboratory issues, providing safety instructions and purchases of chemicals. I would also like to thank Dr. Katrin Hoffmann for the positive spirit, help and assistance in administrative and technical

problems, she was a great supporter and very understanding when “last minute help” was needed. Thanks to Dr. Arne Güttler for his assistance, especially with laser safety regulations, and to Janina Roik (division 1.6) for her friendly and nice attitude while performing the ICP-OES measurements.

Thanks to my office mates Melissa Jane Monks, Bettina Grauel and Florian Frenzel for the constructive atmosphere in the office, for the nice daily company, great discussions, interesting times and the “too much coffee” we had together. Not only that you helped me endure the hard times of my PhD, you made being a doctoral candidate at BAM an enjoyable experience.

I am thankful for the time spent with my colleagues, the doctoral candidates: Elina Andresen, Cui Wang, Daniel Kage and Florian Weigert for the nice working atmosphere, interesting small talks and lunch breaks, especially our “Fridays out lunch”. Additionally, I would like to thank my Master student Shu Wang for our work together. I am entirely grateful for two wonderful colleagues that turned out to be close friends, Lorena and Nithiya. Their friendship, companionship, our trips and travels together, cooking and backing evenings are true gifts for me. Thanks for sharing such great memories with me.

To my family in Herford: my cousin Mohamed, his wife Dua’a and their lovely son Albaraa for having me over very often and making me feel like home. I am greatly indebted to you all, and I wish you a lifetime of peace, happiness and success.

Last but not least, my deepest thanks and gratitude to my parents: Ismail and Fakhrieh, for their endless emotional and financial support throughout my entire life. I would have never been the person I am today without their wisdom, warmth and encouragement, which they have been always ready to provide. I feel blessed and privileged to have you two as role models in my life. Mom and Dad, thanks for giving me the best gift and support system, my awesome brothers and sisters: Iyad, Abdulfattah, Nihaya, Nisreen, Mohammad and Yazan to whom I am entirely grateful.

1. Abstract

Lanthanide-based upconversion nanoparticles (UCNP), such as NaYF₄: Yb³⁺/Er³⁺, are inorganic nanocrystals that exhibit upconversion luminescence; a phenomenon that involves emission of higher energy photons upon the excitation of the nanomaterial with lower energy photons. As a result, these particles show distinct non-linear optical properties that make them suitable candidates to be used in applications such as bioimaging, drug release and drug delivery, photovoltaics and biosensing. However, the use of these nanoparticles is still limited due to numerous challenges. Amongst those are the small absorption cross-sections and narrow absorption bands of UCNP along with the relatively low photoluminescence quantum yields. Additionally, the cytotoxicity of these particles is still a matter of investigation with very few research outcomes assessing the biocompatibility of UCNP despite their enormous potential in biological and life science applications. This thesis focusses on new means that can help to tackle these challenges.

One strategy to deal with the first challenge and boost UCNP brightness is sensitization using near infrared (NIR) absorbing and emitting dyes. This strategy was used and is presented in the first project discussed in this thesis. A custom-made NIR dye (1859 SL), synthesized by our collaboration partners, was coupled with NaYF₄: 20%Yb³⁺, 2%Er³⁺ in a micellar encapsulation approach using two different surfactants, namely Pluronic F-127 and Tween 80. The relatively broad absorption band and the strong absorption cross section of the dye made it an ideal light harvester and energy donor for UCNP. The optimum ratio of dye to UCNP and the best value of excitation power density for the measurements were investigated by measuring the luminescence intensity for systems with different particle to dye ratios, and at variable excitation power densities.

In the second project, dissolution of UCNP in aqueous media was investigated as a possible source for toxicity of UCNP due to the release of fluoride and lanthanide ions. Investigation of the ability of surface passivation and silica coating to inhibit ions release from the UCNP surfaces was studied. UCNP dissolution was quantified electrochemically using a fluoride ion selective electrode (ISE) and by inductively coupled plasma optical emission spectrometry (ICP OES) that provided the amount of released fluoride and lanthanide ions respectively. In

addition, dissolution was monitored fluorometrically. The chemical composition of the aqueous environment on UCNP dissolution has a critical influence. For example, the formation of a layer of adsorbed molecules (organic compounds constituting DMEM, such as aminoacids) on the UCNP surface was observed for particles aged in a cell medium (DMEM). This layer protected the UCNP from dissolution and enhanced their fluorescence. X-ray photoelectron spectroscopy (XPS) and mass spectrometry (MS) were used to investigate the chemical nature of this layer. This outcome offers a very practical and biocompatible mean for inhibiting ions release from UCNP, which is a cause of cytotoxicity of the particles.

In a third project carried out in collaboration with the group of Prof. Christina Graf (FUB), a new, simple approach for growing a silica shell with an adjustable thickness between 5 and 250 nm onto oleate coated UCNP was investigated. Two different synthesis methods were combined to achieve that: oil-in-water microemulsion synthesis, and Stöber-like synthesis. Firstly, this method included the growth of silica on the oleate-coated particles in a multi-step reverse microemulsion reaction performed consecutively without the need for intermediate isolation or purification steps. Then the particles were isolated and further grown in one step up to a diameter of more than 500 nm in a modified Stöber process. The importance of this procedure is due to its ability to grow thick silica shells (of thicknesses larger than 50 nm) onto the hydrophobic UCNP, which could not have been achieved using either of the two synthesis methods separately. The methods used to confirm the silica shell thickness and quality of the UCNP@SiO₂ systems included dynamic light scattering (DLS), zeta potential measurements and scanning electron microscopy (SEM).

2. Zusammenfassung

Aufkonvertierungs-Nanopartikel (UCNP) sind nanoskalige Partikel, die eine Aufkonvertierungslumineszenz aufweisen; ein Phänomen, das die Emission von Photonen höherer Energie bei der Anregung des Nanomaterials mit Photonen niedrigerer Energie beschreibt. Dies verleiht den Partikeln besondere optische Eigenschaften die sie zu interessanten Kandidaten für Anwendungen wie Bildgebungsverfahren, Wirkstofffreisetzung und -abgabe, Photovoltaik und Biosensoren machen. Die Verwendung dieser Nanopartikel ist jedoch aufgrund einer Reihe von Herausforderungen noch begrenzt. Dazu gehören der geringe Absorptionsquerschnitt und die schmalen Absorptionsbanden von UCNP zusammen mit den relativ niedrigen Photolumineszenzquantenausbeuten. Darüber hinaus ist die Zytotoxizität dieser Partikel noch Gegenstand von Untersuchungen, und trotz ihres enormen Potentials in biologischen Anwendungen liegen momentan nur sehr wenige Forschungsergebnisse zur Bewertung der Biokompatibilität von UCNP vor. In dieser Arbeit werden verschiedenen Möglichkeiten untersucht die dabei helfen können, diese Herausforderungen anzugehen.

Eine der Strategien die angewandt werden können um die UCNP-Helligkeit zu Erhöhen und somit der ersten Herausforderung zu begegnen ist die Sensibilisierung mit absorbierenden und emittierenden Farbstoffen im nahen Infrarotbereich (NIR). Diese Strategie wird im ersten in dieser Arbeit vorgestellten Projekt beschrieben. Ein für diese Anwendung gezielt synthetisierter NIR-Farbstoff (1859 SL) wurde mit $\text{NaYF}_4: 20\% \text{Yb}^{3+}, 2\% \text{Er}^{3+}$ in einem mizellaren Verkapselungsansatz unter Verwendung von zwei verschiedenen Tensiden, nämlich Pluronic F 127 und Tween 80 gekoppelt. Die relativ breite Absorptionsbande und der große Absorptionsquerschnitt des Farbstoffs machen ihn zu einem idealen Lichtsammler und Energiedonor für UCNP. Das optimale Verhältnis von Farbstoff zu UCNP und die optimale Leistungsdichte für die Messungen wurden durch Messung der Lumineszenzintensität für Systeme mit unterschiedlichem Partikel-zu-Farbstoff-Verhältnis und variablen Leistungsdichten untersucht.

Im zweiten Projekt wurde die Auflösung von UCNP in wässrigen Medien als mögliche Quelle für die Toxizität von UCNP aufgrund der Freisetzung von Fluorid- und Lanthanid-

Ionen untersucht. Untersucht wurde die Fähigkeit die Ionenfreisetzung von den UCNP-Oberflächen durch Oberflächenpassivierung oder -beschichtung mit Siliziumdioxid zu hemmen. Die UCNP-Auflösung wurde elektrochemisch mit einer fluoridionenselektiven Elektrode (ISE) und durch optische Emissionsspektrometrie mit induktiv gekoppeltem Plasma (ICP OES) quantifiziert, die jeweils die Menge der freigesetzten Fluorid- bzw. Lanthanidionen lieferten. Darüber hinaus wurde die Auflösung fluorometrisch untersucht. Die chemische Zusammensetzung der wässrigen Umgebung hat einen entscheidenden Einfluss auf die UCNP-Auflösung. Bei den in einem Zellmedium (DMEM) gealterten Partikeln wurde die Bildung einer Schicht aus adsorbierten Molekülen auf der UCNP-Oberfläche beobachtet. Diese Schicht schützte die UCNP vor Auflösung und verstärkte ihre Lumineszenz. Mit Hilfe der Röntgen-Photoelektronenspektroskopie (XPS) und der Massenspektrometrie (MS) wurde die chemische Natur dieser Schicht untersucht.

In einem dritten Projekt, das in Zusammenarbeit mit der Gruppe von Prof. Christina Graf (FUB) durchgeführt wurde, wurde ein neuer, einfacher Ansatz für das Aufwachsen einer Siliziumdioxidhülle mit einer einstellbaren Dicke zwischen 5 und 250 nm auf ölsäurebeschichteten UCNP untersucht. Diese Methode beschreibt das Wachstum von Siliziumdioxid auf den mit Oleat beschichteten Partikeln in einer mehrstufigen inversen Mikroemulsion, die nacheinander ohne Isolations- oder Reinigungsschritte der Zwischenprodukte durchgeführt werden kann. Anschließend wurden die Partikel isoliert und in einem weiteren Schritt bis zu einem Durchmesser von mehr als 500 nm in einem modifizierten Stöber-Prozess vergrößert. Die Methoden zur Bestätigung der Siliziumdioxid-Schalendicke und -qualität der UCNP@SiO₂-Systeme umfassten dynamische Lichtstreuung (DLS), Zetapotentialmessungen und Rasterelektronenmikroskopie (REM).

3. Introduction and Motivation

3.1 Prologue

Science has always striven to explain universal phenomena, explore new discoveries, address problems or challenges and then come up with practical solutions to ease life for humanity. In modern life, humanity made great advancements in important fields such as medicine, technology and renewable energy. In the last decades, nanomaterials science has been largely contributing to the advancements of these fields. Due to their small size, nanomaterials have different properties (such as surface plasmon resonance in some metal particles and superparamagnetism in magnetic materials) than their bulk counterparts due to the high surface area to volume ratio and possible appearance of quantum effects at the nanoscale. These properties are determined by parameters such as size, shape, composition or crystalline structure. Tuning these parameters allows the control of the nanomaterial properties and their manipulation to obtain materials that best fit the desired application. Thus, nanomaterials could be used in a wide range of applications in important fields such as medicine, biotechnology and catalysis.

Various types of organic, inorganic and hybrid nanoparticles such as polymer, carbon, metal or metal oxide nanoparticles have been made and used in various applications in different fields, such as: photonics, electronics, chemical sensors, biological sensors, energy storage, and catalysis. In the last two decades, a new family of rare earth metal oxide or fluoride nanoparticles has been synthesized and thoroughly investigated. These nanoparticles are called upconversion nanoparticles (UCNP), because they are capable of performing photon upconversion. Photon upconversion (UC) refers to the excitation of the nanomaterial with lower energy photons, which leads to the emission of higher energy photons (anti-Stokes emission) via intermediate excited electronic states.¹⁻³

Francis Auzel was the first to explain the phenomenon of photon UC for bulk materials in 1966.⁴ High UC efficiencies even at room temperatures were observed for lanthanide-doped solids. Further research was done, until Menyuk *et al.* introduced the most efficient UC phosphor to date: Yb³⁺- and Er³⁺- doped NaYF₄ in 1972.⁵ After that, it was not until the end of

1990s and beginning of 2000s that UC nanometer-sized materials were synthesized.⁶⁻⁸ The aim was to synthesize small upconverting nanocrystals with high luminescence efficiency that form transparent solutions in a wide range of solvents, which enables them to be used in a variety of applications, as outlined below.

Transferring the energy of light from lower energy photons to higher energy photons has many distinct applications and offers many possibilities. Amongst those are the use of UCNP in solar cells,⁹⁻¹⁴ security and barcoding,¹⁵ light emitting diodes (LEDs) and displays,¹⁶⁻¹⁸ and high resolution microscopy.¹⁹⁻²¹ UCNP are commonly excited using commercially available 808 or 980 nm continuous-wave diode lasers. Those excitation wavelengths lie in the biological optical window (650 – 1200 nm) within which living tissues absorb relatively little light compared to shorter and longer wavelengths.²² This range of excitation is behind the use of UCNP in biological applications, such as bioimaging,^{23, 24} *in-vitro* and *in-vivo* detection of biomolecules,²⁵⁻²⁸ drug delivery,²⁹ photodynamic therapy^{23, 24, 30, 31} and biosensing.^{30, 32}

3.2 Motivation and Objectives

UCNP are of increasing importance for a wide range of applications, for example, in bioanalytical, diagnostic, and sensing applications as well as photovoltaic and security applications. To fully utilize the application potential of UCNP, a number of challenges have to be overcome. Amongst those is the low brightness of UCNP, especially for small UCNP (those with diameters below 20 nm). Two main strategies can be followed to improve the brightness of UCNP. The first one is to enhance upconversion luminescence (UCL) by minimizing non-radiative deactivation pathways. The second one is to boost the absorption cross section/excitation efficiency, either by UCL sensitization using near infrared (NIR) dyes, or by coupling a plasmonic structure such as applying a gold or a silver nanoshell to the UCNP surface to enhance the absorption and emission processes. However, the latter requires a dielectric spacer, such as a silica shell, to be present between the UCNP and the metal shell to avoid surface quenching that can occur due to the multiple absorption bands exhibited by the metal shells. Although silica coating on nanomaterials has been thoroughly investigated in the literature, tuning the shell thickness and especially growing a thicker silica shell is still challenging.

Finally, the use of nanomaterials in bioanalytical applications requires biocompatible particles that are sufficiently stable in diluted dispersions and have no acute or chronic toxicity under application-relevant conditions. In the case of UCNP, this implies that they should not release potentially toxic constituents such as fluoride and lanthanide ions.

The work discussed in this thesis has three main objectives to tackle some of the challenges, limitations, and open questions mentioned above:

1. Enhancing UCL by NIR dye sensitization of UCNP
2. Monitoring the dissolution behavior of UCNP in aqueous environments
3. Optimizing the coating process of UCNP with silica

Aiming at enhancing the brightness of UCNP, dye sensitization of UCNP using a custom-made NIR dye (1859 SL),³³ synthesized by our collaboration partners (research group of Prof. Yuri L. Slominskii), was investigated and is presented in section 6.1. This dye has an emission spectrum that overlaps well with the absorption bands of the UCNP, which lead to an enhancement in fluorescence intensity. Dye-UCNP systems are obtained by a new, simple, experimentally easy and inexpensive approach by encapsulating the dye molecules in a micelle surrounding hydrophobic oleate-stabilized core-only UCNP with the aid of two different surfactants.

The second objective is presented in section 6.2. The ability of surface passivation and coating techniques to inhibit ions release from the UCNP surfaces was investigated. UCNP release fluoride and lanthanide ions when dispersed in aqueous media, and since these ions are toxic (especially fluoride ions), their release from the particles limit the use of UCNP in biological applications. A systematic study of the stability of UCNP with different surface chemistries under various application-relevant conditions was investigated and monitored, in order to come up with possible solutions to protect the particles from dissolution.

Section 7.1 deals with the third objective and presents a new approach for growing a silica shell with an adjustable thickness between 5 and 250 nm onto oleate coated UCNP. This approach was based on the use of a combination of two synthesis methods: oil-in-water microemulsion and Stöber-like synthesis. The aim was to develop a method for coating UCNP

with thick silica shells, that should also be applicable to other nanoparticles with hydrophobic surfaces regardless of their chemical composition.

3.3 Upconversion Nanoparticles (UCNP)

UCNP are doped nanocrystals in which trivalent lanthanide ions are incorporated into an inorganic lattice with a diameter of less than 100 nm in all three dimensions.³⁴ UCNP are distinct to other luminescent materials by their ability to perform upconversion (UC): the conversion of near infrared (NIR) light to ultraviolet (UV) or visible light. The selection of the host material and the dopant ions determine the UC efficiency, excitation energy as well as the energy of the emitted photons.^{1, 32, 34} Usually, two types of dopant ions are used; the first one is a sensitizer, which is excited upon NIR light absorption and consequently transfers the energy to the second ion, the activator ion, that emits photons with higher energy than the excitation energy. To achieve efficient UC, certain requirements must be met by the inorganic host crystal and the lanthanide dopant ions. These requirements are discussed in the following sections.

3.3.1 Selection of Efficient Host Inorganic Crystals

UCNP are composed of activator and sensitizer ions doped in a host crystal. This implies that the choice of the host crystal determines the distance between the dopant ions and their spatial position.³⁴ Moreover, the host crystal affects the UC efficiency in two main ways: a) by the phonon dynamics and b) by the local crystal field.³⁵ Phonon induced nonradiative processes are the main loss mechanism for UC emission, hence, hosts that possess low phonon energies minimize nonradiative processes and consequently produce more emissive UCNP.^{2, 32, 34} The crystal field of the host material influences the UC efficiency by perturbing the parity forbidden f-f transitions making them partially allowed. A low-symmetry host crystal is preferred as the intermixing of the f states with higher electronic configurations can be more significant.³² The UC efficiency of the hexagonal (β) phase NaYF₄ is higher than that of the cubic (α) phase NaYF₄. For example, the UC efficiency of the green emission in β -NaYF₄:Yb³⁺/Er³⁺, is approximately 10 times stronger than that in cubic α -NaYF₄:Yb³⁺/Er³⁺.^{2, 3}

In summary, optimal host materials should be transparent to NIR light, have low phonon energies, strong crystal fields, lower symmetry of the crystal phase and be chemically

stable.^{2, 32, 36} Hosts containing cations with similar ionic radii to those of the lanthanide dopant ions reduce crystal defects, and consequently reduce the quenching of UCL. Metal oxides are chemically stable and can be used to produce UC materials, but their relatively high cutoff phonon energies, in the range of 500-900 cm^{-1} for Y_2O_3 ,³⁷ ZrO_2 ,³⁸ and YVO_4 ,³⁹ reduce the UC efficiency due to a higher rate of nonradiative processes. Rare earth fluorides on the other hand, which exhibit the lowest phonon cutoff energy amongst the investigated hosts ($\sim 350 \text{ cm}^{-1}$), showed the highest UC efficiency and for this reason, hosts such as NaYF_4 are most frequently used in recent studies.

3.3.2 Selection of the Dopant Ions

The dopant ions are optically active centers, i.e., are capable of absorbing photons and subsequently emitting light. UC occurs in systems having multiple real, long-lived intermediate states, in which the low-energy excitation photons can accumulate and perform UC. If the gaps between three or more energy levels are very similar, successive excitation to a highly excited state is feasible with a laser light source, given that each absorption step requires the same photon energy. Although UC can be achieved by systems containing some of the d block elements such as Ti^{2+} ,^{40, 41} Ni^{2+} ,^{42, 43} Mo^{3+} ,^{44, 45} Re^{4+} ,^{44, 46} or Os^{4+} ,⁴⁷ the most efficient reported UC processes occur with trivalent lanthanide ions due to their distinguished properties,³⁴ such as:

- They possess a multitude and “ladder-like” energy levels.
- The f-f transitions are Laporte forbidden. As a consequence, they generally exhibit low molar absorption coefficients and their excited states are long-lived (up to 0.1 seconds).³
- The 4f electrons in lanthanide ions are shielded by the fully occupied $5s^2$, $5p^6$ and $6s^2$ shells. This shielding is responsible for sharp and narrow 4f-4f transition bands.

Amongst the lanthanide ions, Er^{3+} , Tm^{3+} and Ho^{3+} are mostly used as activators due to their ability to generate visible optical emissions under low power densities (approximately 10 W/cm^2).³⁰ Nanoparticles containing a single dopant lanthanide ion are capable of performing UC and have been initially investigated.^{48, 49} Single-doped UCNP, however, are limited by the low absorption of the exciting light since the 4f-4f transitions are parity forbidden. A higher concentration of the activator could be used to increase absorption, but the range of efficient dopant concentration is limited by cross-relaxation processes. Hence, the

addition of a second lanthanide ion (sensitizer) with a larger absorption cross-section in the NIR spectral region than that of the activator ions can be used to increase the UC efficiency. The most frequently used lanthanide sensitizer is the trivalent Ytterbium ion (Yb^{3+}), which constitute a simple two energy level system, and has a large absorption cross-section at wavelengths around 975 nm. Moreover, the energy difference between the ground state of Yb^{3+} ($^2\text{F}_{7/2}$) and its excited state ($^2\text{F}_{5/2}$) matches well the energy separations in many sensitizer ions such as Er^{3+} and Tm^{3+} .⁵⁰ A schematic illustration of the energy transitions between the sensitizer and the activator, and the UC emission is shown in **Figure 1**. The type and concentration of lanthanide dopants affect the UC efficiency and the emission lines of the resulting UCNP. For example, Er^{3+} emits two photons in the green region of the electromagnetic spectrum and one photon in the red region, while Tm^{3+} emits light in the blue region. Tuning the colors of the emission bands is realized by changing the type or concentration of the dopant ions, controlling the size of the UCNP, controlling the relaxation processes induced by photons of the surrounding ligands, designing different core/shell systems and using resonance energy transfer mechanisms between the UCNP and e.g., coupled organic dyes or quantum dots.^{2, 32}

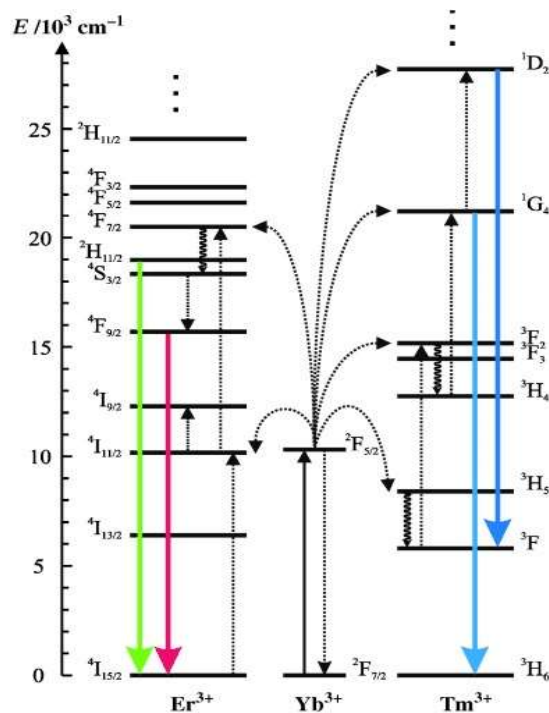


Figure 1: Energy level diagram showing the excitation and emission lines for a system containing Yb^{3+} ions as sensitizers and Er^{3+} and Tm^{3+} as activators. The solid black arrow indicates the excitation of Yb^{3+} by a 980 nm laser, the dotted arrow indicate nonradiative energy transfer and multiphonon relaxation processes. Green, red and blue solid arrows indicate the corresponding visible upconversion emission. Reproduced with permission from (Advanced Materials, 2004, 16, 2102-2105) Copy-right Wiley-VCH 2004. License number: 4871900950470

3.3.3 Upconversion Mechanisms

UC requires the population of electrons in a metastable excited state of the activator ion in order to enable sequential absorption of photons to further excite the electron to a higher excited state using the same excitation laser source, and thus the same excitation wavelength. Several mechanisms are possible for achieving UC, such as: excited-state absorption (ESA), energy transfer upconversion (ETU), cooperative sensitization upconversion (CSU), cross relaxation (CR) and photon avalanche (PA).^{2, 3, 15, 32, 34} **Figure 2** shows schematic diagrams of the energy transfer pathways involved in each mechanism. However, ESA and ETU mechanisms are most relevant for the UC processes in NaYF₄: Yb³⁺, Er³⁺ nanoparticles, which are the particles of interest in this thesis, and for this reason, only those two mechanisms are discussed here in more detail.

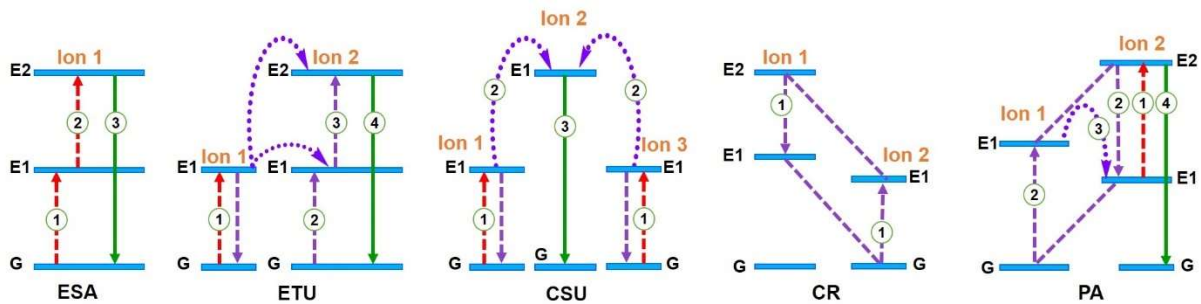


Figure 2: Mechanisms of upconversion processes, the red dotted arrows represent photon absorption, green solid arrows represent photon emission, the purple dotted-curved arrows represent the photon transfer to adjacent ions. The symbols “G, E1 and E2” represent the ground state, the first excited state and the second excited states, respectively. Ion 1 is commonly called the sensitizer while Ion 2 is the activator, Ions 1 and 3 in CSU could be the same type of ion and/or different types of ions. Reproduced from Chem. Rev. 2014, 114, 5161-5214.

a. Excited-State Absorption (ESA)

This is the simplest UC mechanism, in which the sequential absorption of two (or more) photons within the activator ion is responsible for the UC emission. This mechanism requires a ladder-like energy separation (equal separation) from the ground state and the first excited state and from the first excited state to the second excited state as well as a long lifetime of the intermediate excited state. This mechanism explains UC in singly doped UCNPs with very dilute concentrations of the activator, so that the energy transfer between the two activators can be neglected. The most commonly used activators, Er³⁺, Ho³⁺ and Tm³⁺, fulfill these requirements.^{2, 32, 34}

b. Energy Transfer Upconversion (ETU)

In ETU, the UC emission is induced by the energy transfer between a sensitizer and an activator. The sensitizer is first excited from the ground state to its meta-stable first excited state by absorbing a pump photon. Then, it transfers its energy non-radiatively either to the ground state of the sensitizer or to the first excited state of the activator. The electron is then again excited to the second excited state of the activator. The UC efficiency in ETU depends on the distance between the sensitizer and the activator.

3.4 Dye Sensitization of Upconverting Nanoparticles

One of the main limitations of UCNP is the small absorption cross section (10^{-20} cm²)⁵¹ due to parity-forbidden 4f-4f transitions⁵² together with the narrow absorption bands. Moreover, their photoluminescence quantum yields are relatively low and depend on excitation power density as well as the surface-to-volume ratio.^{53, 54} NIR dyes coupled to UCNP can provide a potential strategy to boost UCNP brightness, i.e., the product of the molar absorption coefficient or cross section and the photoluminescence quantum yield.^{15, 32, 55} The relatively broad absorption bands and the high molar absorption coefficients of organic dyes render them ideal light harvesters and energy donors for UCNP.^{52, 56} Moreover, these dyes can also help to shift the excitation of the dye-UCNP systems from 980 nm for Yb-doped UCNP to approximately 800 nm, which fits better into the biological spectral window and prevents heating effects that are caused by the strong absorption of water at 980 nm.⁵⁷

Dye sensitization of UCNP can occur via the Förster mechanism (through the electrostatic interactions between a donor and an acceptor presented as point dipoles) and/or the Dexter mechanism (involving the bilateral exchange of electrons between donor and acceptor in a spin-conserved singlet-singlet or triplet-triplet transfer) from light harvesting organic dyes located directly at or in the immediate vicinity of the UCNP surface across the organic/inorganic interface to the optically active lanthanide ions incorporated in the UCNP.⁵¹ The latter mechanism is significant only at very short donor-acceptor distances (~ 10 Å or less), while electrostatic interactions can occur over longer distances (10–100 Å). The dyes and UCNP can be brought together by modification of the UCNP surface,^{58, 59} modification of the dye,^{58, 60, 61} covalent binding,⁶² or encapsulation in a micelle.⁶³ The first successful attempt of

dye sensitized UC was reported by Zou *et al.*⁶⁰ The dye IR-806, which is a carboxylic acid derivative of the commercially available dye IR-780, was attached to UCNP by replacing the oleylamine ligands on the as-synthesized oleylamine-coated UCNP. Upon excitation at 800 nm, this dye-UCNP system produced the typical (UCL) spectrum of Yb, Er co-doped materials with the green and red Er³⁺ emission bands. This initiated an increasing number of studies of dye-UCNP systems prepared by attaching NIR dyes to UCNP with different ligand functionalities.^{51, 52, 56, 58} In this thesis, dye sensitization of UCNP using the NIR dye (1859 SL) (see **Figure 3**) was investigated as a possible strategy to boost UCNP brightness, the results are discussed in more detail in section 6.1.

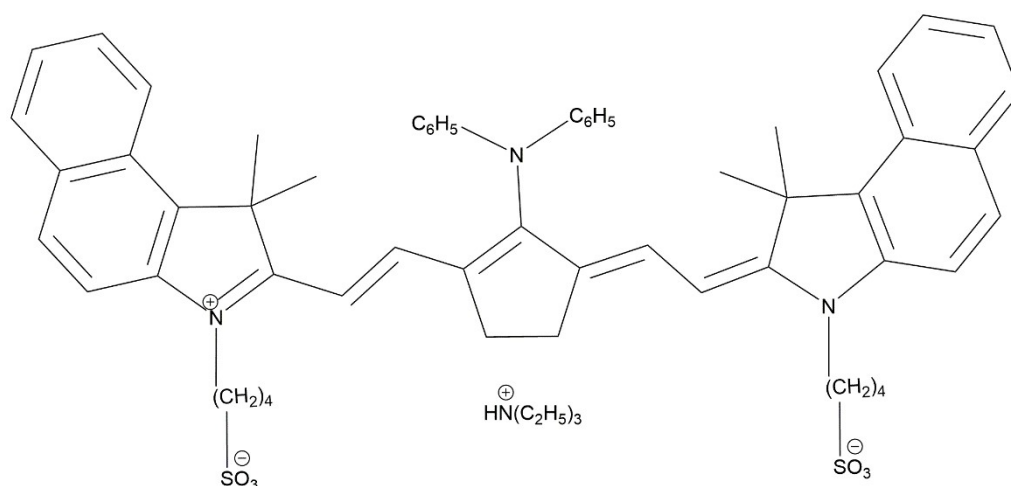


Figure 3: The chemical structure of the dye (1859 SL)

3.4 Synthesis of Upconverting Nanoparticles

A variety of synthetic methods have been developed in the last two decades to synthesize efficient and monodisperse UCNP with controlled size. The choice of the synthesis method affects the produced nanoparticles' size, crystallinity, and monodispersity. The type of the stabilizing ligands on the surface determines the polarity of the nanoparticles surface and hence, the solvents in which they can be re-dispersed.

Several synthesis methods have been used and reported in the literature, such as: co-precipitation⁵, hydro(solvo-)thermal synthesis⁶⁻⁸, thermal decomposition⁹⁻¹⁴, ionic liquid-based synthesis¹⁵ and microwave synthesis.¹⁶ Amongst those, the thermal decomposition

method is superior with respect to narrow particle size distributions, crystal phase purity and optical properties.⁶⁴

The work discussed in chapters 6 and 7 of this thesis is based on the use of NaYF₄:20%Yb³⁺, 2%Er³⁺ UCNP that are synthesized following a general procedure for the synthesis of monodisperse nanoparticles using thermal decomposition with minor modifications.^{18, 65-67} A more detailed description of the synthesis is presented in chapter 4.

3.5 Surface Modification of Upconverting Nanoparticles

The use of UCNP in biological applications requires water dispersible particles. However, the most common and efficient synthetic routes for their formation use high boiling organic solvents, producing hydrophobic particles. Consequently, the as-synthesized UCNP must be further modified to obtain water dispersible and colloidally stable particles.

Several procedures have been developed and used so far to change the hydrophobic UCNP into hydrophilic, stable UCNP,⁶⁸ mainly: ligand exchange and silica encapsulation of UCNP. A very common and reliable procedure for ligand exchange is to initially remove the original ligand (usually oleate for UCNP) forming “naked” UCNP and then coat them with a hydrophilic organic ligand. Dong. *et. al.* used nitrosonium tetrafluoroborate (NOBF₄) to replace the oleate ligand and then stabilized the nanocrystals in a hydrophilic solvent such as N,N-dimethylformamide (DMF).⁶⁹ The obtained hydrophilic UCNP can be further coated with a variety of organic ligands such as polyacrylic acid (PAA),⁷⁰ citrate or PEO-10-OH-terminated phosphonic acid (PEG-PA). Additionally, silica coatings have been used to render UCNP water dispersible.^{71, 72} This also enables further surface functionalization, such as the covalent attachment of fluorescent dyes for biotechnological applications,⁷³ or the specific modification of silica nanoparticles for targeted drug delivery⁷⁴ or for their use as biosensors.⁷⁵

3.6 Silica Coating on Upconverting Nanoparticles

Depending on the applied coating procedure, two different morphologies of silica can be produced; a mesoporous or a microporous silica shell. The difference between both is in the pore size, which is defined as the distance between two opposite walls of the pore, i.e., the diameter in case of cylindrical pores or the width in case of slit-shaped pores. According to the

recommendations of the international union of pure and applied chemistry (IUPAC), pores that have widths larger than 50 nm are considered macropores, pores that have widths between 2 and 50 nm are considered mesopores, while pores that have widths smaller than 2 nm are considered micropores.⁷⁶ Advancements in the synthesis of silica nanoparticles and the coating processes of nanoparticles with silica shells allow for precise tailoring of the morphology, surface chemistry and shell thickness of silica according to the desired application. While silica coating in general enables further surface functionalization such as the covalent attachment of biomolecules and sensor molecules, a highly porous silica surface is beneficial for many life science applications.^{24, 29, 34, 77, 78}

The growth mechanism of colloidal particles explained by LaMer in 1950 plays an essential role in many syntheses of monodisperse nanoparticles.⁷⁹ Based on his theory, it became clear that the synthesis of monodisperse nanoparticles requires fast nucleation and slow growth. Although the growth of core-shell particles was not explained by LaMer's theory, the theory can still help to qualitatively estimate the optimal reaction conditions for the silica coating on nanoparticles.⁸⁰ The formation of nanoparticles includes three stages: monomer concentration, nucleation, and growth (see **Figure 4**). Applying that to UCNP coating with silica, the first step is the supply and hydrolysis of the silica precursor tetraethylorthosilicate (TEOS). The concentration of the hydrolyzed TEOS increases until the solution reaches a state of supersaturation. Once the concentration of the monomer exceeds the heterogeneous nucleation threshold, nucleation on the surface of the UCNP occurs. If the concentration of the monomer is increased even further and exceeds the homogeneous nucleation threshold, then homogenous nucleation will occur forming small silica nanoparticles ("secondary nucleation") resulting in a mixture of core-shell particles and small silica nanoparticles. To avoid that, the concentration of the silica precursors needs to be adjusted to stay above the heterogeneous nucleation threshold, but below the homogeneous nucleation threshold. Fractional addition of small amounts of TEOS over a long period of time can be used to stay below the homogeneous nucleation threshold and grow a thicker silica shell on preexisting nanoparticle cores.⁸⁰

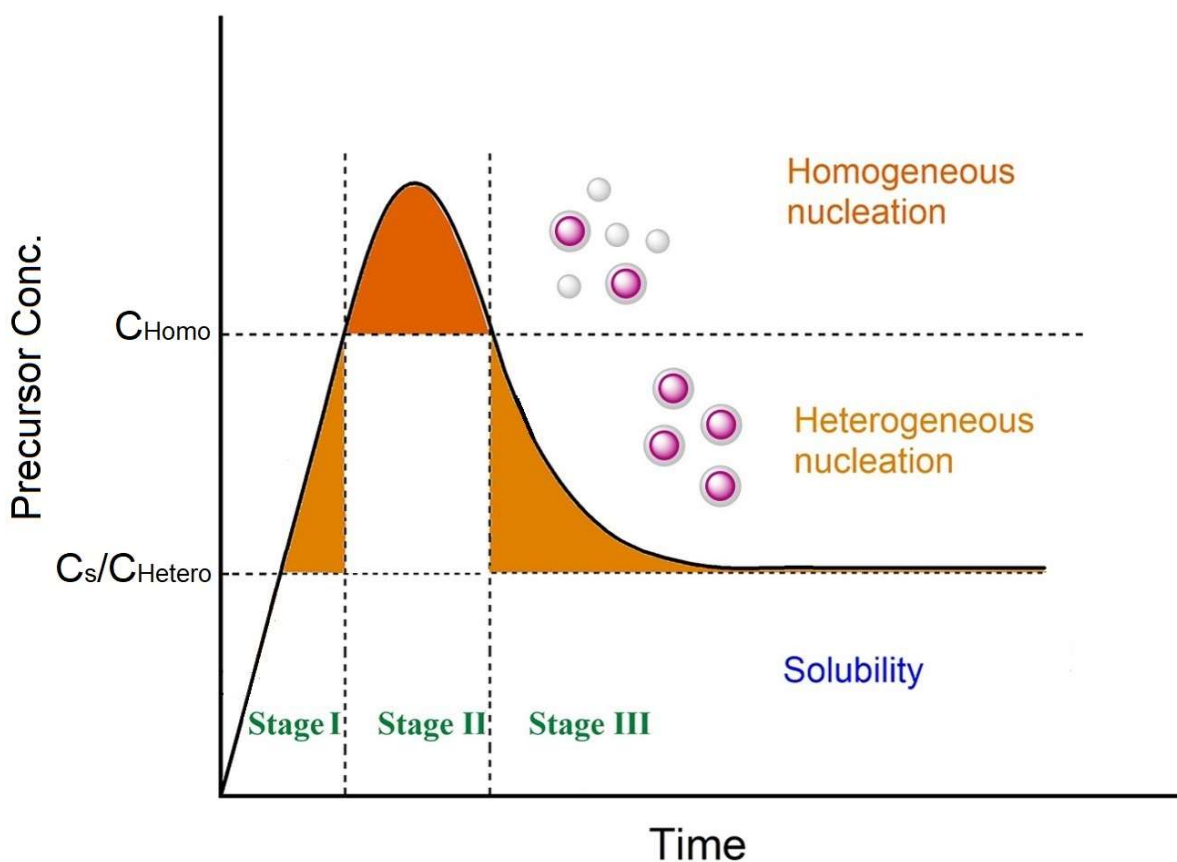
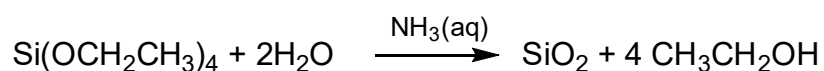


Figure 4: La Mer-like diagram showing the effect of hydrolyzed TEOS concentration against time on homogeneous nucleation and heterogeneous nucleation. (Interpreted from J. Am. Chem. Soc. 1950, 72, 11, 4847-4854)

The formation of silica occurs through an S_N2 reaction mechanism. In this process, an alkoxy silane (most often tetraethylorthosilicate (TEOS)) is first hydrolyzed and then condensed to form silica nanoparticles. The reaction takes place in an ethanolic solution under the catalytic action of ammonia, according to the following equation:



Within the scope of this work, UCNP coating with silica was used in section 6.2 to investigate the protection effects of silica shelling on the surface of the particles, and hence decreasing ion release. Mesoporous and microporous silica shells were applied, and their effects were investigated. Furthermore, silica coating was the main focus of section 7.1. Here, a procedure for coating UCNP with a silica shell of adjustable thickness was developed. Two different

syntheses methods were combined to achieve that: oil-in-water reverse microemulsion synthesis, and Stöber-like synthesis.

3.6.1 Coating Upconverting Nanoparticles with a silica shell using a reverse oil-in-water microemulsion method

The word “microemulsion” was first proposed by Schulman in 1959 after several years of investigations of transparent solutions resulting from mixing two liquids of different polarity by the aid of a surfactant and a cosurfactant, which he first described as transparent water-in-oil dispersions.^{81, 82} A microemulsion is an isotropic, macroscopically homogeneous and thermodynamically stable solution containing at least three components: a polar phase, a nonpolar phase and a surfactant. The reverse water-in-oil microemulsion method is based on mixing a surfactant in an organic solvent with or without the addition of water, forming aggregates that are called reverse micelles.

The formation of the microemulsion can be either in the form of oil-swollen micelles dispersed in water, so-called “oil-in-water microemulsion (O/W)”, or water-swollen micelles dispersed in oil, i.e. “water-in-oil microemulsion (W/O)”, depending on the proportions of the oil and water phases. The latter is called a reverse microemulsion, and the micelles can be used as nanoreactors for the synthesis of small silica nanoparticles,⁸³⁻⁸⁶ or for growing silica shells onto hydrophobic inorganic nanoparticles^{71, 87-97} as discussed in chapter 7 of this thesis. Reverse micelles form in a way that the hydrophilic polar heads of the surfactant molecules are attracted towards the inside and the hydrophobic apolar hydrocarbon tails are attracted by the non-aqueous solvent and are directed towards the outside. By altering the water to surfactant ratio and hence the amount of water trapped inside the micelle the size of the micelle can be varied to a certain degree. Hydrophobic reagents can partition to some extent into the micelles where they can mix and react.

It has been initially assumed that in order to obtain monodisperse core shell nanoparticles with a single core in each shell, the number of micelles has to match the number of cores. While it is important that each core is placed in a micelle, there are other factors affecting the growth mechanisms of the silica shell.^{79, 80} To grow a thicker silica shell, a higher ammonia to Igepal ratio could be used to increase the aqueous domain “size of the micelles” and the amount of TEOS used could be increased (see **Figure 5**). However, these factors can

increase homogeneous nucleation and lead to the formation of undesirable free silica cores. So, one should bear in mind that optimizing the number of aqueous domains (micelles) to the number of UCNP is not the only factor affecting the formation of one-to-one core shell UCNP@SiO₂ systems, but also the other factors affecting nucleation mechanisms described previously, such as monomer concentration and reaction time should be taken into account.⁷⁹

98

In this work, oil-in-water reverse microemulsion silica growth on the hydrophobic as-synthesized oleate-coated UCNP was applied as the first step in a multistep synthesis procedure. However, several consecutive microemulsion steps were applied (see **Figure 5**) in order to render the particles water dispersible, and colloidally stable to be capable of undergoing further regrowth of the UCNP@SiO₂ in one step. The results are explained in detail in chapter 7.

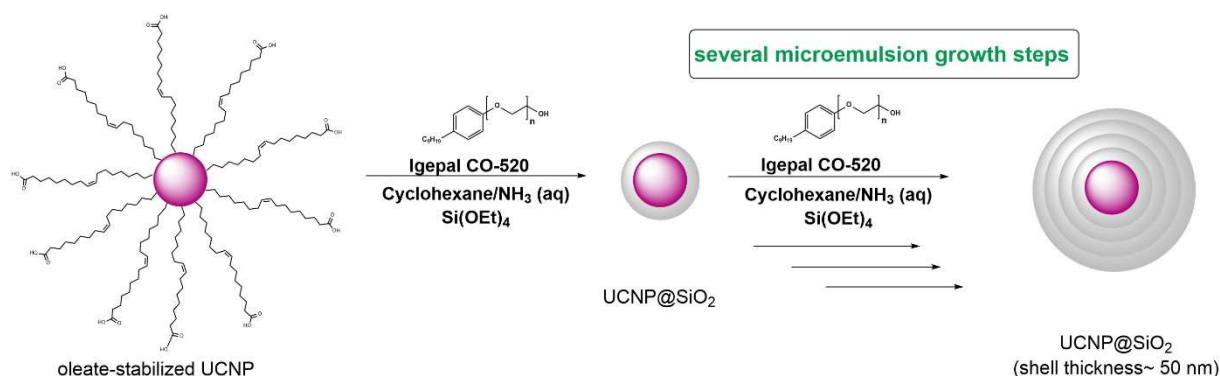


Figure 5: Schematic representation of the consecutive oil-in-water microemulsion silica coating procedure applied in chapter 7.

3.6.2 Silica Re-growth on Upconverting Nanoparticles

While the reverse microemulsion method can be used for silica coating of oil-dispersed nanoparticles, a modified version of the Stöber process can be used for the regrowth of silica nanoparticles dispersed in aqueous media. The method was originally developed by Stöber *et al.* in 1968 for the synthesis of silica nanoparticles with diameters of 30 nm to 1 μ m.⁹⁹ Stöber's synthesis was later optimized and developed for further growth of small silica nanoparticles.^{100, 101} In this thesis, a protocol for further growth of silica on UCNP@SiO₂ nanoparticles was studied and optimized. Details are presented in section 7.1.

3.6.3 Coating Upconverting Nanoparticles with a mesoporous silica shell

In order to coat nanoparticles with a mesoporous silica shell, a surfactant is used that acts as a stabilizing agent and as a template for the formation of the porous structure of silica at the same time. A variety of surfactants can be used to achieve this goal, amongst which are alkyltrimethylammonium surfactants and triblock copolymers. Triblock copolymers, such as Pluronic-type poly(alkylene oxide) triblock copolymers have been used as templates in mesoporous silica formation,^{102, 103} e.g. for the production of the so called Santa Barbara Amorphous (SBA-type) mesoporous nanoparticles (MSN).¹⁰³⁻¹⁰⁶ Alkyltrimethylammonium surfactants are commonly used as templates to form the mesopores in MCM-type materials (Mobil Composition of Matter), such as cetyltrimethylammonium chloride (CTAC),^{29, 107} octadecyltrimethoxysilane (C18TMS)⁷⁸ and cetyltrimethylammonium bromide (CTAB),¹⁰⁸⁻¹¹⁰ which was also used in this thesis for the preparation of mesoporous silica shells in the systems investigated in section 6.2. The silica shell is formed through hydrolysis and condensation of a silica precursor such as TEOS or tetramethoxysilane (TMOS), as explained in the previous section. Typically, the silica precursor is hydrolyzed in an ethanolic solution in the presence of aqueous ammonia or sodium hydroxide, followed by condensation of two silanol groups, or one silanol and an unhydrolyzed (or only partially hydrolyzed) alkoxy silane to form silica. The surfactant is removed at the end of the synthesis by ion exchange with inorganic salts (sodium chloride¹⁰⁷ or ammonium nitrate¹⁰⁹) or by calcination. In this work, CTAB was used as a stabilizing agent and as a template to form the mesopores (see **Figure 6**).

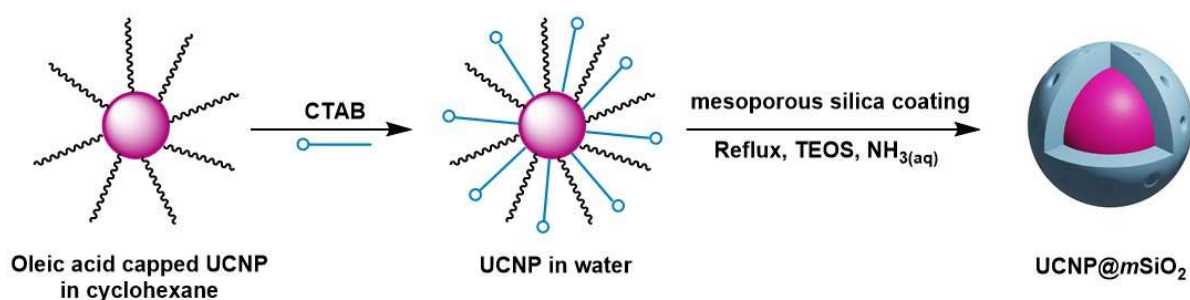


Figure 6: Schematic representation of the procedure used to coat UCNPs with a mesoporous silica shell.

3.7 Stability of Upconverting Nanoparticles and Monitoring their Dissolution in Aqueous Media

The use of UCNP in therapeutic applications and in bioimaging is based on the assumption that they are nontoxic or of very low toxicity.^{111, 112} This assumption is based on the fact that lanthanide fluoride powders have very low solubility products in water, e. g., the solubility product of LaF₃ powder in water is $K_{sp} = 3.26 \times 10^{-21}$.¹¹³ However, lanthanide fluoride nanoparticles can have higher solubility products than powders or bulk materials. Moreover, there have been recent reports on the dissolution of these nanoparticles in aqueous environments under high dilution conditions.¹¹⁴⁻¹¹⁹ The dissolution leads to the release of fluoride and lanthanide ions which can be toxic for biological systems.¹²⁰

UCNP surface chemistry plays an essential role in the dispersibility and colloidal stability of UCNP in aqueous environments and the prevention of their dissolution upon dilution, thereby minimizing toxicity concerns.^{112, 121} Surface passivation techniques are also important for shielding the lanthanide ions of the UCNP from luminescence-quenching molecules that contain moieties with high energy vibrations such as -OH.^{53, 122, 123} Dissolution of UCNP in aqueous solution causes partial loss of ions from the host crystal, which causes a decrease in the size of the nanoparticles, resulting in decreased luminescence intensity of UCNP upon dissolution. Consequently, UCNP aged in aqueous solutions have shorter luminescence decay lifetimes than the unaged UCNP. This decrease in luminescence intensity and lifetimes is more significant in diluted nanoparticle suspensions, where the solubility equilibrium can be achieved faster.¹¹⁷

Section 6.2 of this thesis demonstrates a thorough investigation of the factors affecting UCNP dissolution and suggests possible strategies for increasing their stability towards dissolution in aqueous and biologically relevant media.

4. Synthesis, Analytical Methods and Techniques

4.1 Synthesis of UCNP

The thermal decomposition synthesis of UCNP is carried out in high boiling solvents, such as oleic acid (b.p. 360°C) and octadecene (b.p. 315°C). Oleic acid acts as a solvent and as a stabilizing agent that prevents nanoparticles agglomeration. A two-pot synthesis is applied, first, a precursor is formed by reacting lanthanide chlorides with sodium oleate, then the precursor is heated up to 325°C to grow the UC nanocrystals to larger and more stable nanoparticles by the thermodynamically driven growth mechanism “Ostwald ripening”, which is based on the fact that larger nanoparticles are thermodynamically more favored than smaller nanoparticles. The nanoparticles are isolated by precipitation upon addition of ethanol to the reaction solution after cooling down to room temperature.

4.2 Structural Characterization of UCNP

Nanoparticle characterization is a very important step for the determination of their properties, due to the dependence of these properties on features such as particle size, size distribution, shape, shell thickness, and surface charge. Several characterization techniques were used in this work, including electron microscopy, dynamic light scattering and surface charge analysis.

4.2.1 Electron Microscopy

Since the theoretical limit for the resolution of a microscope is inversely proportional to the energy: higher energy means smaller structures can be resolved, electron microscopy is used for nanoparticles imaging.^{124, 125} The two most common types of electron microscopes are the Scanning Electron Microscope (SEM) and the Transmission Electron Microscope (TEM), see **Figure 7**. The components of the two microscopes are very similar, they both consist of an electron source, a series of electromagnetic and electrostatic lenses to control the shape and trajectory of the electron beam and electron apertures, which are placed inside a chamber that is under high vacuum.¹²⁶ To obtain an SEM image, a finely focused beam of electrons is scanned

across the surface of a solid sample in a raster pattern and the scattered or secondary electrons are collected. In TEM, the transmitted electrons that pass through the sample before they are collected are used for generating the image. SEM produces images that can be used to investigate the surface structure or topography of the particles. TEM images on the other hand are 2D projections of the sample, which can be used mainly for size and shape determination, and in some cases even information about the crystallinity of the particles. Similar to TEM, some SEMs allow for analyzing the specimen in transmission scanning electron microscope mode (TSEM) using suitable detectors. As in TEM, when the sample is scanned, the electrons penetrating the sample are detected.¹²⁴ The size and monodispersity of the UCNPs discussed in chapters 6 and 7 in this thesis were evaluated using TSEM images.

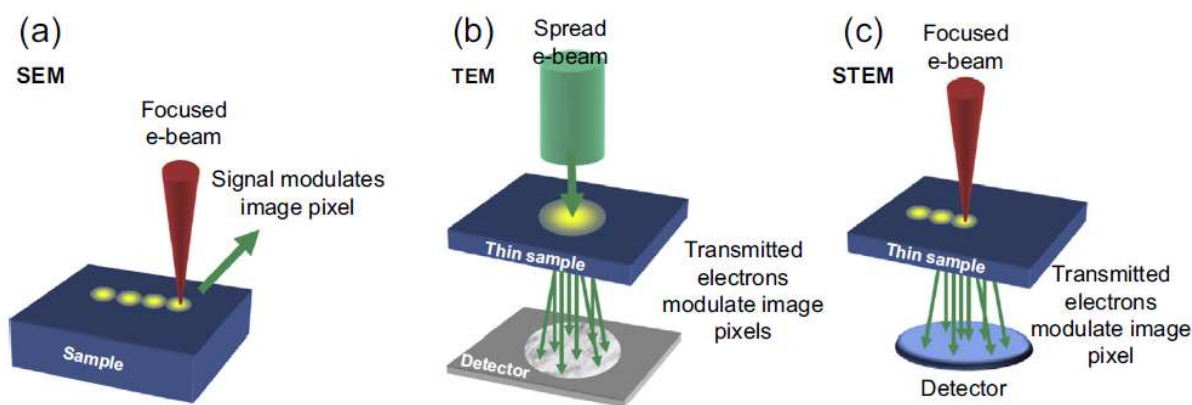


Figure 7: Schematic representation of SEM, TEM, and STEM imaging methodology.¹²⁶

4.2.2 Dynamic Light Scattering (DLS)

Particles in a suspension are in random and constant movement caused by their collision with the molecules of the solvent in which the particles are suspended. Illumination of the particles with a laser results in fluctuating, dynamic scattering of light, due to the Brownian motion of the particles. Dynamic light scattering (DLS) is a technique used to measure the Brownian motion of particles in a dispersion to determine their hydrodynamic diameter accordingly. The hydrodynamic diameter is the diameter of a sphere that diffuses at the same rate as the measured particle. The intensity changes over time due to the diffusion of the particles. Smaller particles diffuse faster than bigger particles, therefore, the intensity of the scattered light will change more rapidly for smaller particles than for larger ones.¹²⁷ During the DLS measurement, the intensity of the scattered light is recorded over time. The time

correlation of the intensity fluctuations is directly dependent on the diffusion time of the particles, and hence also on the size of the particles as described by the Stokes-Einstein equation. An autocorrelation analysis is used to determine the diffusion coefficient, and the particle size d_H is then calculated using the Stokes-Einstein equation:¹²⁸

$$d_H = \frac{kT}{3\pi\eta D}$$

Where d_H is the hydrodynamic diameter, k is the Boltzman constant, T is the absolute temperature at which the measurement is taken, η is the viscosity of the solvent, and D is the diffusion coefficient.

In this work, DLS measurements were performed on UCNP samples as a first characterization step. The results provide a hint about the polydispersity and the colloidal stability of the particles.

4.2.3 Surface Charge

When a charged particle is immersed in an aqueous electrolyte, ions from the solution are attracted close to the surface of the particle for charge balancing. This layer of charged ions close to the particle surface is called the Stern layer and is a fixed layer that moves together with the particle. There is a uniform distribution of cations and anions within an electrolyte solution. The oppositely charged ions (with regards to the particle's surface charge), are attracted close to the particle's surface, while the ions holding the same charge as the particles will be repelled. This region of ions balancing the charge of the particle is called the diffuse region. The Stern layer that is associated with and tightly bound to the surface of the material together with the diffuse layer are called the electrical double layer. The transition point between the bound and free liquid is called the slipping plane (see **Figure 8**). The energy required to attract a point charge towards the particle is called the electrical potential. The potential difference between the slipping plane and the potential of the bulk solution is called the zeta potential, and is typically considered a measure of surface charge and colloidal stability.¹²⁹ Surface charge affects the behavior of nanoparticles in different environments, particularly their tendency towards aggregation, as electrostatic repulsion between particles is a key factor promoting the stability of colloidal solutions. Zeta potential measurements were

performed for the UCNP used in section 6.2 to confirm the ligand exchange and colloidal stability of surface modified UCNP.

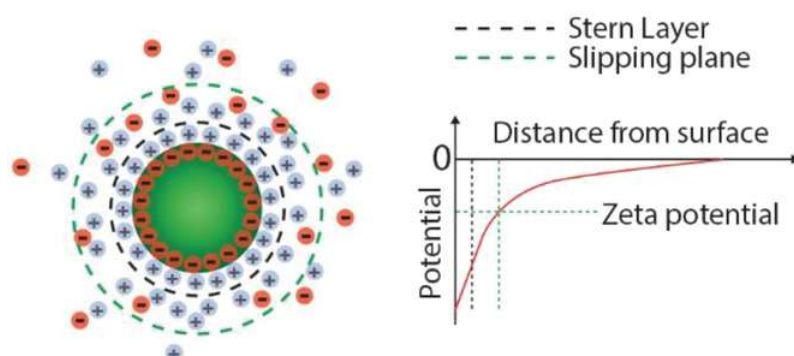


Figure 8: A schematic representation of the electric double layer of charged particles and the slipping plane which determines the zeta potential. Taken with permission from reference 112 (Adv. Mater. 2019, 31, 1901556) Licensed Content Publisher: John Wiley and sons. License number: 4915340197284

4.3 Optical Spectroscopy

The increasing focus of research on UCNP is due to their potential to convert light between different spectral regions and their unique photophysical properties, which make optical spectroscopy a very important characterization and analysis technique for the study and investigation of this kind of particles. According to IUPAC, optical spectroscopy is defined as the study of physical systems by electromagnetic radiation with which they interact or that they produce.¹³⁰ To fully investigate UCNP, properties such as absorption, fluorescence emission and emission lifetime of the particles are determined. A Jablonski diagram is usually used to illustrate the processes that occur during the absorption and emission of light. Jablonski diagrams are used in a variety of forms, a simple form of the diagram is shown in **Figure 9**.

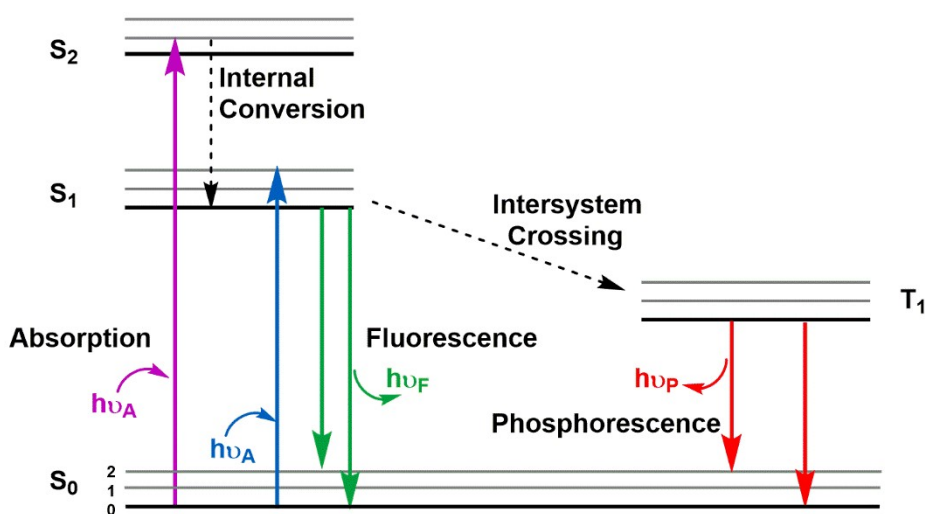


Figure 9: A simple form of a Jablonskii diagram. The singlet ground, first, and second electronic states are symbolized by S_0 , S_1 , and S_2 , respectively. At each of these electronic energy levels the fluorophores can exist in a number of vibrational energy levels, numbered 0, 1, 2 in the figure. Reproduced from Lakowicz J. Principles of Fluorescence Spectroscopy, 2006, third Edition.

When electromagnetic radiation is transmitted through a material, atoms absorb light, which results in the promotion of electrons from the ground state S_0 to a short-lived high energy excited state (for example, S_1). Fluorescence emission occurs when the excited electrons relax back to the ground state, and the wavelength of the emitted photon corresponds to the energy gap between the ground and excited states. The wavelength of the emitted photon is commonly higher than the excitation wavelength, and the energy gap is known as the “Stokes shift”. However, in UCNPs, the emitted light has a lower wavelength than the excitation light, which is also referred to as an “anti-Stokes” shift. Absorption measurements are commonly performed by scanning the monochromator that produces the monochromatic light that reaches the sample. Emission spectra are commonly obtained by keeping the excitation wavelength constant and scanning the emission monochromator. A fluorescence excitation spectrum is obtained by fixing the emission wavelength and scanning the excitation monochromator over a suitable wavelength range.¹³¹

4.3.1 Fluorescence lifetimes

Fluorescence lifetime (τ) is the average amount of time a fluorophore remains in the excited state following excitation,¹³² is affected by changes in the electronic transitions during a radiative decay. Determination of the fluorescence lifetime of UCNPs is important, for

example, changes in (τ) can confirm energy transfer from UCNP to an organic fluorescent dye. In addition, the intensity and relative spectral distribution of the fluorescence lifetime depend on UCNP size and the microenvironment,^{66, 117, 133} for that reason, conducting these measurements can give valuable insights into particle aging in aqueous media, which was the main focus of section 6.2 in this work. The fluorescence lifetime (τ) can be calculated by the following equation:¹³²

$$\tau = \frac{1}{(kr + k_{ic} + k_{isc})}$$

Where k_r is the radiative rate constant, k_{ic} is the internal conversion rate constant, and k_{isc} is the rate constant of intersystem crossing.

4.4 Analytical Measurements

4.4.1 Inductively Coupled Plasma-Optical Emission Spectrometry (ICP-OES)

Inductively coupled plasma-optical emission spectroscopy is a routine measurement technique for the qualitative and quantitative determination of the elemental composition of materials.¹³⁴ In this thesis, ICP-OES was used to determine the exact lanthanide ion amounts contained in the UCNP investigated in chapters 6 and 7, as the amounts and ratios of the lanthanide ions in the particle influence their optical characteristics. In addition, it was used to determine the exact amount of the lanthanide ions released from UCNP upon aging (section 6.1).

The sample must be introduced in the liquid phase, for example, in the case of UCNP, the particles are dissolved and then drawn into a peristaltic pump that delivers the sample to the nebulizer where the sample is converted into a fine aerosol spray. The fine spray droplets are directed into a hot plasma, which is a highly energized ionic gas. Argon gas is used as a plasma source in an ICP-OES. The sample's aerosol vaporizes in the plasma and its atoms and ions are excited. The excited atoms and ions emit their characteristic radiation which is then transferred into a high resolution optical sealed system, which separates light into the specific wavelengths for the elements to be measured. The emitted light is detected and used to quantify the amounts of ions into concentration units. **Figure 10** represents a diagram of a typical ICP-OES instrument.

The main advantage of the ICP over methods that use other excitation sources refers to its capability for efficient and reproducible vaporization, atomization, excitation, and ionization for a wide range of elements in various sample matrices. This is mainly due to the high temperature of 6000–7000 K in the observation zones of the ICP. Due to this high temperature, ICP-OES shows low background emission and low chemical interference. ICP-OES is used for the detection of over 70 elements with a very low detection limit of most elements (0.1 – 100 ng/mL).¹³⁴

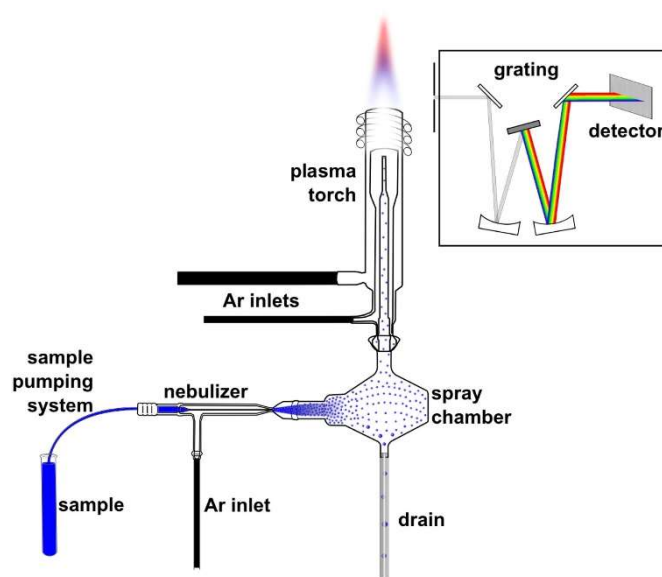


Figure 10: Diagram of a typical ICP-OES instrument with radial configuration of the detection system, highlighting the most important parts. Taken with permission from (Cement and Concrete Research 91 (2017) 52–60) Licensed Content Publisher: Elsevier. License number: 4915390947716

4.4.2 Fluoride-Ion Selective Electrode (ISE)

An ion selective electrode (ISE), also known as membrane electrode, uses potentiometry to generate a difference in electrical potential between an ion selective electrode and a reference electrode. The output potential is proportional to the concentration of the ion of interest. In the case of a fluoride ISE, the ion selective membrane is a single crystal of lanthanum fluoride (LaF_3) doped with europium fluoride (EuF_2) to create fluoride vacancies that allow ionic conduction by fluoride.¹³⁵ While the reference electrode used is made of a combination of silver and potassium chlorides. A calibration curve should be established for the determination of the ion activity in the sample. The electric potential (voltage) depends on the logarithm of the ionic activity, according to Nernst equation:

$$E = E^{\circ} - \frac{RT}{nF} \ln a F^{-}$$

Where E: is the measured electrical potential

E° : is the standard cell potential

R: is the ideal gas constant

F: is Faraday constant

$a F^{-}$: is the activity of the fluoride ion

For best results, the measurements are performed at a fixed ionic strength. The ionic strength is kept high by the use of an ionic strength adjuster (ISA) or a total ionic strength adjusted buffer solution (TISAB),¹³⁶ so that the various contributions of the measuring ion to the total ionic strength can be neglected. The fluoride ISE is highly selective, and the only ion which significantly interferes with the measurement of fluoride ions is hydroxide (OH^{-}). However, this interference can be avoided by using a buffered solution to keep the pH value of the solution below 7. A fluoride ion selective electrode was used for the work in this thesis for the detection of the amount of fluoride ions released from UCNP upon aging in aqueous media, the results are presented in section 6.2.

5. Synopsis of Results, Conclusions & Outlook

In this work, stability, surface modification and sensitization of upconversion nanoparticles (UCNP) were investigated. In section 6.1, the fluorescence emission of UCNP was enhanced by NIR dye sensitization. In section 6.2, the stability of UCNP in aqueous media was monitored and investigated. In section 7.1, the coating process of UCNP with silica nanoshells of controllable thicknesses was optimized.

In section 6.1, a successful and simple strategy to prepare UCNP systems with dye sensitization of the UC emission was demonstrated. A near infrared (NIR) absorbing and emitting cyanine dye (1859 SL), core-only UCNP, and two biocompatible surfactants, namely Pluronic F-127 and Tween 80, were used. This micellar encapsulation is advantageous in that it ensures that the dye molecules are in close proximity to the UCNP surface (and hence the optically active lanthanide ions), which is a requirement for efficient energy transfer. Other advantages of this approach are that it is fast, inexpensive, and experimentally simple without the need of chemical surface modification of the UCNP or the dye, or the need of covalent binding of the dye to the UCNP. The hydrophobic moieties of the surfactants enables their confinement of the dye 1859 SL in the hydrophobic pocket around as synthesized, oleic acid capped UCNP. Excitation of the dye with an 808 nm continuous wave laser showed strong fluorescence emission of the UCNP with an enhancement factor of about 21 compared to the direct excitation of a control sample under identical conditions. This confirmed energy transfer from the excited dye molecules to the Yb^{3+} ions, followed by energy transfer to the emitting Er^{3+} ions (energy transfer upconversion). Moreover, the excitation of the UCNP core could be shifted from 980 nm to 808 nm, which lies in the biological optical window where water absorption and hence heating effects are minimized. In future work, further investigations could be conducted to determine the exact mechanisms involved in the demonstrated energy transfer. Additionally, a thin undoped NaYF_4 shell could be added on the surface of the UCNP and prior to the dye encapsulation to achieve a better enhancement to the fluorescence emission by minimizing surface quenching, bearing in mind that energy transfer is affected by the distance between the dye and Yb^{3+} and Er^{3+} ions.

In section 6.2, the stability of UCNP in aqueous media was monitored by aging UCNP in water, phosphate buffered saline (PBS) and Dulbecco's modified Eagle medium (DMEM) at room and body temperature (37 °C). Other parameters addressed were particle size, surface functionalization and concentration of the UCNP. Special emphasis was dedicated to assess the influence of surface functionalization. Polyacrylic acid coated, citrate coated and bare UCNP were investigated. Additionally, mesoporous and microporous silica shells of different thicknesses were applied to UCNP to assess their potential for UCNP protection against dissolution. Dissolution was confirmed and quantified electrochemically using a fluoride ion-selective electrode (ISE) and inductively coupled plasma optical emission spectrometry (ICP OES) to determine the amount of released fluoride and lanthanide ions, respectively. In addition, luminescence measurements were conducted on fresh and aged UCNP to investigate the effect of dissolution on UCL. These experiments revealed that smaller particles are more prone to dissolution. Coating of the UCNP surface with a silica shell considerably improved particle stability in water and in PBS under all conditions assessed, and a sufficiently thick microporous silica shell inhibited dissolution almost completely. Our results also underlined the critical influence of the chemical composition of the aqueous environment on UCNP dissolution. Dissolution was more pronounced in PBS containing lanthanide binding phosphate anions compared to water, while dissolution was negligible in DMEM. The inhibition of dissolution in DMEM was attributed to the formation of a layer of adsorbed molecules on the UCNP surface. This layer not only protected the UCNP from dissolution, but also enhanced their luminescence lifetime. This layer was further examined by X ray photoelectron spectroscopy (XPS) and mass spectrometry (MS) measurements, which suggested that mainly phenylalanine, lysine, and glucose are adsorbed on the UCNP surface from DMEM. In future projects, it would be interesting to investigate and optimize the thickness of the silica shell regarding optimum protection with minimum thickness, as the size of a nanoparticle can be an important parameter for many biological and bioanalytical applications. In addition, employing the findings of DMEM incubated UCNP in cellular toxicity studies would be interesting for the design of new biocompatible surface coatings for UCNP and other nanoparticles as well.

In section 7.1, a new method for the growth of silica shells of sizes between 5 and 250 nm on oleate coated UCNP was developed. This method includes the growth of silica on the

oleate coated particles in multi step reverse microemulsion reactions performed consecutively without intermediate isolation or purification steps. In each step, the same volumes of TEOS and aqueous ammonia were added, and the volumes of cyclohexane and Igepal CO-520 were increased while keeping the concentration of Igepal CO 520 in cyclohexane constant. The formation of the undesirable core free silica particles was successfully prevented by careful adjustment of the aqueous domain and the concentration of the added silica precursor. This stepwise procedure produced stable core shell nanoparticles with zeta potential values less than - 40 mV. Five to six coating steps were required to achieve that, then the particles were isolated by centrifugation and dispersed in an ammoniacal ethanol solution to be grown by continuous addition of TEOS in one step up to a diameter of more than 500 nm in a modified Stöber process. The prior reverse microemulsion stepwise procedure was necessary for growing thick silica shells on the UCNP, since a direct growth of silica on oleate coated UCNP was not possible in a Stöber like growth process which requires nanoparticles with hydrophilic surfaces. We anticipate that this protocol will also be useful for the coating of other nanoparticles with similar hydrophobic surface functionalities such as iron oxide nanoparticles or semiconductor nanoparticles with hydrophobic capping agents.

In summary, the main objectives anticipated from this thesis have been thoroughly investigated. 1859 SL dye sensitization of UCNP showed an enhancement to the UCL compared to that of the control sample without the dye. A reproducible protocol for the coating of UCNP with silica was optimized, producing monodisperse and colloiddally stable core shell particles. The systematic investigation of UCNP dissolution in aqueous media showed a suitable surface passivation can inhibit ion release from the particles, and that the chemical composition of the aqueous environment has a critical influence on the dissolution of UCNP. For example, adsorption of compounds such as lysine from DMEM, protected the particles from dissolution. This finding can have a large impact on the interpretation of cytotoxicity studies of UCNP. Also on studies of other nanoparticles, as such experiments are normally done with nanoparticles dispersed in cell culture medium prior to their incubation with cells. To extend our understanding of the cytotoxicity of UCNP and their dissolution behavior in cells, viability tests to our particles on skin cells (keratinocytes) were performed by our collaboration partners (research group of Dr. Helena Oliveira, University of Aveiro,

Portugal) and we are currently evaluating the results before moving forward to further investigations.

6. Manuscripts: Major Contributions

6.1 Sensitization of upconverting nanoparticles with a NIR-emissive cyanine dye using a micellar encapsulation approach

Title	Sensitization of upconverting nanoparticles with a NIR-emissive cyanine dye using a micellar encapsulation approach
Authors	Maysoon I. Saleh , Ihor D. Panas, Florian Frenzel, Christian Würth, Bastian Rühle, Yuri L. Slominskii, Aleksander Demchenko and Ute Resch-Genger
Journal	Methods and Applications in Fluorescence. Volume 7, Number 1 Special issue on Upconversion Methods, Applications and Materials
DOI	https://doi.org/10.1088/2050-6120/aafe1f
Links	https://iopscience.iop.org/article/10.1088/2050-6120/aafe1f
Detailed scientific contribution	The concept of this manuscript was elaborated by I. Panas, A. Demchenko and U. Resch-Genger. Experiments were designed and planned by M. Saleh, I. Panas, F. Frenzel and B. Rühle. UCNPs were synthesized by M. Saleh, micellar encapsulation of the dye and structural characterization were performed by M. Saleh and I. Panas. Optical measurements were performed by F. Frenzel. Quantum yield measurements were performed by B. Rühle. All experimental results were interpreted and evaluated by M. Saleh, I. Panas, F. Frenzel, B. Rühle and U. Resch-Genger. The manuscript was mainly written by M. Saleh, B. Rühle and U. Resch-Genger.
Estimated own contribution	~ 40 %
Date of publication	23. January. 2019

PAPER

Sensitization of upconverting nanoparticles with a NIR-emissive cyanine dye using a micellar encapsulation approach

Recent citations

- [A new forum for upconversion research: the UPCON conference](#)
Hans H Gorris *et al*

To cite this article: Maysoon I Saleh *et al* 2019 *Methods Appl. Fluoresc.* **7** 014003

View the [article online](#) for updates and enhancements.



EXPERTS IN MOLECULAR SPECTROSCOPY

Photoluminescence • Raman • UV-Vis • Transient Absorption



Methods and Applications in Fluorescence



PAPER

Sensitization of upconverting nanoparticles with a NIR-emissive cyanine dye using a micellar encapsulation approach

RECEIVED
15 October 2018

REVISED
21 December 2018

ACCEPTED FOR PUBLICATION
14 January 2019

PUBLISHED
23 January 2019

Maysoon I Saleh¹, Ihor D Panas², Florian Frenzel¹, Christian Würth¹, Bastian Rühle¹, Yuri L Slominskii³, Aleksander Demchenko² and Ute Resch-Genger¹

¹ Federal Institute for Materials Research and Testing, Division Biophotonics, Richard-Willstätter-Str. 11, 12489 Berlin, Germany

² Palladin Institute of Biochemistry, Leontovycha str. 9, 01601, Ukraine

³ Institute of Organic Chemistry, Murmanska str. 5, 02660 Ukraine

E-mail: Ute.Resch@bam.de

Keywords: upconversion, NIR-dye sensitization, cyanine dyes, luminescence, emission enhancement, micellar encapsulation, NaYF₄:YbEr

Supplementary material for this article is available [online](#)

Abstract

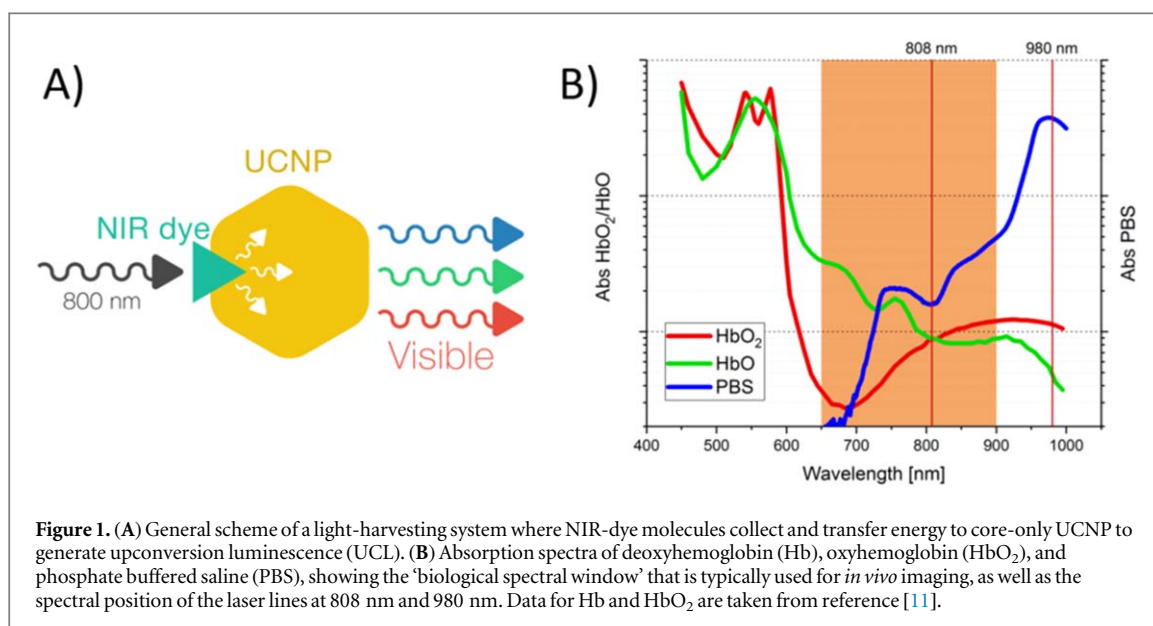
Photon upconversion nanomaterials have a wide range of applications, including biosensing and deep-tissue imaging. Their typically very weak and narrow absorption bands together with their size dependent luminescence efficiency can limit their application potential. This has been addressed by increasingly sophisticated core-shell particle architectures including the sensitization with organic dyes that strongly absorb in the near infrared (NIR). In this work, we present a simple water-dispersible micellar system that features energy transfer from the novel NIR excitable dye, 1859 SL with a high molar absorption coefficient and a moderate fluorescence quantum yield to oleate-capped NaYF₄:20%Yb(III), 2%Er(III) upconversion nanoparticles (UCNP) upon 808 nm excitation. The micelles were formed using the surfactants Pluronic F-127 and Tween 80 to produce a hydrophilic dye-UCNP system. Successful energy transfer from the dye to the UCNP could be confirmed by emission measurements that revealed the occurrence of upconversion emission upon excitation at 808 nm and an enhancement of the green Er(III) emission compared to direct Er(III) excitation at 808 nm.

Introduction

Upconversion nanoparticles (UCNP) have many interesting features that are of high importance in various fields of applications such as bioimaging, bioanalytical assays, photodynamic therapy, and solar cells [1–4]. One of the main limitations of UCNP is the very weak (10^{-20} cm²) absorption cross section [5] due to parity-forbidden 4f-4f transitions [6] in conjunction with the very narrow absorption bands (full width at half maximum (FWHM) of the absorption band of about 10 nm–20 nm in the ultraviolet, visible, and near infrared spectral region). Moreover, their photoluminescence quantum yields are relatively low and depend on excitation power density as well as on the surface-to-volume ratio, due to the multiphotonic nature of the upconversion (UC) process and surface quenching effects, particularly for core-only UCNP [7], [8]. Near infrared (NIR) dyes coupled to UCNP can provide a potential strategy to boost UCNP

brightness, the product of the molar absorption coefficient or cross section and the photoluminescence quantum yield as shown before [1–3]. The relatively broad absorption bands and the strong absorption cross section of organic dyes render them ideal light harvesters and energy donors for UCNP (figure 1), [6], [9]. Moreover, these dyes can also help shifting the excitation of the dye-UCNP systems from typically 980 nm for Yb-doped UCNP closer to 800 nm, which fits better into the biological spectral window and prevents heating effects by water absorption [10]. This can increase the applicability of these materials, especially for biological studies.

Dye sensitization of UCNP can occur via the Förster mechanism (through electrostatic interactions between a donor and an acceptor presented as point dipoles) and/or the Dexter mechanism (involving the bilateral exchange of electrons between donor and acceptor in a spin-conserved singlet-singlet or triplet-triplet transfer) from light harvesting organic dyes



located directly at or in the immediate vicinity of the UCNP surface across the organic/inorganic interface to the optically active lanthanide ions incorporated in the UCNP [5]. The latter is significant only at very short donor-acceptor distances (~ 10 Å or less), while electrostatic interactions can occur over longer distances (10–100 Å).

The first successful attempt of dye sensitized UC was reported by Zou *et al* [12]. The authors used the dye IR-806, which is a carboxylic acid derivative of the commercially available dye IR-780, attached to UCNP by replacing the oleylamine ligands on the as-synthesized oleylamine-coated UCNP. Upon excitation at 800 nm, this dye-UCNP system produced the typical upconversion luminescence (UCL) spectrum of Yb, Er co-doped materials with the green and red Er(III) emission bands. This initiated an increasing number of studies of dye-UCNP systems prepared by attaching NIR dyes to UCNP with different ligand functionalities [5], [6], [9], [13], [14]. Other strategies included the modification of UCNP with an inactive protective shell to minimize surface quenching of the lanthanide ions [6], [13] or adding an active shell of NaYF₄ doped with Yb(III) or Nd(III) to further increase the energy transfer efficiency [14]. In the majority of these studies, the exact nature of the dye-UCNP energy transfer mechanism was not explained in detail. Only recently, Garfield *et al* [15] reported that in the case of the dye IR-806 attached to NaGdF₄ nanoparticles (undoped and doped with Yb(III) and Er(III)), the Gd(III) ions seem to mediate intersystem crossing of the antenna dyes and thereby, nonradiative energy transfer from the dye's triplet state energy.

The NIR dye, IR-806, chosen by Zou *et al* [12] in their proof-of-concept study, absorbs strongly between 650 nm–850 nm with a maximum at 806 nm. Although the overlap between the emission spectrum of this dye and the absorption spectrum of the UCNP

is not ideal, sensitized UCL could be observed. In this work, we investigate dye sensitization of UCNP using the custom-made NIR dye 1859 SL [15] that has a photoluminescence quantum yield that is comparable to IR-806, yet its emission spectrum overlaps better with the absorption bands of the UCNP. Moreover, this dye can form emissive J-aggregates in aqueous solution and its absorption below 600 nm is weak which is essential to minimize the absorption of the emitted upconverted photons. Dye-UCNP systems were obtained by a simple and experimentally easy and inexpensive approach by encapsulating the dye molecules in a micelle surrounding hydrophobic oleate-stabilized core-only NaYF₄: 20%Yb(III), 2%Er(III) UCNP with the aid of different surfactants. This approach was first described by Tao *et al* [16] who embedded the dye IR-1061 in a poly(acrylic acid) matrix and then conjugated the dye-PAA with DSPE-mPEG (a polyethylene glycol-conjugated phospholipid) coated nanoparticles.

Materials and methods

Lanthanide chlorides used for the synthesis of the UCNP were purchased from Sigma Aldrich with high purity (99.99%). Pluronic F-127, sodium oleate, oleic acid, and octadecene (90% technical grade) were obtained from Sigma Aldrich and used without further purification. Tween 80 was purchased from Merck, and the IR dye 1859 SL was synthesized in the research group of Dr Y Slominskii according to a published procedure [15]. All solvents employed for the optical measurements were purchased from Sigma Aldrich in spectroscopic grade.

Absorption and fluorescence spectra and the photoluminescence quantum yields (QY) were measured with a CARY 5000 absorption spectrometer (Varian) and a FSP920 fluorescence spectrometer (Edinburgh

Table 1. Composition of the Pluronic F-127 encapsulated samples.

Sample	1	2	3	4	5	6	7
1859 SL, μg	0	4.2	12.8	25.6	38.4	51.6	25.6
F-127, g	0.01	0.01	0.01	0.01	0.01	0.01	0.01
UCNP, mg	20	20	20	20	20	20	0
Dye-to-UCNP ratio ($\mu\text{g}/\text{mg}$)	0	0.21	0.64	1.28	1.92	2.58	0

Instruments) equipped with a xenon lamp and a 980 nm laser diode. The emission lifetimes were obtained with FLS980 and FLS920 fluorescence lifetime spectrometers (Edinburgh Instruments). A more detailed experimental procedure describing the relative QY measurements using the dye IR 140 as quantum yield standard [17] as described by Würth *et al* [18] can be found in the Supporting Information (SI; is available online at stacks.iop.org/MAF/7/014003/mmedia). Energy transfer and photostability studies of micellar UCNP–cyanine dye systems were done with a Lambda 900 (UV/Vis/NIR) absorption spectrometer (Perkin Elmer) and a FLS980 fluorescence lifetime spectrometer (Edinburgh Instruments), respectively. All measurements were carried out at room temperature in 1 cm quartz cells (Hellma).

Dynamic light scattering (DLS) measurements of the UCNP–cyanine dye systems were performed with a DLS Zeta Potential Analyzer, Zetasizer Nano ZS90 (Malvern).

Upconversion nanoparticle preparation

NaYF_4 : 20%Yb(III), 2%Er(III) were synthesized according to a previously reported procedure with some modifications [19]. The synthesis and analytical characterization of the nanoparticles are provided in the SI.

Sample preparation

Stock solutions of 1859 SL dye in chloroform (0.47 mg mL^{-1} , 0.45 mM), Pluronic F-127 in water (200 mg mL^{-1} , 0.016 M) and oleic acid capped UCNP in chloroform (50 mg mL^{-1}) were mixed in various proportions as shown in table 1.

The samples were prepared in the compositions indicated in table 1. After mixing, each sample was dried under argon in a 50 ml round bottom flask. Dried samples were redispersed in 2 ml of Milli-Q water under sonication in an ultrasonic bath.

In the Tween 80 experiments, the same procedure was applied. Stock solutions of 1859 SL dye in chloroform (0.62 mg mL^{-1} , 0.59 mM), Tween 80 in water (500 mg mL^{-1} , 0.382 M), and oleic acid capped UCNP in chloroform (7 mg/mL) were mixed in various proportions, as specified in table 2.

Results and discussion

The absorption and emission spectra of dye 1859 SL are shown in figure 2. This includes the spectra of the

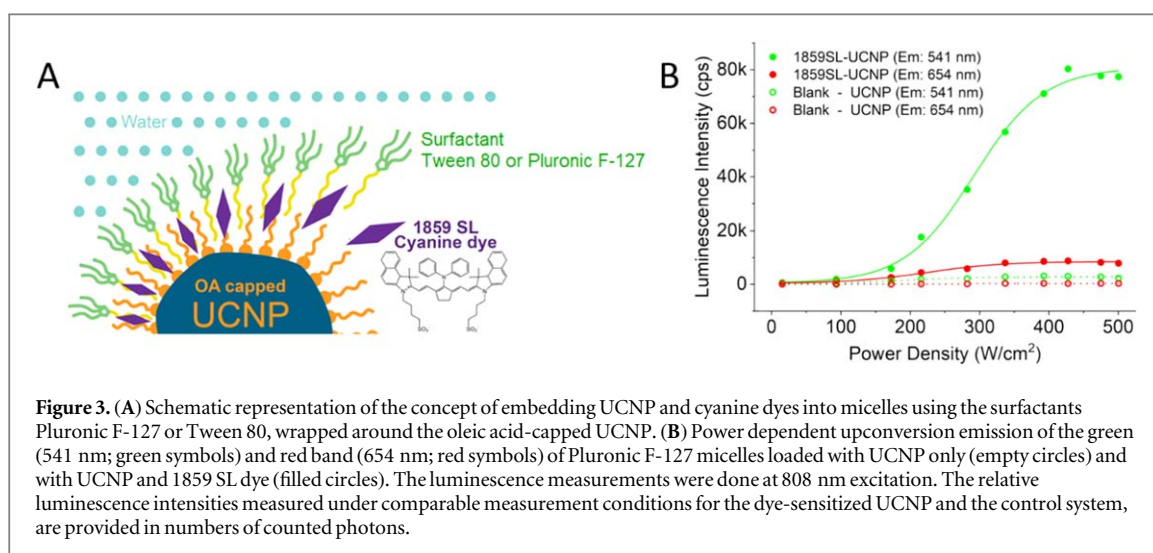
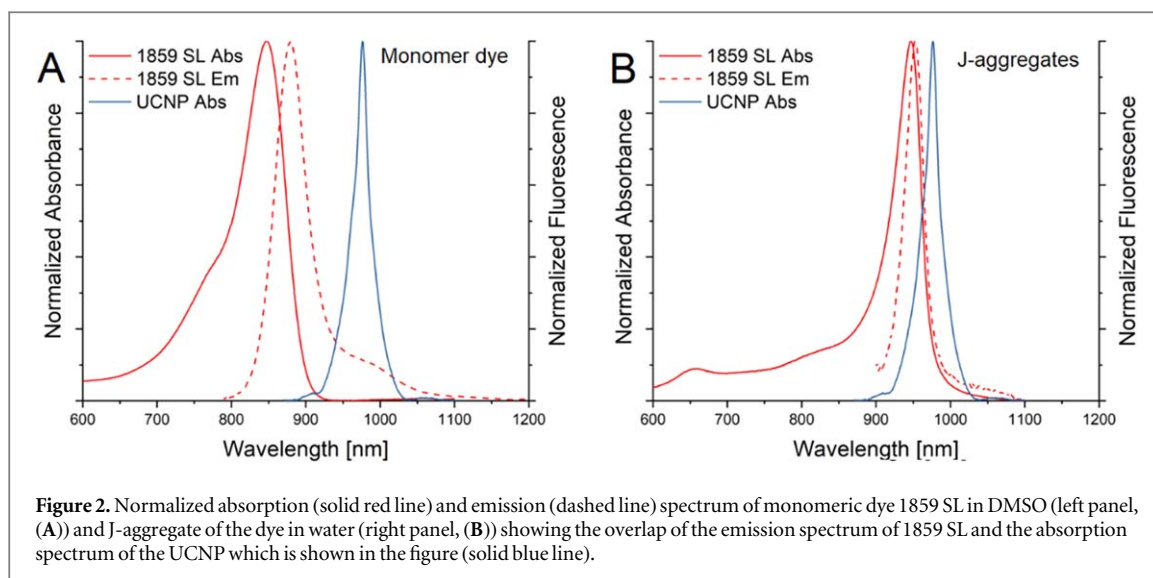
Table 2. Composition of the Tween 80 encapsulated samples.

Sample	1	2	3	4	5
Dye stock, μg	0	1.05	2.80	9.80	16.80
Tween 80 stock, g	0.03	0.03	0.03	0.03	0.03
UCNP stock, mg	0.35	0.35	0.35	0.35	0.35
Dye-to-UCNP ratio ($\mu\text{g}/\text{mg}$)	0	3	8	28	48

monomeric dye in DMSO as well as the absorption and emission spectra of its J-aggregates formed in water at a higher dye concentration. The fact that this dye forms J-aggregates with a very strong absorption band at 946 nm could enable studying whether dye sensitization of UCNP can occur with J-aggregates known for their very high molar absorption coefficients. QY measurements of the monomeric dye in DMSO and its J-aggregates in water revealed, however, QY of 11.9% and only 0.04%, respectively. The low QY of the J-aggregates prevented us from further investigations of their use as light-harvesting antennas.

In order to assess the occurrence of dye sensitization, we compared the luminescence behavior of the micellar-encapsulated 1859 SL–UCNP systems with that of a control system, here micellar-encapsulated UCNP lacking the dye, studied under identical measurement conditions. The 1859 SL–UCNP@Pluronic F-127 system shows strong upconversion emission at 541 nm and 654 nm upon excitation at 808 nm (figure 3, right panel and figure 4), while only very weak emission was observed for the control system lacking the dye, under identical conditions. The weak emission arising from the UCNP in the control system originates from the direct excitation of the $^4\text{I}_{9/2}$ energy level of Er(III). The strong enhancement of the upconversion luminescence in the order of 21 provides clear evidence of dye sensitization.

Next, the 1859 SL–UCNP@Pluronic F-127 system was optimized regarding the dye content to achieve an efficient sensitization. A dye content between 0.64–1.28 μg per milligram of UCNP was found to be optimal for this system (figures 4(A) and (B)). Higher dye loading concentrations led to reabsorption and possibly also self quenching of the dye molecules, lowering the luminescence intensity of the antenna dyes and the dye-UCNP system. As can be seen by comparing the emission intensities of the micellar system lacking the NIR dye (red line in figure 4(B)) with the emission intensity of the same system containing 0.64 $\mu\text{g}/\text{mL}$ 1859 SL acquired under identical



conditions, a strong enhancement of the upconversion luminescence can be achieved. The very weak luminescence of the micellar system upon excitation at 808 nm in the absence of the dye is attributed to direct excitation of erbium ions.

While the 1859 SL–UCNP@Pluronic F-127 system demonstrated promising luminescence features and underlined the feasibility of using such a micellar system for dye sensitization, DLS measurements of this system showed a hydrodynamic diameter of the micelles of about 1 μm (SI, figure S3). This reveals that the system was not colloidally stable in water for a longer period of time and may tend to form agglomerates in water.

To overcome the agglomeration issues with Pluronic F-127 [20], Tween 80 was used for encapsulating OA-capped UCNP (figure 3(B)). As with Pluronic F127, the 1859 SL dye molecules can be trapped inside the hydrophobic organic surfactant shell of the UCNP within a distance that is close enough for energy transfer from dye molecules to the UCNP.

The optimized micellar system, 1859 SL–UCNP@Tween 80, showed better results in terms of a narrower size distribution and colloidal stability in DLS. Moreover, it also revealed efficient dye sensitization of the UCNP emission, with the intensity of the upconversion emission depending on the dye-to-UCNP ratio as observed previously for the Pluronic F-127 system (figure 4). The optimal dye content for the Tween 80 systems is about 8 μg per milligram of UCNP (figure 4, panels (B) and (D)). The strongly enhanced upconversion of the micellar system that contains UCNP and the optimum dye concentration (purple spectra in figure 4, panels (B) and (D)) compared to that of the control system provides solid proof of successful energy transfer from the dye molecules to the UCNP under these conditions.

In both types of micellar systems, however, dye photodegradation occurred at the very high excitation power densities used for these studies (SI, figure S4). Similar photostability issues have been also reported for other NIR dye sensitized systems [9].

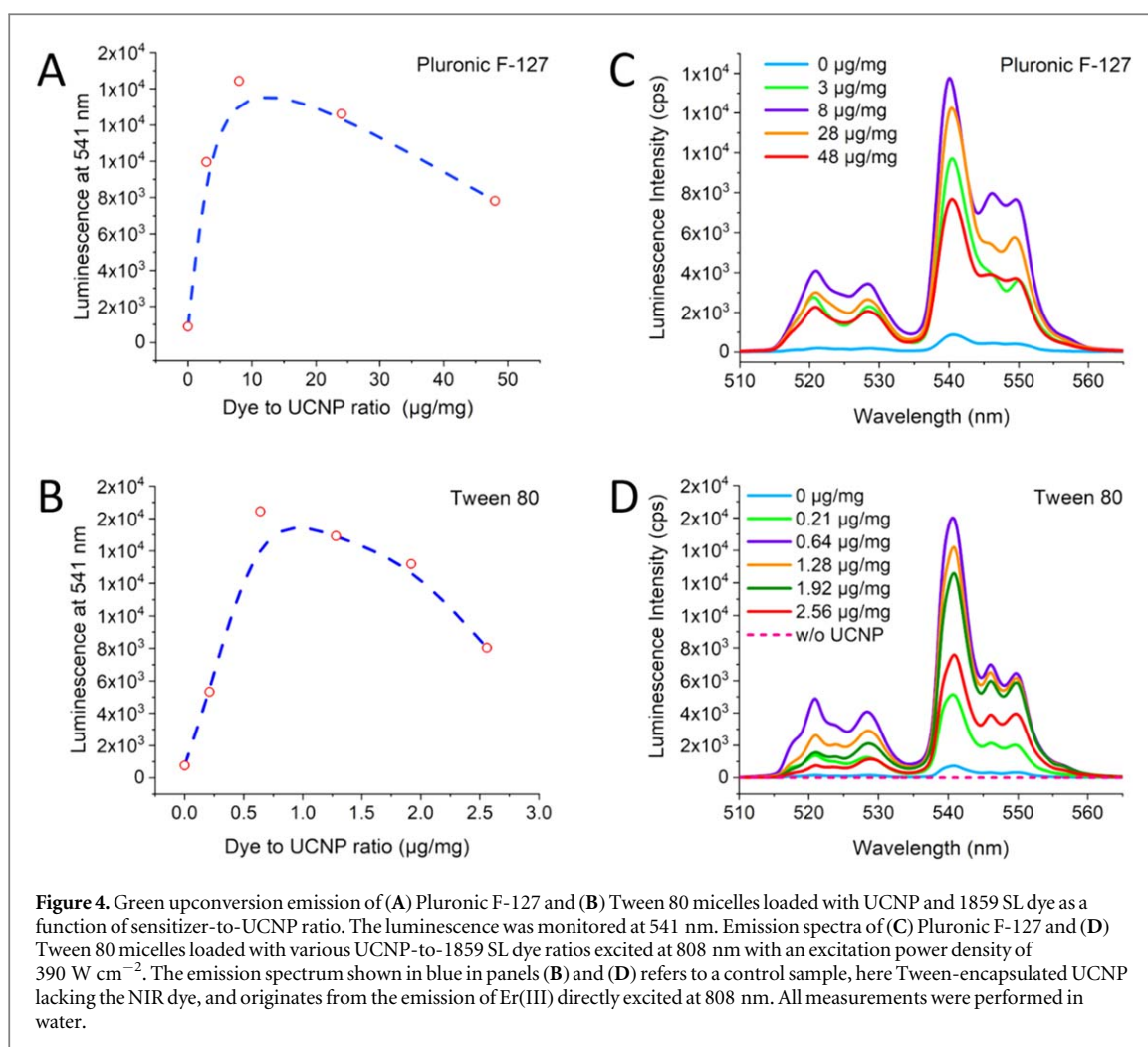


Figure 4. Green upconversion emission of (A) Pluronic F-127 and (B) Tween 80 micelles loaded with UCNP and 1859 SL dye as a function of sensitizer-to-UCNP ratio. The luminescence was monitored at 541 nm. Emission spectra of (C) Pluronic F-127 and (D) Tween 80 micelles loaded with various UCNP-to-1859 SL dye ratios excited at 808 nm with an excitation power density of 390 W cm^{-2} . The emission spectrum shown in blue in panels (B) and (D) refers to a control sample, here Tween-encapsulated UCNP lacking the NIR dye, and originates from the emission of Er(III) directly excited at 808 nm. All measurements were performed in water.

Conclusion

We demonstrated a successful strategy for simple and easy to prepare upconversion nanoparticle (UCNP) systems with dye sensitization of the upconversion emission, using a near infrared (NIR) absorbing and emitting cyanine dye, core-only UCNP, and micelle-forming surfactants. Excitation of the dye with an 808 nm CW laser showed strong fluorescence emission of the UCNP with an enhancement factor of about 21 compared to the excitation of the dye-lacking UCNP control sample under identical conditions which produced only very weak emission, arising from the direct excitation of Er(III) ions. This confirms energy transfer from the excited dye molecules to the Yb(III) ions, followed by energy transfer to the subsequently emitting Er(III) ions (energy transfer upconversion). This shifts the excitation of the Yb(III), Er(III)-doped NaYF_4 UCNP core from 980 nm to 808 nm located in the biologically relevant first diagnostic window where water absorption and hence heating effects are minimized.

This strategy could be realized with the two well-known and biocompatible surfactants Pluronic F-127 [21–24] and Tween 80 [20], underlining its versatility. This micellar encapsulation ensures that the dye

molecules are in close neighborhood to the UCNP surface and hence the optically active lanthanide ions within these UCNP, as required for energy transfer. Moreover, this approach is fast, inexpensive, and experimentally simple without the need of chemical surface modification of the UCNP [13], [25], modification of the dye [12], [13], [26] or covalent binding [27]. With their hydrophobic moieties, Pluronic F-127 and Tween 80 can confine 1859 SL in the hydrophobic pocket around oleic acid capped UCNP. Additionally, this approach renders the systems well dispersible in water, particularly in the case of Tween, which is an import requirement in biological applications. Our micellar encapsulation approach could be also interesting for theranostic applications in the future as the hydrophobic interior of such micellar systems can be used as an efficient nanocarrier for water-insoluble drugs [20].

The exact mechanisms involved in the demonstrated energy transfer still require further investigations which were beyond the scope of the current study. Presently, we cannot say whether dye sensitization by the NIR dye 1859 SL can be attributed merely to direct energy transfer from the dye's singlet state or whether its triplet state is also involved as observed by Schuck and colleagues [28] for NaGdF_4 UCNP. Here,

particularly the close proximity of the heavy and paramagnetic lanthanide Gd(III) ions induces intersystem crossing in the antennae cyanine dyes, with the dye triplet states then acting as energy donors.

Acknowledgments

This work was supported by The European Upconversion Network as a part of European Association in Science and Technology (COST). XRD data were done by Michael Labza in the Institute of Chemistry of Free University (FU) Berlin. ICP-OES measurements were performed by Janina Roik, Division 1.6, Federal Institute for Materials Research and Testing (BAM). URG, MIS, and FF gratefully acknowledge financial support from the grant RE1203/20-1 (M-Eranet project NANOHYPER; German Research Council (DFG)). The authors have declared that no conflicting interests exist.

Authors contribution

Maysoon I Saleh, Ihor D Panas and Florian Frenzel contributed equally to this work.

ORCID iDs

Ute Resch-Genger  <https://orcid.org/0000-0002-0944-1115>

References

- Chen G, Qiu H, Prasad P N and Chen X 2014 Upconversion nanoparticles: design, nanochemistry, and applications in theranostics *Chem. Rev.* **114** 5161–214
- Zhou J, Liu Q, Feng W, Sun Y and Li F 2015 Upconversion luminescent materials: advances and applications *Chem. Rev.* **115** 395–465
- Bünzli J-C G 2010 Lanthanide luminescence for biomedical analyses and imaging *Chem. Rev.* **110** 2729–55
- Resch-Genger U and Gorris H H 2017 Perspectives and challenges of photon-upconversion nanoparticles: I. Routes to brighter particles and quantitative spectroscopic studies *Anal. Bioanal. Chem.* **409** 5855–74
- Wang X, Valiev R R, Ohulchanskyy T Y, Ågren H, Yang C and Chen G 2017 Dye-sensitized lanthanide-doped upconversion nanoparticles *Chem. Soc. Rev.* **46** 4150–67
- Chen G, Shao W, Valiev R R, Ohulchanskyy T Y, He G S, Ågren H and Prasad P N 2016 Efficient broadband upconversion of near-infrared light in dye-sensitized core/shell nanocrystals *Adv. Opt. Mater.* **4** 1760–6
- Würth C, Kaiser M, Wilhelm S, Grauel B, Hirsch T and Resch-Genger U 2017 Excitation power dependent population pathways and absolute quantum yields of upconversion nanoparticles in different solvents *Nanoscale* **9** 4283–94
- Kraft M, Würth C, Muhr V, Hirsch T and Resch-Genger U 2018 Particle-size-dependent upconversion luminescence of NaYF₄:Yb,Er nanoparticles in organic solvents and water at different excitation power densities *Nano Res.* **1**–15
- Wu X et al 2016 Dye-sensitized core/active shell upconversion nanoparticles for optogenetics and bioimaging applications *ACS Nano* **10** 1060–6
- Söderlund H, Mousavi M, Liu H and Andersson-Engels S 2015 Increasing depth penetration in biological tissue imaging using 808-nm excited Nd³⁺/Yb³⁺/Er³⁺-doped upconverting nanoparticles *J. Biomed. Opt.* **20** 86008
- Takatani S and Graham M D 1979 Theoretical analysis of diffuse reflectance from a two-layer tissue model *IEEE Trans. Biomed. Eng.* **26** 656–64
- Zou W, Visser C, Maduro J A, Pshenichnikov M S and Hummelen J C 2012 Broadband dye-sensitized upconversion of near-infrared light *Nat. Photonics* **6** 560–4
- Chen G et al 2015 Energy-cascaded upconversion in an organic dye-sensitized core/shell fluoride nanocrystal *Nano Lett.* **15** 7400–7
- Huang X 2015 Giant enhancement of upconversion emission in (NaYF₄:Nd³⁺/Yb³⁺/Ho³⁺)/(NaYF₄:Nd³⁺/Yb³⁺) core/shell nanoparticles excited at 808 nm *Opt. Lett.* **40** 3599–602
- Dimitriev O P, Bricks J L, Smirnova A L and Slominskiy Y L 2017 Towards white-light generation through upconversion of low-power near-infrared photons *RSC Adv.* **7** 16126–30
- Tao Z, Hong G, Shinji C, Chen C, Diao S, Antaris A L, Zhang B, Zou Y and Dai H 2013 Biological imaging using nanoparticles of small organic molecules with fluorescence emission at wavelengths longer than 1000 nm *Angew. Chemie - Int. Ed.* **52** 13002–6
- Rurack K and Spieles M 2011 Fluorescence quantum yields of a series of red and near-infrared dyes emitting at 600–100 nm *Anal. Chem.* **83** 1232–42
- Würth C, Grabolle M, Pauli J, Spieles M and Resch-Genger U 2013 Relative and absolute determination of fluorescence quantum yields of transparent samples *Nat. Protoc.* **8** 1535–50
- Na H, Woo K, Lim K and Jang H S 2013 Rational morphology control of β -NaYF₄:Yb,Er/Tm upconversion nanophosphors using a ligand, an additive, and lanthanide doping *Nanoscale* **5** 4242–51
- Ren W, Tian G, Jian S, Gu Z, Zhou L, Yan L, Jin S, Yin W and Zhao Y 2012 TWEEN coated NaYF₄:Yb,Er/NaYF₄ core/shell upconversion nanoparticles for bioimaging and drug delivery *RSC Adv.* **2** 7037
- Shachaf Y, Gonen-Wadmany M and Seliktar D 2010 The biocompatibility of Pluronic®F127 fibrinogen-based hydrogels *Biomaterials* **31** 2836–47
- Alexandridis P and Lindman B (ed) 2000 *Amphiphilic Block Copolymers: Self-Assembly and Applications* (New York: Elsevier) 978-0-444-82441-7 (<https://doi.org/10.1016/B978-0-444-82441-7.X5000-2>)
- Moghim S M and Hunter A C 2000 Poloxamers and poloxamines in nanoparticle engineering and experimental medicine *Trends Biotechnol.* **18** 412–20
- Kabanov A V and Alakhov V Y 2000 Micelles of amphiphilic block copolymers as vehicles for drug delivery *Amphiphilic Block Copolym ()* (New York: Elsevier) 347–769780444824417
- Shao Q, Li X, Hua P, Zhang G, Dong Y and Jiang J 2017 Enhancing the upconversion luminescence and photothermal conversion properties of ~800 nm excitable core/shell nanoparticles by dye molecule sensitization *J. Colloid Interface Sci.* **486** 121–7
- Xu J, Sun M, Kuang Y, Bi H, Liu B, Yang D, Lv R, Gai S, He F and Yang P 2017 Markedly enhanced up-conversion luminescence by combining IR-808 dye sensitization and core-shell-shell structures *Dalt. Trans.* **46** 1495–501
- Shan G, Weissleder R and Hilderbrand S A 2013 Upconverting organic dye doped core-shell nano-composites for dual-modality NIR imaging and photo-thermal therapy *Theranostics* **3** 267–74
- Garfield D J et al 2018 Enrichment of molecular antenna triplets amplifies upconverting nanoparticle emission *Nat. Photonics* **12** 402–7

Supplementary Information

Synthesis of upconversion nanoparticles

Synthesis of the precursor: In a round bottom flask, sodium oleate (9.1458 g, 30.00 mmol) was dissolved in 20 mL H₂O and 30 mL ethanol. In a centrifuge tube YCl₃·6H₂O (2.4416 g, 8.04 mmol), YbCl₃·6H₂O (0.7162 g, 1.84 mmol) and ErCl₃·6H₂O (0.0778 g, 0.2 mmol) were dissolved in a mixture of 30 mL H₂O, 70 mL ethanol and 70 mL hexane. The two solutions were mixed together and refluxed for 4h. After cooling down the yellow homogeneous solution, the product was dried with the rotary evaporator.

Synthesis of NaYF₄:20%Yb(III), 2%Er(III) (upconversion nanoparticles): The lanthanide precursor was mixed with 150 mL octadecene and 70 mL oleic acid. The solution was heated to 100°C to degas the solution and then allowed to cool to 50°C under argon. Then, 30 mL of a methanolic solution containing NaOH (1.00 g, 25.000 mmol) and NH₄F (1.48 g, 39.960 mmol) were added slowly to the precursor and the reaction mixture was stirred for 30 min at 50°C to ensure that all the fluorides were dissolved. The solution was heated to a temperature of 100°C to remove methanol. Then it was heated to 300°C and the reaction was kept at this temperature for 2.0 h under an inert atmosphere. Then the nanoparticles were sedimented by ethanol and cleaned by centrifugation.

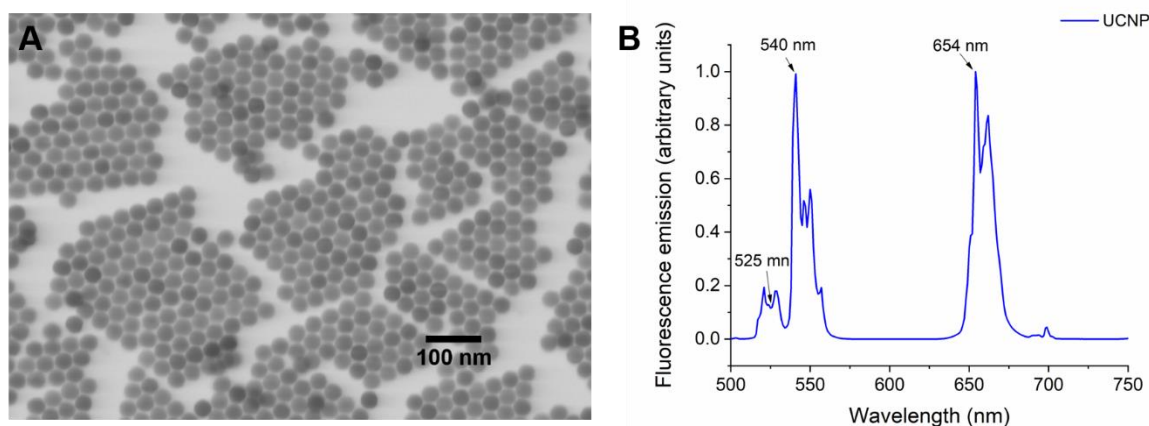


Figure S1: **A)** STEM image of NaYF₄: 20%Yb(III), 2%Er(III). STEM images were acquired on a Hitachi SU8030 EM. Images were taken with an acceleration voltage of 30 kV, average diameter estimated using fiji software is 32 nm. **B)** Upconversion fluorescence emission upon excitation at 980 nm

Inductively coupled Plasma (ICP)

ICP measurements were carried out using an iCAP 6000 Series ICP Spectrometer from Thermo Scientific with a radial optical approach. Results showed that the nanoparticles contained 81.46% ± 7.24 Yttrium, 16.43% ± 0.08 Ytterbium and 2.11% ± 0.09 Erbium.

X-ray Diffraction Spectrometry (XRD)

For XRD measurements of a minimum amount of 10 mg dried particles were used. The XRD device was an STOE Stadi P from STOE. As a Cu K α 1 radiation source, a Cu anode was used with a radiation wavelength of 1,5405 nm. The angle range of the measurements was 10-90° and with a measurement time of 120 s/0,2°.

The UCNP has a predominately hexagonal phase structure, with minority of cubic phase peaks as shown in **Figure S2**.

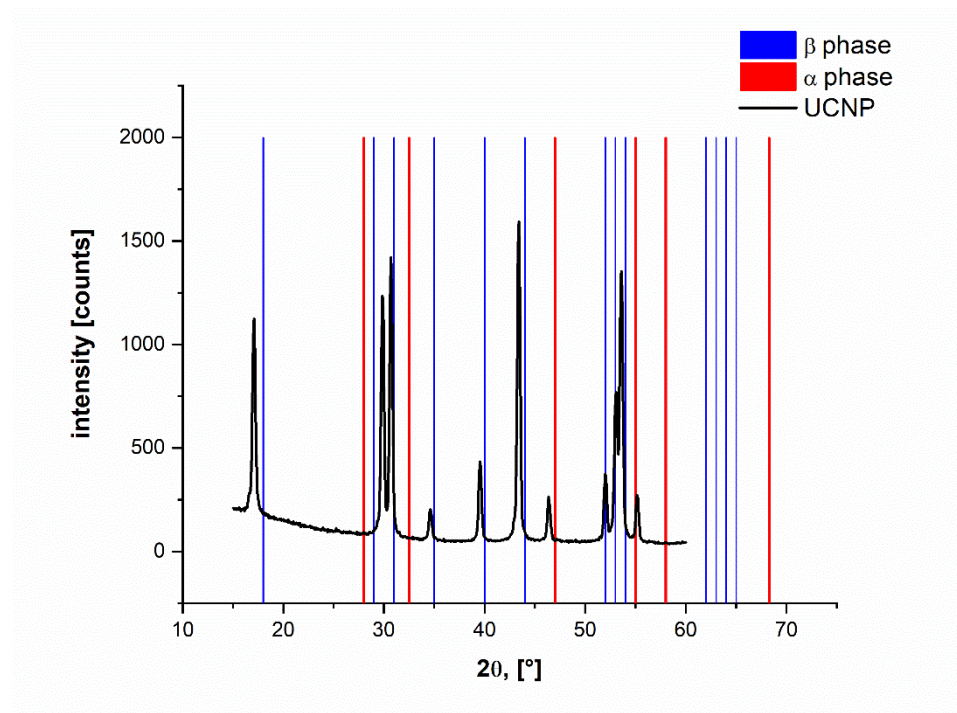


Figure S2: XRD spectrum of UCNP core

DLS measurements of the dye-UCNP micelles using Tween 80 as a surfactant revealed a hydrodynamic diameter of these micellar composites of about 200 nm that are colloiddally stable for a long enough time

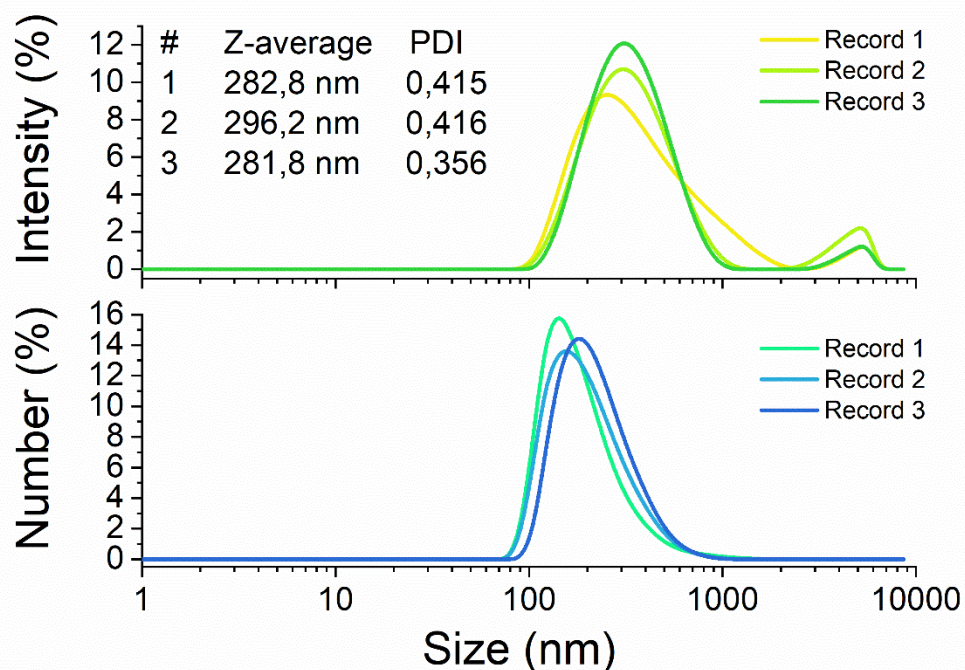


Figure S3: DLS size distribution of UCNPs – 1859 SL composite in Tween 80 shell

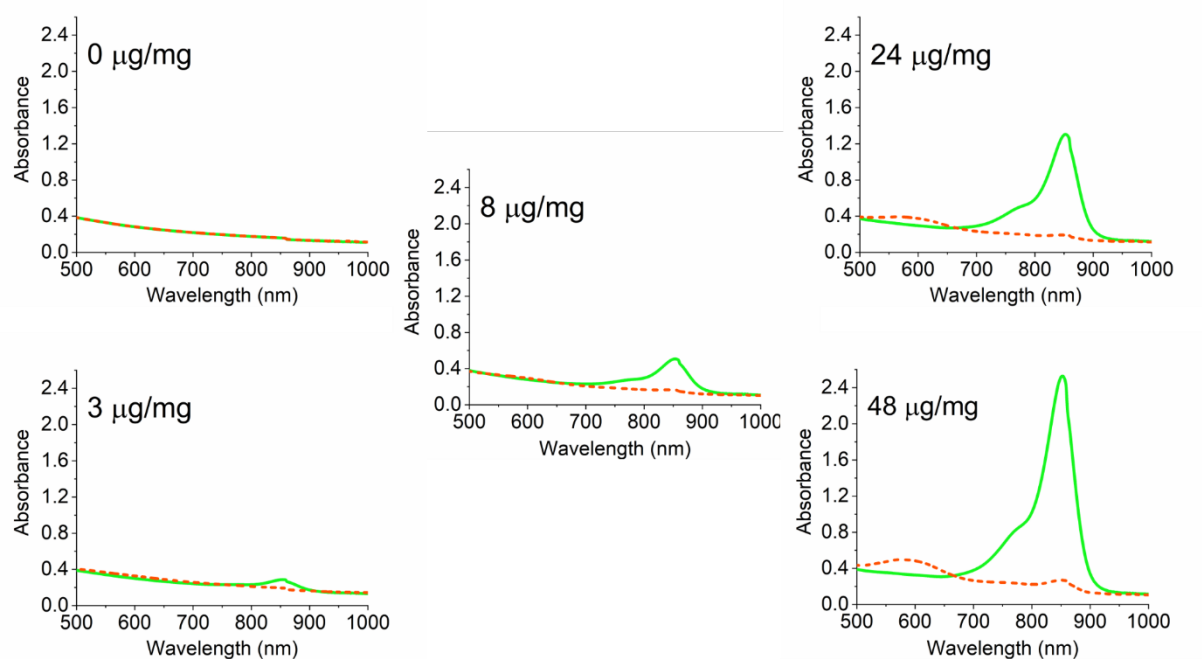


Figure S4: Absorbance spectra of the 1859 SL – UCNPs @ Tween80 system with various UCNPs to 1859 SL dye ratio before and after 808 nm laser illumination. The straight line is for the absorbance measurements prior to 808 nm excitation, the dashed line is for the absorbance measurements after 808 nm excitation. Exposure time for each sample is 44 s, and the power density is 390 W/cm². Upconversion is nonlinear, so the dependence for low power can be expected, at higher excitation, dye degradation is observed.

Relative quantum yield measurements

The absorbances of solutions of the reference dye IR-140, 1859 SL dye and J-aggregates of 1859 SL dye used for the relative QY determinations were adjusted to 0.1 at the absorbance maximum wavelength. IR-140 and 1859 SL were measured in DMSO, J-aggregates of 1859 SL were measured in deionized water.

Fluorescence spectra were recorded with a fluorescence spectrometer FSP920 from Edinburgh Instrument with a Xenon lamp as the excitation light source. All fluorescence measurements were performed with polarizers in the excitation and the emission paths at magic angle configuration (excitation and emission polarizers at 0°, and 54.8° respectively) to overcome possible emission anisotropies in recorded spectra. Slits in the excitation and emission paths were kept the same for all measurements (16 nm excitation, 8 nm emission). Dwell time and wavelength step size were 2 s and 1 nm respectively for all measurements. Excitation wavelength was 780 nm and emission scan range was 790 – 1500 nm for the 1859 SL dye and 875 nm / 900 – 1100 nm respectively for the J-aggregates. Due to the low intensity of the emission of J-aggregates, their spectra were accumulated in 6 repeats and averaged. Emission spectra of all the dyes were background corrected with emission spectra of solvents they were dissolved in.

All fluorescence spectra presented are corrected for scattered excitation light as well as for the spectral responsivity of the emission detection system and fluctuations of the excitation light source.

Relative QY were calculated according to the formula of Demas and Crosby [1], [2] (eq. 1) by taking into account the integral fluorescence $F_i(\lambda_{em})$ and absorption factor $f_i(\lambda_{ex})$ at the excitation wavelength. For the calculation of the QY of J-aggregates, the refractive indices n_i of water and DMSO were considered. Index “ref” designates the reference dye and index “x” the substance for which the QY is to be determined.

$$\Phi_x = \Phi_{ref} \cdot \frac{f_{ref}(\lambda_{ex})}{f_x(\lambda_{ex})} \frac{\int_{\lambda_{em}} F_x(\lambda_{em})}{\int_{\lambda_{em}} F_{ref}(\lambda_{em})} \frac{n_x^2}{n_{ref}^2} \quad (\text{Eq. 1})$$

The QY of reference dye IR-140 in DMSO was assumed to be 0.2 [3].

- [1] J. N. Demas and G. A. Crosby, “The Measurement of Photoluminescence Quantum Yields. A Review,” *J. Phys. Chem.*, vol. 75, no. 8, pp. 991–1024, 1971.
- [2] K. Rurack and M. Spieles, “Fluorescence quantum yields of a series of red and near-infrared dyes emitting at 600-1000 nm,” *Anal. Chem.*, vol. 83, no. 4, pp. 1232–1242, 2011.
- [3] S. Hatami *et al.*, “Absolute photoluminescence quantum yields of IR26 and IR-emissive Cd_{1-x}Hg_xTe and PbS quantum dots - method- and material-inherent challenges,” *Nanoscale*, vol. 7, no. 1, pp. 133–143, 2015.

6.2 Assessing the Protective Effects of Different Surface Coatings on NaYF₄:Yb³⁺, Er³⁺ Upconverting Nanoparticles in Buffer and DMEM

Title	Assessing the Protective Effects of Different Surface Coatings on NaYF ₄ :Yb ³⁺ , Er ³⁺ Upconverting Nanoparticles in Buffer and DMEM
Authors	Maysoon I. Saleh , Bastian Rühle, Shu Wang, Jörg Radnik, Yi You and Ute Resch-Genger
Journal	Scientific Reports. Sci Rep 10, 19318 (2020)
DOI	https://doi.org/10.1038/s41598-020-76116-z
Links	https://www.nature.com/articles/s41598-020-76116-z#citeas
Detailed scientific contribution	The concept of this manuscript was elaborated by M. Saleh, B. Rühle and U. Resch-Genger. Experiments were designed and planned by M. Saleh and B. Rühle. Synthesis of the UCNP and silica coating were done by M. Saleh, ligand removal and exchange were performed by S. Wang under the supervision of M. Saleh. Aging experiments were performed by S. Wang and M. Saleh. SIE measurements were performed by S. Wang. XPS and MS measurements were performed by J. Radnik and Y. You, respectively. All co-authors contributed to the interpretation and evaluation of the experimental results. The manuscript was mainly written by M. Saleh, B. Rühle and U. Resch-Genger.
Estimated own contribution	~ 60 %
Date of publication	09. November. 2020



OPEN

Assessing the protective effects of different surface coatings on NaYF₄:Yb³⁺, Er³⁺ upconverting nanoparticles in buffer and DMEM

Maysoon I. Saleh^{1,2}, Bastian Rühle¹, Shu Wang^{1,2}, Jörg Radnik³, Yi You⁴ & Ute Resch-Genger¹✉

We studied the dissolution behavior of β NaYF₄:Yb(20%), Er(2%) UCNP of two different sizes in biologically relevant media i.e., water (neutral pH), phosphate buffered saline (PBS), and Dulbecco's modified Eagle medium (DMEM) at different temperatures and particle concentrations. Special emphasis was dedicated to assess the influence of different surface functionalizations, particularly the potential of mesoporous and microporous silica shells of different thicknesses for UCNP stabilization and protection. Dissolution was quantified electrochemically using a fluoride ion selective electrode (ISE) and by inductively coupled plasma optical emission spectrometry (ICP OES). In addition, dissolution was monitored fluorometrically. These experiments revealed that a thick microporous silica shell drastically decreased dissolution. Our results also underline the critical influence of the chemical composition of the aqueous environment on UCNP dissolution. In DMEM, we observed the formation of a layer of adsorbed molecules on the UCNP surface that protected the UCNP from dissolution and enhanced their fluorescence. Examination of this layer by X-ray photoelectron spectroscopy (XPS) and mass spectrometry (MS) suggested that mainly phenylalanine, lysine, and glucose are adsorbed from DMEM. These findings should be considered in the future for cellular toxicity studies with UCNP and other nanoparticles and the design of new biocompatible surface coatings.

Lanthanide-doped upconversion nanoparticles (UCNP) such as NaYF₄:Yb,Er and NaYF₄:Yb,Tm have been in the focus of many studies in the last two decades due to their unique optical properties. This includes multiphotonic excitation in the near-infrared (NIR) region^{1–6}, emission of a multitude of characteristic narrow emission bands at shorter (upconversion luminescence, UCL) and longer (downshifted luminescence, DSL) wavelengths than the exciting photons⁷, long luminescence lifetimes⁸, and a high photostability⁷. These properties make them attractive fluorescent reporters for life sciences applications such as bioimaging^{9,10}, in-vitro and in-vivo detection of biomolecules^{11–14}, drug delivery¹⁵, photodynamic therapy^{2,9,10,16}, and biosensing^{2,3}. Utilization in bioimaging and cellular studies requires, however, biocompatible particles that are sufficiently stable in diluted dispersions and have no acute or chronic toxicity under application-relevant conditions^{17–21}. In the case of UCNP, this implies they should not release potentially toxic constituents such as fluoride and lanthanide ions.

UCNP are commonly synthesized in apolar solvents using hydrophobic oleic acid as a capping agent^{2,22,23}, which makes them dispersible only in apolar solvents. To render them water dispersible for applications in biological systems, they must undergo surface modification either by ligand exchange or addition of a new coating (ligand addition or encapsulation) on top of the initially present surface ligands^{24–26}. Several ligand exchange procedures have been reported so far^{24,25,27–31}, such as the exchange of the oleate ligands for polyacrylic acid (PAA)⁶, polyethylene glycol (PEG)⁷, phosphonate ligands³², citrate⁸, or removal of the oleate ligand with NOBF₄/DMF yielding “naked” UCNP stabilized with electrostatically adsorbed BF₄[−]⁹. Alternatively, silica coatings have been used that also enable further surface functionalization³³, such as the covalent attachment of targeted biomolecules

¹Federal Institute for Materials Research and Testing, Division 1.2 Biophotonics, Richard-Willstätter-Str. 11, 12489 Berlin, Germany. ²Institut Für Chemie Und Biochemie, Freie Universität Berlin, Takustrasse 3, 14195 Berlin, Germany. ³Federal Institute for Materials Research and Testing, Division 6.1, Unter den Eichen 44-46, 12203 Berlin, Germany. ⁴Federal Institute for Materials Research and Testing, Division 6.3, structural analysis, Richard-Willstätter-Str. 11, 12489 Berlin, Germany. ✉email: ute.resch@bam.de

and sensor molecules^{2,10}. UCNP surface chemistry is of considerable importance not only for shielding the lanthanide ions of the UCNP from luminescence quenching molecules that contain moieties with high energy vibrations such as $-\text{OH}$ ^{34–36}, but also for UCNP dispersibility and colloidal stability in aqueous environments and the prevention of UCNP dissolution upon dilution, thereby minimizing toxicity concerns^{21,37}. For years, UCNP were assumed to be chemically inert, due to the very low solubility products of lanthanide fluorides in water (e. g., $K_{\text{sp}} = 3.26 \times 10^{-21}$ for LaF_3)³⁸. The influence of size, surface-to-volume ratio, and surface curvature on solubility products that are usually determined for larger size powders or bulk materials was neglected. However, there appeared an increasing number of reports recently on the dissolution of UCNP like NaYF_4 -based materials in aqueous environments under high dilution conditions^{14–18}, leading to the release of fluoride and lanthanide ions^{30,39–43}. This raised concerns of UCNP biocompatibility and triggered toxicity studies¹⁷.

In this work, we studied the stability of 20 nm and 30 nm-sized $\beta\text{-NaYF}_4\text{:Yb}(20\%), \text{Er}(2\%)$ UCNP from one batch each with different surface chemistries such as polyacrylic acid (PAA) and citrate ligands as well as mesoporous and microporous silica shells in different aqueous environments. Parameters addressed besides size and surface chemistry include UCNP concentration (5 mg/L, 50 mg/L), temperature (room temperature and body temperature), and the chemical composition of typically used aqueous environments like water (neutral pH), PBS, and cell culture medium (DMEM). The release of fluoride and lanthanide ions was quantified with a fluoride ion-selective electrode (ISE) and by inductively coupled plasma optical emission spectrometry (ICP-OES), respectively. Size- and environment-sensitive upconversion luminescence (UCL) spectra and luminescence lifetimes were utilized for UCNP stability monitoring. The investigation of organic molecules adsorbed on the surface of UCNP aged in DMEM was conducted by X-ray photoelectron spectroscopy (XPS) and mass spectrometry (MS).

Experimental

Materials. Lanthanide chlorides with high purity (99.99%) were used for the synthesis of the UCNP. Sodium oleate (82%), oleic acid (90%, technical grade), octadecene (90%, technical grade), hexadecyltrimethylammonium bromide (CTAB, 98%), citric acid (99.5%), diethylene glycol (DEG, 99%), N,N-dimethyl formamide (DMF, 99.5%), nitrosyl tetrafluoroborate (95%), polyacrylic acid (MW = 1800 Da), trisodium citrate dihydrate (95%), tetraethyl orthosilicate for synthesis (98%), and ammonia solution (25% wt% in water) were obtained from Sigma Aldrich (Germany) and used without further purification. ICP standard solutions (1000 mg/L in nitric acid) used for calibration of the measurements quantifying fluoride and lanthanide ions were purchased from Sigma Aldrich. Dulbecco's Modified Eagle Medium (DMEM) (product number: D5546) was purchased from Sigma Aldrich. The detailed composition of DMEM can be found in the supplementary information (Table S2, SI). All solvents employed for the optical measurements were purchased from Sigma Aldrich in spectroscopic grade. Water refers here to Milli-Q water.

Synthesis and surface modifications of the UCNP. $\text{NaYF}_4\text{:}20\%\text{Yb}^{3+}, 2\%\text{Er}^{3+}$ UCNP were synthesized according to a previously reported procedure^{26–28} with some modifications^{25,44}. Surface modifications and silica coating experiments followed published procedures^{45–49}. The detailed synthesis and characterization of the UCNP are provided in the supplementary information (SI).

Surface modified UCNP were stored in absolute ethanol, except for bare UCNP that were stored in dimethyl formamide (DMF). Stock solutions of the different UCNP (5 mg/mL) were stored in the fridge (at 4 °C) after surface modification and prior to their use in aging studies.

Structural analysis. *Electron microscopy.* Transmission scanning electron microscopy (TSEM) images were recorded with a Hitachi SU 8030 scanning electron microscope in TSEM mode with an electron acceleration voltage of 30 kV and a current of 20 μA . A droplet of a dilute dispersion of the particles was dried on a carbon-coated copper grid (Cu 400 mesh, Quantifoil).

Zeta potential measurements. Zeta potential measurements of the surface-modified UCNP were performed with a DLS Zeta Potential Analyzer, Zetasizer Nano ZS90 (Malvern). Measurements were carried out for UCNP dispersions in MilliQ water at room temperature, the samples were placed in Zetasizer Nano ZS in capillary zeta cells DTS 1070 from Malvern Instruments.

X-ray diffraction measurements. X-ray diffraction measurements were performed with a STOE STADI P powder diffractometer with a Cu tube, a scan speed of 0.2-degree step/120 s, a tube voltage of 40 kV and a tube current of 30 mA in transmission geometry.

Absorption and fluorescence measurements. Absorption spectra were measured with a CARY 5000 absorption spectrometer (Varian) and fluorescence spectra were obtained with a calibrated FSP920 fluorescence spectrometer (Edinburgh Instruments) equipped with a xenon lamp and a 2 W 980 nm laser diode. Emission decay kinetics and lifetimes were obtained with FLS980 and FLS920 fluorescence lifetime spectrometers (Edinburgh Instruments). All measurements were carried out at room temperature in 1 cm quartz cells (Hellma) using an excitation wavelength of 976 nm and identical measurement conditions (i.e., excitation power density etc.). The lifetimes of the Yb^{3+} and Er^{3+} emission bands were obtained from the decay profiles recorded at 1010 nm and 545 nm using a tail fit with a biexponential decay. For the time-resolved UCL studies, all samples were dispersed in water and the measurements were carried out at the same excitation power density (75 W/cm²) to enable a direct comparison of the excitation power density-dependent UCL behavior.

Quantification of the components released from the UCNP. Quantification of the released lanthanide ions was carried out by ICP-OES using a Model: FHX, 76004553 spectrometer from SPECTRO Arcos-EOP. The amount of released fluoride ions was determined with a fluoride ion-selective electrode (ISE) from Metrohm AG, Switzerland.

XPS measurements. The XPS spectra of UCNP were measured with an AXIS Ultra DLD photoelectron spectrometer (Kratos Analytical, Manchester, UK) with monochromatic Al K α radiation ($E = 1486.6$ eV) at a pressure below 1×10^{-8} mbar. The electron emission angle was 0° and the source-to-analyzer angle was 60° . The binding energy scale of the instrument was calibrated following a procedure from Kratos which uses ISO 15472 binding energy data⁵⁰. XPS spectra were recorded by setting the instrument to the hybrid lens mode and the slot mode with a $300 \times 700 \mu\text{m}^2$ analysis area. Furthermore, the charge neutralizer was used. All spectra were recorded in the fixed analyzer transmission (FAT) mode. The binding energies were referenced to the C1s peak of aliphatic carbon at 285.0 eV. Before determining the peak area and fitting, the background was subtracted using a modified Toogaard background⁵¹. For the quantification, the survey spectra obtained with a pass energy of 80 eV were used. The peak intensities were corrected for the appropriate Scofield factors, the inelastic mean free path, and the intensity response function of the instrument. The maximum relative uncertainty for the composition was $\pm 20\%$. The chemical species were determined with fits of the peaks measured at high resolution (pass energy of 20 eV). For the fits, a combination of Gaussian–Lorentzian peak profiles was used⁵¹. The uncertainty of the binding energy was around ± 0.4 eV. For sample preparation, 1 mg of UCNP-Bare-20 nm was redispersed in 1 mL of DMEM for one hour at room temperature under vortex shaking, the sample was centrifuged, and the supernatant was removed. The pellet was redispersed in 10 μL of water and the solution was drop-casted on a silicon wafer (cut in about $1 \times 1 \text{ cm}^2$ shaped pieces).

MS measurements. A unit-resolution 3D ion trap mass spectrometer (Thermo LCQ Deca XP) was used to record all mass spectra. The mass range was set to m/z 50 to 450. The automatic gain control (AGC) was disabled to maintain a consistent mass-spectral acquisition rate at ~ 3 spectra/s. The injection time was set to 45 ms at 1 micro scan (without hardware averaging). The ionization method used has been previously described⁵². An in-house built device similar to a surface acoustic wave nebulizer (SAWN) was used to introduce the sample in a pulsed fashion. The sample was first mixed with methanol (HPLC grade) in a volumetric ratio of 1:2. In each sample analysis, 10 μL of the sample solution was applied on the surface of the nebulizer. The nebulizer was activated for 10 s each time. This pulsed sample introduction allowed the application of cross correlation for data processing⁵³. Analyte-related ions appeared only during this period, because the samples were introduced in a defined time window. The background ions were automatically flagged and removed from the mass spectra.

For sample preparation, 1 mg of UCNP-bare-20 was incubated in 1 mL of DMEM for 1 h at room temperature under vortex shaking (same conditions as for XPS). The sample was centrifuged, the supernatant was removed, redispersed in 100 μL of Phosphate Buffer (100 mM; pH 7.4) and incubated for 6 h at 60°C to dissolve the particles and release the adsorbed molecules from the particle surface. Afterwards, the sample was centrifuged for 15 min at 16.1 k rcf to remove insoluble components, and the supernatant was analyzed by MS.

Aging experiments. The desired amount of UCNP (0.005 mg for starting concentration of 5 mg/L or 0.05 mg for starting concentration 50 mg/L) was re-dispersed in 10 mL of the aqueous medium of interest in a 15 mL centrifuge tube, and then kept on a vortex shaker for six hours. Afterwards, the solution was centrifuged, the supernatant was collected with a pipette, the residual UCNP were re-dispersed in 10 mL of the same aqueous medium and allowed to shake on the vortex shaker for another nine hours. The supernatant was collected again, kept after each centrifugation step for ICP-OES and ISE measurements, and the same procedure was repeated for all other time points of the experiments. Additionally, the solid UCNP residue after the last time point was used for optical measurements. A schematic representation of the procedure is shown in Fig. 1.

Results and discussion

The samples studied and abbreviations used, reflecting their core size and surface chemistry, are summarized in Table 1. As summarized in Fig. 1, the as-synthesized UCNP and the surface modified UCNP were characterized by transmission scanning electron microscopy (TSEM) images, absorption and emission spectra as well as X-ray diffraction (XRD) diffractograms that are shown in the SI (Figures S1–S4). Thin (10 nm) and a thick (73 nm) microporous silica shells as well as a mesoporous silica shell (23 nm) were applied to 30 nm UCNP, and the corresponding TSEM images are shown in the SI (Figure S1). Ligand exchange was supported by zeta potential measurements as shown in the supplementary information (Table S3, SI). 20 nm and 30 nm-sized $\beta\text{-NaYF}_4:20\%\text{Yb}^{3+}, 2\%\text{Er}^{3+}$ UCNP with different surface chemistries were dispersed in concentrations of 5 and 50 mg/L in water, PBS, and DMEM and aged for time intervals of 6, 15, 24, 48, and 72 h at room temperature and at 37°C . The supernatants were collected from the samples after aging and were kept for further analysis of the released ions by ICP-OES and ISE measurements.

As the aging experiments were performed for UCNP of different core sizes, surface coatings, and starting concentrations, a direct comparison of the results based solely on the moles of released ions obtained from ICP-OES and ISE measurements can be misleading. To consider UCNP size and concentration, we therefore calculated the fractions of the number of released ions of the element of interest to the total number of ions of the same element present in the UCNP before aging for quantifying ion release and comparing the different UCNP types and aging scenarios. In the following, this quantity is referred to as “mole fraction of the element” for convenience, bearing in mind that this definition deviates from the conventional definition of a mole fraction of an element in a given chemical system.

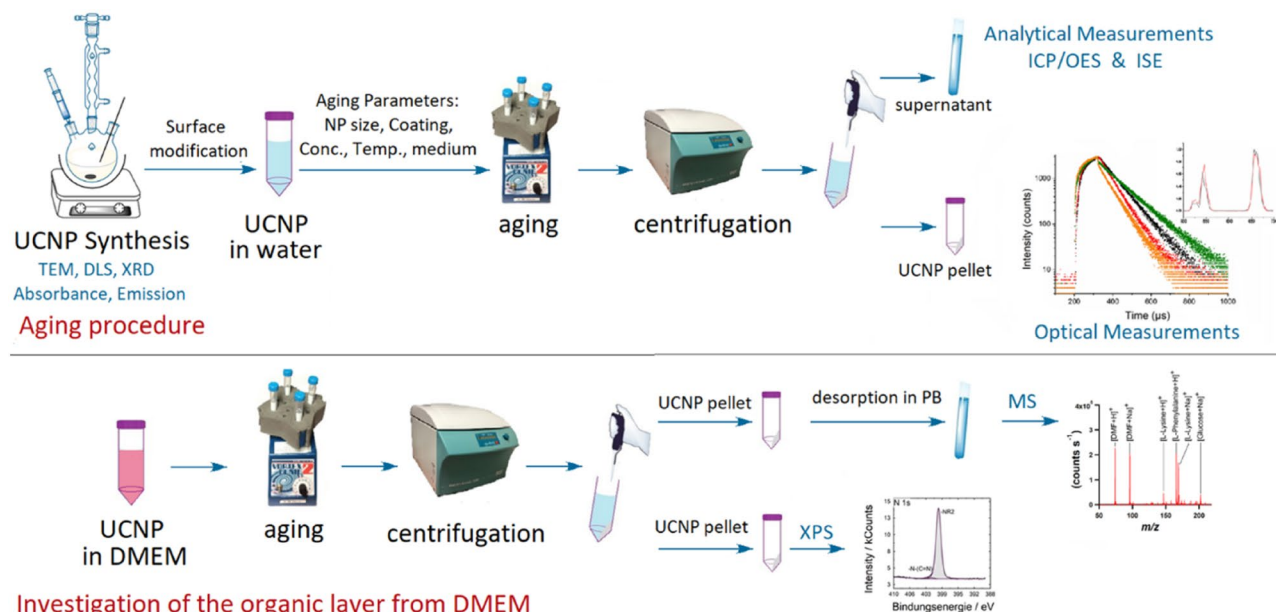


Figure 1. Schematic representation of the aging procedure used here for the different UCNP, exemplarily shown for water.

UCNP with different surface coatings		
Sample ID	Surface coating	Diameter (nm)
UC-bare-20*	BF_4^-	20
UC-bare-30*	BF_4^-	30
UC-citrate-20	Citrate	20
UC-citrate-30	Citrate	30
UC-PAA-20	Polyacrylic acid	20
UC-PAA-30	Polyacrylic acid	30
UCNP coated with silica (UCNP diameter for all samples is 30 nm)		
Sample ID	Shell porosity	Shell thickness (nm)
UC- mSiO_2 - NH_3	Mesoporous	23
UC- mSiO_2 -NaOH	Mesoporous	23
UC- SiO_2 -thin	Microporous	10
UC- SiO_2 -thick	Microporous	73

Table 1. UCNP samples used for the aging studies including terminology used. *Oleate ligands were removed and the UCNP were electrostatically stabilized by surface adsorbed BF_4^- after ligand exchange.

Influence of UCNP size and surface ligand on dissolution. The results of the stability studies with differently sized UCNP bearing either coordinatively bound surface ligands or with ligand-free (bare) UCNP are summarized in Fig. 2. As shown in Fig. 2A, ion release was observed for all UCNP regardless of their surface chemistry. Moreover, the relative percentages of the released ions were consistent with the composition of the unaged UCNP (78% Y^{3+} , 20% Yb^{3+} and 2% Er^{3+}), see Table S4, SI. Therefore, only the results of Y^{3+} and F^- are presented in the following sections. The Y^{3+} ion was chosen because it is the main constituent of the UCNP and hence its detection in the supernatant by ICP-OES can be achieved with a higher accuracy and a smaller uncertainty than the quantification of less abundant Yb^{3+} and Er^{3+} .

The fractions of the released ions clearly depended on UCNP concentration and chemical nature of the surface coatings (Figure S5, SI). 20 nm UCNP (blue bars) have a higher tendency to release lanthanide ions and dissolve than their 30 nm UCNP counterparts (orange bars) with a similar surface chemistry. The same trend was observed for the release of fluoride ions (Fig. 2B). This highlights the influence of both the surface area in contact with the surrounding medium and nanoparticle curvature. However, the influence of UCNP surface chemistry on particle dissolution was small compared to the influence of the chemical composition of the aqueous medium used for the aging studies.

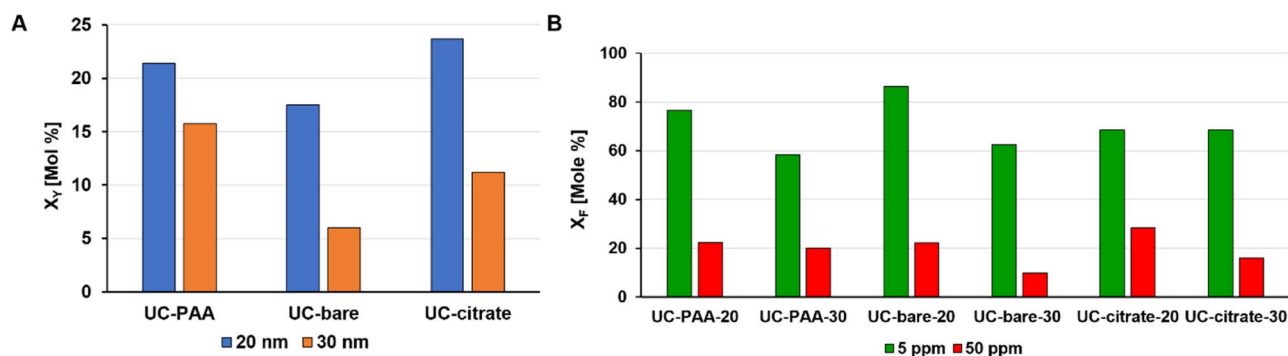


Figure 2. (A) Mole fractions of Y^{3+} released from UCNPs with different surface ligands determined for two core sizes (blue: 20 nm, orange: 30 nm) after 72 h of aging in water at room temperature. (B) Mole fractions of F^{-} released from UCNPs of different particle size and surface functionalizations determined for two different initial UCNPs concentrations (green: 5 mg/L, red: 50 mg/L). The samples were aged in water at room temperature for 72 h.

Effect of UCNPs concentration. For bare and ligand stabilized UCNPs, ion release in water was more significant for diluted UCNPs dispersions with particle concentrations of 5 mg/L compared to UCNPs dispersions containing 50 mg/L of nanoparticles. This trend was observed for all UCNPs dispersions studied regardless of UCNPs surface coating (Fig. 2B). This observation reflects the trend reported e.g., by Dukhno et al.⁵⁴, and is in agreement with observations with other types of nanoparticles like semiconductor quantum dots with coordinatively bound surface ligands that can desorb upon dilution. In principle, UCNPs dissolution can be prevented by addition of NaF, as shown by other groups^{54,55}, which shifts the dissolution equilibrium towards the solid, i.e., nanoparticle system. However, adding potentially hazardous fluoride ions is not an option for applying UCNPs in biological systems. Nanoparticle concentrations commonly used in in-vitro studies range from 1 to 100 ppm ($\mu\text{g/mL}$)^{19,20,56}. Verma et al. showed that fluoride concentrations of 120 ppm decreased cell viability up to 60%⁵⁷. Although fluoride is generally considered toxic at concentrations above 15 ppm^{41,42}, long term exposure (up to 5 days) to non-lethal fluoride concentrations as low as 5 ppb of F^{-} were shown to decrease cellular DNA synthesis and a F^{-} concentration of 38 ppb almost completely inhibited it⁴¹.

Considering that the concentration of released fluoride ions in our experiments was in the range of 1–5 ppm after incubation for 72 h in water for all samples studied here (see SI, Tables S5–S6), this confirms the concerns raised regarding the biocompatibility of bare, citrate- and PAA-stabilized UCNPs.

Shelling with meso- and microporous silica. Two different silica shells were applied, a mesoporous and a microporous silica shell. A mesoporous coating yields a highly porous silica surface which is beneficial for many life science applications^{10,15,45,58,59}, while a microporous silica shell is expected to provide a better surface protection, and consequently, a lower tendency towards core nanoparticle dissolution. For the preparation of the mesoporous silica shell, ammonia solution or sodium hydroxide were used as basic catalysts for the hydrolysis of TEOS⁶⁰. For this study, a thin (10 nm) and a thick (73 nm) microporous silica shells as well as a mesoporous silica shell (23 nm) were applied to 30 nm UCNPs and the particles were then aged under similar conditions as previously employed for UCNPs surface-stabilized with organic ligands (see Fig. 3A,B). UC-bare-30 were used as a control (see Fig. 3, red curve). As shown in Fig. 3, shelling with a mesoporous silica shell decreased UCNPs dissolution by 55% for UC- $m\text{SiO}_2\text{-NH}_3$ and 39% for UC- $m\text{SiO}_2\text{-NaOH}$ relative to the bare control sample. The number of ions released from UCNPs coated with a thick microporous silica shell was negligible, which clearly demonstrates that a thicker silica shell provided a better protection for the UCNPs against dissolution.

Effect of temperature. Subsequently, UCNPs dissolution was studied at room temperature and at 37 °C mimicking in-vitro and in-vivo conditions for the more stable silica-shelled UCNPs. Aging of the silica coated samples at body temperature was used to assess the efficiency of silica coating in dissolution prevention or inhibition for cellular and bioimaging studies. As summarized in Fig. 3C,D, dissolution is typically enhanced at a higher temperature. As expected, the dissolution of the UCNPs coated with a thin microporous or a mesoporous shell increased with increasing temperature while UCNPs coated with a thick microporous silica shell remained stable also at 37 °C.

Effect of the chemical composition of the aqueous medium. We assessed the stability of our ligand-stabilized and silica coated UCNPs in water, PBS and in DMEM (which is used in cell culture experiments). The results, summarized in Fig. 4, reveal the strongest dissolution of UCNPs in PBS, as indicated by the increased amount of released fluoride ions. This is ascribed to the high tendency of lanthanide ions to form stable complexes with phosphates and agrees well with the findings of Lisjak et al.⁶¹. However, we could not detect lanthanide ions in the supernatants after UCNPs aging in PBS. This finding is ascribed to the low solubility and precipitation of the lanthanide phosphate complexes formed. The most intriguing effects were observed for aging UCNPs with different surface chemistries in DMEM, which contains a mixture of biomolecules such as amino acids, sugars, vitamins, and salts (Table S2, SI). In this case, only very small amounts of fluoride ions

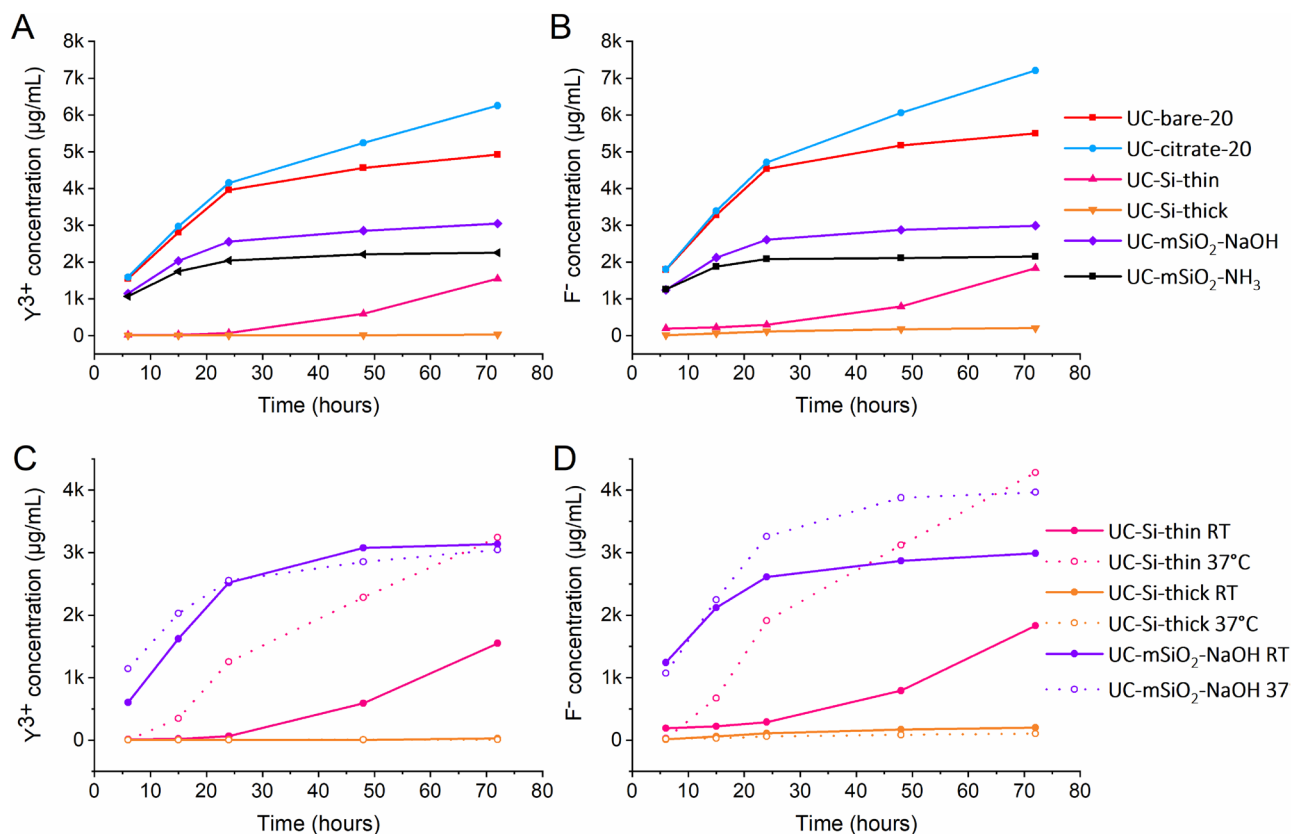


Figure 3. Comparison of the dissolution behavior of 30 nm bare UCNP (red line) to 30 nm UCNP with different silica coatings (see legend) in water at room temperature for up to 72 h and a UCNP concentration of 50 mg/L. (A) shows the Y^{3+} concentrations obtained by ICP/OES and (B) shows the concentrations of F^{-} obtained by ISE. (C) shows released Yttrium ion concentrations obtained by ICP/OES and (D) shows released fluoride ion concentrations measured by ISE. The lines are only a guide to the eye.

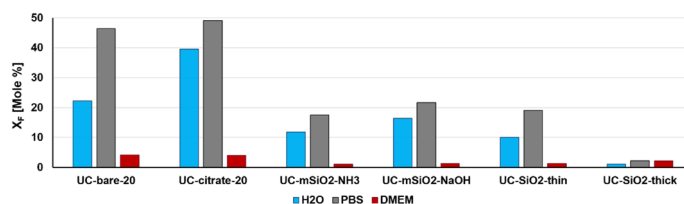


Figure 4. Mole fractions of fluoride ions released from UCNP (50 mg/L) with different surface chemistries upon aging for 72 h in different solvents: water at RT (H_2O , blue bar), PBS at RT (PBS, grey bar), and cell culture medium at 37 °C (DMEM, dark red bar).

were released for all UCNP studied as shown in Fig. 4. This strongly enhanced UCNP stability is ascribed to the formation of a protective corona of adsorbed biomolecules on the UCNP surface, similar to the formation of a protein corona observed for many nanoparticle systems in plasma and in intracellular fluids which is known to significantly affect nanoparticle toxicity^{38–43}.

Fluorescence monitoring of UCNP aging. Since UCNP dissolution causes a decrease in UCNP size⁵⁵, and the intensity and relative spectral distribution of UCL and particularly the luminescence decay kinetics of the Yb^{3+} emission depend on UCNP size and microenvironment^{23,25,34,62,63}, luminescence measurements were used to monitor UCNP dissolution. Thereby, we examined the UCL features and the downshifted Yb^{3+} emission of the fresh and aged UCNP samples varying in core size, surface chemistry, and UCNP concentration using identical instrument settings (particularly matching excitation power densities). The results of the lifetime measurements are summarized in Fig. 5, and the lifetimes are given in the SI (Table S8). As shown in Fig. 5A, aging of UCNP in water has only a small influence on the relative spectral distribution of the normalized emission spectra obtained at the same excitation power density and also on the red-to-green ratio of the Er^{3+} emission bands. Therefore, for monitoring the dissolution effects, we focused solely on measurements of the luminescence lifetimes of the Yb^{3+} and the green Er^{3+} emission excited via energy transfer upconversion (ETU) as these parameters have been

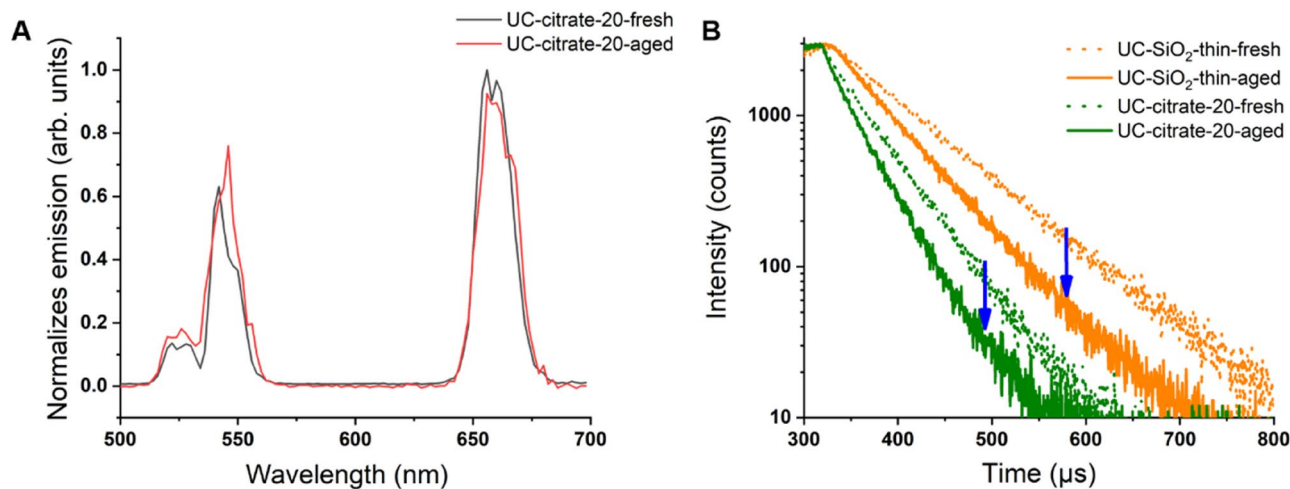


Figure 5. (A) Normalized UCL emission spectra of fresh (black line) and aged (red line) 20 nm citrate coated UCNPs excited at 976 nm and normalized to the red emission at 655 nm. (B) Decay kinetics of the Yb^{3+} luminescence of fresh (orange, dotted line) and aged (orange, solid line) UCNPs coated with a thin silica shell and stabilized with citrate (green, dotted and solid lines) excited at 976 nm and detected at 1010 nm. For the time-resolved studies, an excitation power density of 75 W/cm^2 was used. Aged samples were incubated in water for 48 h, collected by centrifugation, and then redispersed in water; fresh samples were dispersed in water and measured immediately.

previously identified to respond sensitively to aging-induced changes^{62,64}. Moreover, the decay kinetics are independent of UCNPs concentration and are more easily accessible for very dilute samples. Figure 5B highlights the noticeable dilution-induced decrease in the luminescence lifetimes of the Yb^{3+} of the aged UCNPs compared to the fresh UCNPs in water, exemplarily for 20 nm-sized UCNPs coated with citrate and a thin microporous silica shell, respectively. The variation in the lifetimes of the aged UCNPs coated with a thin silica shell compared to the lifetimes of their unaged counterparts suggests particles dissolution. Apparently, a 10 nm silica shell is not sufficient for inhibiting particle dissolution. Similar changes in luminescence decay kinetics of Yb^{3+} reflecting the trends observed in the previously discussed analytical studies were obtained for the other UCNPs samples except for aging in DMEM. Here, time-resolved luminescence measurements with UCNPs, as shown exemplarily for bare and citrate stabilized UCNPs in Fig. 6, revealed a considerable increase in the Yb^{3+} luminescence lifetime. This suggests a shielding of the UCNPs surface for the DMEM-aged samples, thereby supporting the hypothesis of the formation of a protective bio-corona on the surface of the UCNPs.

XPS and MS study of the organic surface layer formed in DMEM. To gain more information on the DMEM-induced surface modification and the DMEM components on the UCNPs surface, we subsequently analysed DMEM-aged samples with XPS and MS. First, XPS measurements of UC-bare-20 nanoparticles before and after incubation in DMEM were performed to study changes in the surface chemistry. The particles were incubated in DMEM, isolated by centrifugation, redispersed in 10 μL of water, cast on a silicon wafer, and left to dry (see also Materials and Methods section). While the transfer to water seems to cause partial dissociation of the organic layer from the UCNPs surface as revealed by lifetime measurements shown in the SI (Figure S9), parts of the adsorbed layer of DMEM constituents still remain on the particle surface as revealed by the still slightly prolonged decay behavior of the DSL compared to the starting UCNPs (see SI, Figure S9, comparison of green and blue decay curves). Hence, the organic components detected by XPS after UCNPs drying are associated with the DMEM-aged UCNPs sample. The XPS measurements after incubation in DMEM showed—besides the presence of inorganic components from the UCNPs themselves (Y^{3+} , F^- and Na^+ ions)—also the presence of new nitrogen-containing species and changes in the relative amounts of carbon and oxygen species. This is ascribed to the adsorption of organic molecules on the surface of the UCNPs (see Tables S10 and S11, SI). To further investigate the DMEM components adsorbed on the UCNPs surface, we also performed MS analyses. Again, we incubated a sample of UC-bare-20 nanoparticles in DMEM in an identical procedure to that used for preparing the XPS sample and isolated the DMEM-surface modified particles by centrifugation. Then, the molecules adsorbed on the UCNPs surface were desorbed by placing the UCNPs in phosphate buffer and the mass spectra of the resulting solution (containing the molecules desorbed in phosphate buffer) were measured. Based on the well-known chemical context of DMEM, we could assign the peaks found in the measured sample by interpreting their m/z with respect to the possible DMEM components shown in the SI (Table S2). One should bear in mind again that all organic compounds detected in the solution by MS had to come either from DMEM components that were introduced together with the sample and hence previously adsorbed on the UCNPs surface, or from traces of oleic acid or DMF that remained associated with the nanoparticle surface after the ligand exchange process. MS analysis of the supernatant led to six main peaks as shown in Fig. 7. The peaks at m/z 148 and m/z 170 were assigned to $[\text{Lysine} + \text{H}]^+$ and $[\text{Lysine} + \text{Na}]^+$, the peak at m/z 166 to $[\text{Phenylalanine} + \text{H}]^+$, and the peak at m/z 220 to $[\text{Glucose} + \text{Na}]^+$ (isobar with $[\text{myo-Inositol} + \text{Na}]^+$), respectively. Likely candidates for the peaks at m/z 74 and 96 are $[\text{Dimethylformamide} + \text{H}]^+$ and $[\text{Dimethylformamide} + \text{Na}]^+$, respectively.

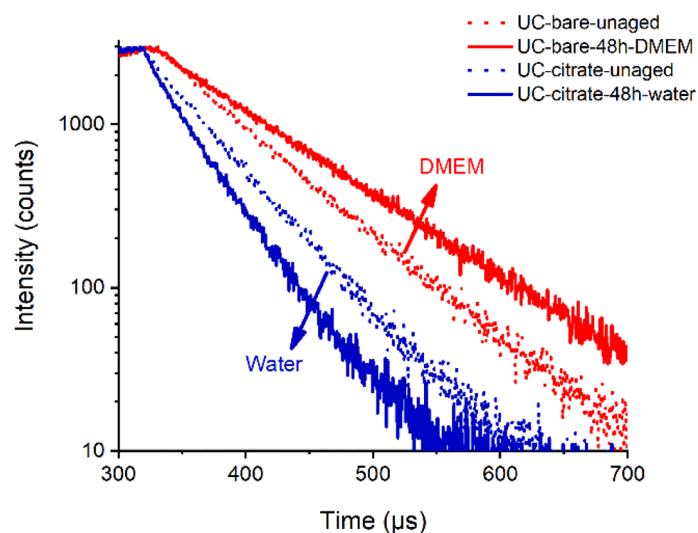


Figure 6. Decay curves of fresh (red, dotted line) and DMEM-aged (red, solid line, red) 20 nm bare UCNP and fresh (dotted line, blue) and H₂O-aged (straight line, blue) 20 nm UC-citrate nanoparticles. The aged UCNP were collected and redispersed in milli-Q water for the measurement of the decay kinetics. The Yb³⁺ emission was excited at 976 nm and detected at 1010 nm.

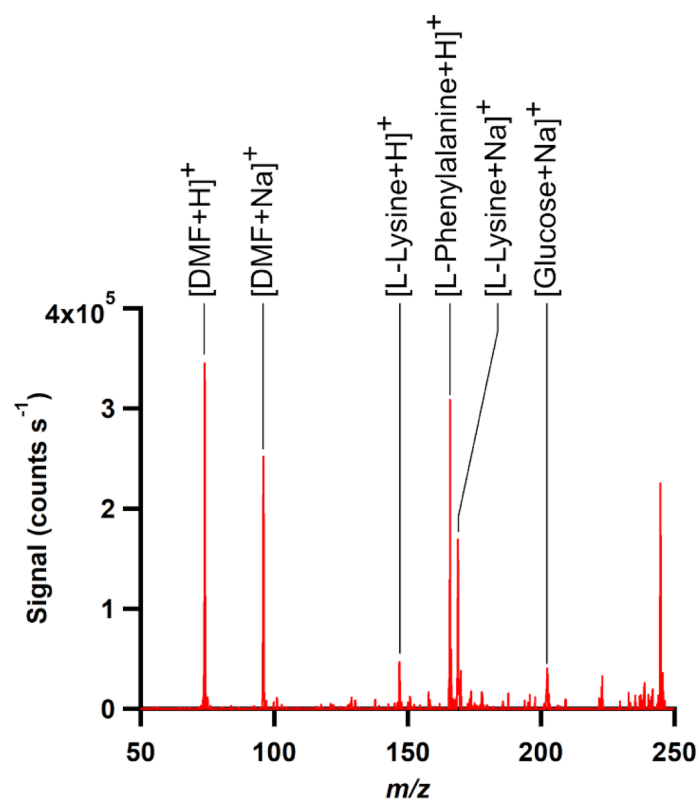


Figure 7. Mass spectrum of the aqueous solution containing components of the “corona” layer that results from incubating UCNP in DMEM.

Conclusion and outlook

We present a systematic study on the aging and dissolution of 20 nm- and 30 nm-sized β -NaYF₄:Yb,Er upconversion nanoparticles (UCNP), surface-stabilized with the coordinatively bound ligands citrate and polyacrylic acid (PAA) or with mesoporous or microporous silica shells of different thickness in water of neutral pH, phosphate buffer saline (PBS) solution, and the cell culture medium DMEM at room temperature and 37 °C.

Particle dissolution was quantified with a fluoride-selective electrode and inductively coupled plasma optical emission spectroscopy. Our results revealed that a reduced particle size, an increased temperature, and a decreased UCNP concentration, particularly for UCNP with coordinatively bound ligands, all favour UCNP dissolution. These findings agree well with the results from previous studies. Dissolution was more pronounced in PBS containing lanthanide-binding phosphate anions compared to water. Silica shelling of the UCNP surface considerably improved particle stability in water and in PBS under all conditions assessed, and a sufficiently thick microporous silica shell proved to be able to protect UCNP from dissolution. Here, further studies are required to optimize the thickness of the silica shell regarding optimum protection with minimum thickness, as the size of a nanoparticle can be an important parameter for many biological and bioanalytical applications.

Surprisingly, DMEM led to a strong stabilization of all UCNP. This was ascribed to the formation of a surface-shielding bio-corona of adsorbed DMEM constituents that prevented the release of detectable amounts of fluoride and lanthanide ions. The formation of such a bio-corona was supported by an increase in the lifetime of the downshifted Yb³⁺ emission which is known to respond strongly to the presence of nearby surface quenchers containing high energy vibrations, such as water molecules. XPS measurements revealed the presence of a high percentage of carbon, oxygen, and nitrogen on the UCNP surface, originating from organic DMEM compounds. Mass spectrometry measurements further suggested that phenylalanine, lysine, and glucose are the main DMEM constituents that adsorb on the surface of the UCNP. Further in depth-studies of the formation and identity of this corona layer, as well as its utilization to engineer new surface coatings based on similar motifs will be done in the future for developing protective biocompatible coatings.

Moreover, our findings concerning the formation of a surface protective layer originating from DMEM on the UCNP have a large impact on the interpretation of cytotoxicity studies of nanoparticles that normally use nanoparticles dispersed in cell culture medium prior to their incubation with cells. For example, this could possibly explain the low cytotoxicity of UCNP previously reported in the literature, despite the fact that the same particles show non-negligible dissolution and release of potentially harmful ions such as Fluoride and heavy metals in water and buffer up to levels that might cause cytotoxic effects. This suggests that further in-vitro and in-vivo studies are required to draw conclusions about the UCNP cytotoxicity.

Received: 29 July 2020; Accepted: 15 September 2020

Published online: 09 November 2020

References

- Haase, M. & Schäfer, H. Upconverting nanoparticles. *Angew. Chem. Int. Ed. Engl.* **50**, 5808–5829. <https://doi.org/10.1002/anie.201005159> (2011).
- Wang, F., Banerjee, D., Liu, Y., Chen, X. & Liu, X. Upconversion nanoparticles in biological labeling, imaging, and therapy. *Analyst* **135**, 1839–1854. <https://doi.org/10.1039/c0an00144a> (2010).
- Chen, G., Qiu, H., Prasad, P. N. & Chen, X. Upconversion nanoparticles: design, nanochemistry, and applications in theranostics. *Chem. Rev.* **114**, 5161–5214. <https://doi.org/10.1021/cr400425h> (2014).
- Wang, F. & Liu, X. Recent advances in the chemistry of lanthanide-doped upconversion nanocrystals. *Chem. Soc. Rev.* **38**, 976–989. <https://doi.org/10.1039/b809132n> (2009).
- Auzel, F. Upconversion and Anti-Stokes Processes with f and d Ions in Solids. *Chem. Rev.* **104**, 139–173 (2004).
- Qian, H.-S. & Zhang, Y. Synthesis of hexagonal-phase core-shell NaYF₄ nanocrystals with tunable upconversion fluorescence. *Langmuir* **24**, 12123–12125 (2008).
- Resch-Genger, U. & Gorris, H. H. Perspectives and challenges of photon-upconversion nanoparticles - Part I: routes to brighter particles and quantitative spectroscopic studies. *Anal. Bioanal. Chem.* **409**, 5855–5874. <https://doi.org/10.1007/s00216-017-0499-z> (2017).
- Heng Qin, D. W., Juna, S., Xiangyu, X., Mary, R. & Fang, X. Tuning the upconversion photoluminescence lifetimes of NaYF₄:Yb³⁺, Er³⁺ through lanthanide Gd³⁺ doping. *Sci. Rep.* <https://doi.org/10.1038/s41598-018-30983-9> (2018).
- Gorris, H. H. & Resch-Genger, U. Perspectives and challenges of photon-upconversion nanoparticles - Part II: bioanalytical applications. *Anal. Bioanal. Chem.* **409**, 5875–5890. <https://doi.org/10.1007/s00216-017-0482-8> (2017).
- Liu, J., Li, C. & Li, F. Fluorescence turn-on chemodosimeter-functionalized mesoporous silica nanoparticles and their application in cell imaging. *J. Mater. Chem.* **21**, 13163–13167. <https://doi.org/10.1039/c1jm10803d> (2011).
- Alonso-de Castro, S. *et al.* Functionalizing NaGdF₄:Yb, Er upconverting nanoparticles with bone-targeting phosphonate ligands: imaging and in vivo biodistribution. *Inorganics* <https://doi.org/10.3390/inorganics7050060> (2019).
- Del Rosal, B. & Jaque, D. Upconversion nanoparticles for in vivo applications: limitations and future perspectives. *Methods Appl Fluoresc.* **7**, 022001. <https://doi.org/10.1088/2050-6120/ab029f> (2019).
- Generalova, A. N. *et al.* PEG-modified upconversion nanoparticles for in vivo optical imaging of tumors. *RSC Adv.* **6**, 30089–30097. <https://doi.org/10.1039/c5ra25304g> (2016).
- Park, Y. I., Lee, K. T., Suh, Y. D. & Hyeon, T. Upconverting nanoparticles: a versatile platform for wide-field two-photon microscopy and multi-modal in vivo imaging. *Chem. Soc. Rev.* **44**, 1302–1317. <https://doi.org/10.1039/c4cs00173g> (2015).
- Liu, J., Bu, W., Pan, L. & Shi, J. NIR-triggered anticancer drug delivery by upconverting nanoparticles with integrated azobenzene-modified mesoporous silica. *Angew. Chem. Int. Ed. Engl.* **52**, 4375–4379. <https://doi.org/10.1002/anie.201300183> (2013).
- Peng, J. *et al.* Polyphosphoric acid capping radioactive/upconverting NaLuF₄:Yb, Tm, 153Sm nanoparticles for blood pool imaging in vivo. *Biomaterials* **34**, 9535–9544. <https://doi.org/10.1016/j.biomaterials.2013.07.098> (2013).
- Oliveira, H. *et al.* Critical considerations on the clinical translation of upconversion Nanoparticles (UCNPs): recommendations from the European Upconversion Network (COST Action CM1403). *Adv. Healthc. Mater.* **8**, e1801233. <https://doi.org/10.1002/adhm.201801233> (2019).
- Abdul Jalil, R. & Zhang, Y. Biocompatibility of silica coated NaYF₄ upconversion fluorescent nanocrystals. *Biomaterials* **29**, 4122–4128. <https://doi.org/10.1016/j.biomaterials.2008.07.012> (2008).
- Gnach, A., Lipinski, T., Bednarkiewicz, A., Rybka, J. & Capobianco, J. A. Upconverting nanoparticles: assessing the toxicity. *Chem. Soc. Rev.* **44**, 1561–1584. <https://doi.org/10.1039/c4cs00177j> (2015).
- Wysokinska, E. *et al.* Toxicity mechanism of low doses of NaGdF₄:Yb(3+), Er(3+) upconverting nanoparticles in activated macrophage cell lines. *Biomolecules* <https://doi.org/10.3390/biom9010014> (2019).
- Feng, W., Zhu, X. & Li, F. Recent advances in the optimization and functionalization of upconversion nanomaterials for in vivo bioapplications. *NPG Asia Mater.* **5**, e75–e75. <https://doi.org/10.1038/am.2013.63> (2013).

22. Li, Z., Zhang, Y. & Jiang, S. Multicolor core/shell-structured upconversion fluorescent nanoparticles. *Adv. Mater.* **20**, 4765–4769. <https://doi.org/10.1002/adma.200801056> (2008).
23. Wang, F. *et al.* Simultaneous phase and size control of upconversion nanocrystals through lanthanide doping. *Nature* **463**, 1061–1065. <https://doi.org/10.1038/nature08777> (2010).
24. Andresen, E., Resch-Genger, U. & Schaferling, M. Surface modifications for photon-upconversion-based energy-transfer nanoprobes. *Langmuir* **35**, 5093–5113. <https://doi.org/10.1021/acs.langmuir.9b00238> (2019).
25. Wilhelm, S. *et al.* Water dispersible upconverting nanoparticles: effects of surface modification on their luminescence and colloidal stability. *Nanoscale* **7**, 1403–1410. <https://doi.org/10.1039/c4nr05954a> (2015).
26. Himmelstoss, S. F. & Hirsch, T. A critical comparison of lanthanide based upconversion nanoparticles to fluorescent proteins, semiconductor quantum dots, and carbon dots for use in optical sensing and imaging. *Methods Appl. Fluoresc.* **7**, 022002. <https://doi.org/10.1088/2050-6120/ab0bfa> (2019).
27. Sedlmeier, A. & Gorris, H. H. Surface modification and characterization of photon-upconverting nanoparticles for bioanalytical applications. *Chem. Soc. Rev.* **44**, 1526–1560. <https://doi.org/10.1039/c4cs00186a> (2015).
28. Himmelstoß, S. F. & Hirsch, T. Long-term colloidal and chemical stability in aqueous media of NaYF₄-type upconversion nanoparticles modified by ligand-exchange. *Particle Particle Syst. Charact.* <https://doi.org/10.1002/ppsc.201900235> (2019).
29. Estebanez, N., Gonzalez-Bejar, M. & Perez-Prieto, J. Polysulfonate cappings on upconversion nanoparticles prevent their disintegration in water and provide superior stability in a highly acidic medium. *ACS Omega* **4**, 3012–3019. <https://doi.org/10.1021/acsomega.8b03015> (2019).
30. Plohl, O. *et al.* Amphiphilic coatings for the protection of upconverting nanoparticles against dissolution in aqueous media. *Dalton Trans.* **46**, 6975–6984. <https://doi.org/10.1039/c7dt00529f> (2017).
31. Dutta, J. & Rai, V. K. APTES modified GO-PEI-Er³⁺/Yb³⁺: NaYF₄ upconverting nanoparticles hybrid film-based optical pH sensor and NIR photoelectric response. *IEEE Sens. J.* **19**, 3609–3615. <https://doi.org/10.1109/jsen.2019.2892785> (2019).
32. 32Ruibin Li, Z. J., Juyao, D., Chong Hyun, C., Xiang, W., Bingbing, S., Meiyang, W., Yu-Pei, L., Jeffrey, I. Z., Andre, E. N., Tian, X. Enhancing the imaging and biosafety of upconversion nanoparticles through phosphonate coating. *ACS Nano* **9** (2015).
33. Mondal, M., Rai, V. K. & Srivastava, C. Influence of silica surface coating on optical properties of Er³⁺-Yb³⁺:YMoO₄ upconverting nanoparticles. *Chem. Eng. J.* **327**, 838–848. <https://doi.org/10.1016/j.cej.2017.06.166> (2017).
34. Arppe, R. *et al.* Quenching of the upconversion luminescence of NaYF₄(4):Yb(3)(+), Er(3)(+) and NaYF₄(4):Yb(3)(+), Tm(3)(+) nanophosphors by water: the role of the sensitizer Yb(3)(+) in non-radiative relaxation. *Nanoscale* **7**, 11746–11757. <https://doi.org/10.1039/c5nr02100f> (2015).
35. Wurth, C. *et al.* Excitation power dependent population pathways and absolute quantum yields of upconversion nanoparticles in different solvents. *Nanoscale* **9**, 4283–4294. <https://doi.org/10.1039/c7nr00092h> (2017).
36. Wurth, C., Fischer, S., Grauel, B., Alivisatos, A. P. & Resch-Genger, U. Quantum yields, surface quenching, and passivation efficiency for ultrasmall core/shell upconverting nanoparticles. *J. Am. Chem. Soc.* **140**, 4922–4928. <https://doi.org/10.1021/jacs.8b01458> (2018).
37. Xiao, Q. *et al.* Rational design of a thermalresponsive-polymer-switchable FRET system for enhancing the temperature sensitivity of upconversion nanophosphors. *Nanoscale* **6**, 10179–10186. <https://doi.org/10.1039/c4nr02497d> (2014).
38. Itoh Hisako, H. H. Tsuchiya masashi, suzuki yasuo, asano yasukazu determination of solubility products of rare earth fluorides by fluoride ion-selective electrode. *Bull. Chem. Soc. Jpn.* **57**, 1689–1690 (1984).
39. Barbier, O., Arreola-Mendoza, L. & Del Razo, L. M. Molecular mechanisms of fluoride toxicity. *Chem. Biol. Interact.* **188**, 319–333. <https://doi.org/10.1016/j.cbi.2010.07.011> (2010).
40. 40Palmer, R. J. & Stevens, J. B. Cytotoxicity of the rare earth metals cerium, lanthanum, and neodymium in vitro: comparisons with cadmium in a pulmonary macrophage primary culture system. *Environ. Res.* **43** (1987).
41. Chang, Y. C. & Chou, M. Y. Cytotoxicity of fluoride on human pulp cell cultures in vitro. *Oral Surg. Oral Med. Oral Pathol. Oral Radiol. Endod.* **91**, 230–234. <https://doi.org/10.1067/moe.2001.111757> (2001).
42. Salomao, P. M. A. *et al.* The cytotoxic effect of TiF₄ and NaF on fibroblasts is influenced by the experimental model, fluoride concentration and exposure time. *PLoS ONE* **12**, e0179471. <https://doi.org/10.1371/journal.pone.0179471> (2017).
43. Lisjak, D., Plohl, O., Ponikvar-Svet, M. & Majaron, B. Dissolution of upconverting fluoride nanoparticles in aqueous suspensions. *RSC Adv.* **5**, 27393–27397. <https://doi.org/10.1039/c5ra00902b> (2015).
44. Radunz, S. *et al.* Evolution of size and optical properties of upconverting nanoparticles during high-temperature synthesis. *J. Phys. Chem. C* **122**, 28958–28967. <https://doi.org/10.1021/acs.jpcc.8b09819> (2018).
45. Li, C., Liu, J., Alonso, S., Li, F. & Zhang, Y. Upconversion nanoparticles for sensitive and in-depth detection of Cu²⁺ ions. *Nanoscale* **4**, 6065–6071. <https://doi.org/10.1039/c2nr31570j> (2012).
46. Dong, A. *et al.* A generalized ligand-exchange strategy enabling sequential surface functionalization of colloidal nanocrystals. *J. Am. Chem. Soc.* **133**, 998–1006. <https://doi.org/10.1021/ja108948z> (2011).
47. Carron, S. *et al.* Assembly of near infra-red emitting upconverting nanoparticles and multiple Gd(III)-chelates as a potential bimodal contrast agent for MRI and optical imaging. *Dalton Trans.* **44**, 11331–11339. <https://doi.org/10.1039/c5dt00919g> (2015).
48. Juan, J., Cheng, L., Shi, M., Liu, Z. & Mao, X. Poly-(allylamine hydrochloride)-coated but not poly(acrylic acid)-coated upconversion nanoparticles induce autophagy and apoptosis in human blood cancer cells. *J. Mater. Chem. B* **3**, 5769–5776. <https://doi.org/10.1039/c5tb00646e> (2015).
49. Kembuan, C., Saleh, M., Rühle, B., Resch-Genger, U. & Graf, C. Coating of upconversion nanoparticles with silica nanoshells of 5–250 nm thickness. *Beilstein J. Nanotechnol.* **10**, 2410–2421. <https://doi.org/10.3762/bjnano.10.231> (2019).
50. 50In 15472:2010 (Geneva, 2010).
51. Hesse, R. & Denecke, R. Improved Tougaard background calculation by introduction of fittable parameters for the inelastic electron scattering cross-section in the peak fit of photoelectron spectra with UNIFIT 2011. *Surf. Interface Anal.* **43**, 1514–1526. <https://doi.org/10.1002/sia.3746> (2011).
52. Song, L., You, Y. & Evans-Nguyen, T. Surface acoustic wave nebulization with atmospheric-pressure chemical ionization for enhanced ion signal. *Anal. Chem.* **91**, 912–918. <https://doi.org/10.1021/acs.analchem.8b03927> (2019).
53. You, Y., Badal, S. P. & Shelley, J. T. Automatic analyte-ion recognition and background removal for ambient mass-spectrometric data based on cross-correlation. *J. Am. Soc. Mass Spectrom.* **30**, 1720–1732. <https://doi.org/10.1007/s13361-019-02246-y> (2019).
54. Dukhno, O. *et al.* Time-dependent luminescence loss for individual upconversion nanoparticles upon dilution in aqueous solution. *Nanoscale* **10**, 15904–15910. <https://doi.org/10.1039/c8nr03892a> (2018).
55. Lahtinen, S. *et al.* Disintegration of hexagonal NaYF₄:Yb³⁺, Er³⁺ upconverting nanoparticles in aqueous media: the role of fluoride in solubility equilibrium. *J. Phys. Chem. C* **121**, 656–665. <https://doi.org/10.1021/acs.jpcc.6b09301> (2016).
56. Guller, A. E. *et al.* Cytotoxicity and non-specific cellular uptake of bare and surface-modified upconversion nanoparticles in human skin cells. *Nano Res.* **8**, 1546–1562. <https://doi.org/10.1007/s12274-014-0641-6> (2015).
57. Verma, A., Ali, D. & Pathak, A. K. Fluoride induces DNA damage and cytotoxicity in human hepatocellular carcinoma cells. *Toxicol. Environ. Chem.* **99**, 148–159. <https://doi.org/10.1080/02772248.2016.1155380> (2017).
58. Argyo, C., Weiss, V., Bräuchle, C. & Bein, T. Multifunctional mesoporous silica nanoparticles as a universal platform for drug delivery. *Chem. Mater.* **26**, 435–451. <https://doi.org/10.1021/cm402592t> (2013).
59. Qian, H. S., Guo, H. C., Ho, P. C., Mahendran, R. & Zhang, Y. Mesoporous-silica-coated up-conversion fluorescent nanoparticles for photodynamic therapy. *Small* **5**, 2285–2290. <https://doi.org/10.1002/smll.200900692> (2009).

60. Li, Z., Jia, L., Li, Y., He, T. & Li, X.-M. Ammonia-free preparation of Ag@SiO₂ core/shell nanoparticles. *Appl. Surf. Sci.* **345**, 122–126. <https://doi.org/10.1016/j.apsusc.2015.03.159> (2015).
61. Lisjak, D., Plohl, O., Vidmar, J., Majaron, B. & Ponikvar-Svet, M. Dissolution mechanism of upconverting AYF₄:Yb, Tm (A = Na or K) nanoparticles in aqueous media. *Langmuir* **32**, 8222–8229. <https://doi.org/10.1021/acs.langmuir.6b02675> (2016).
62. Plohl, O. *et al.* Optically detected degradation of NaYF₄:Yb, Tm-based upconversion nanoparticles in phosphate buffered saline solution. *Langmuir* **33**, 553–560. <https://doi.org/10.1021/acs.langmuir.6b03907> (2017).
63. Wang, F., Wang, J. & Liu, X. Direct evidence of a surface quenching effect on size-dependent luminescence of upconversion nanoparticles. *Angew. Chem. Int. Ed. Engl.* **49**, 7456–7460. <https://doi.org/10.1002/anie.201003959> (2010).
64. Andresen, E., Wurth, C., Prinz, C., Michaelis, M. & Resch-Genger, U. Time-resolved luminescence spectroscopy for monitoring the stability and dissolution behaviour of upconverting nanocrystals with different surface coatings. *Nanoscale* <https://doi.org/10.1039/d0nr02931a> (2020).

Acknowledgements

This work was supported by The European Upconversion Network as a part of the European Association in Science and Technology (COST). XRD measurements were done by Michael Labza in the Institute of Chemistry of Freie Universität (FU) Berlin. ICP-OES measurements were performed by Janina Roik, Division 1.6, Federal Institute for Materials Research and Testing (BAM). URG and MIS gratefully acknowledge financial support from the grant RE1203/20-1 (M-Eranet project NANOHYPER; German Research Council (DFG)). The authors have declared that no conflicting interests exist. SEM measurements were performed in collaboration with the Research Center for Electron Microscopy and Core Facility “BioSupraMol” at the Institute of Chemistry and Biochemistry, Freie Universität Berlin.

Author contributions

The manuscript was written through contributions of all authors. All authors have given approval to the final version of the manuscript.

Funding

Open Access funding enabled and organized by Projekt DEAL.

Competing interests

The authors declare no competing interests.

Additional information

Supplementary information is available for this paper at <https://doi.org/10.1038/s41598-020-76116-z>.

Correspondence and requests for materials should be addressed to U.R.-G.

Reprints and permissions information is available at www.nature.com/reprints.

Publisher's note Springer Nature remains neutral with regard to jurisdictional claims in published maps and institutional affiliations.



Open Access This article is licensed under a Creative Commons Attribution 4.0 International License, which permits use, sharing, adaptation, distribution and reproduction in any medium or format, as long as you give appropriate credit to the original author(s) and the source, provide a link to the Creative Commons licence, and indicate if changes were made. The images or other third party material in this article are included in the article's Creative Commons licence, unless indicated otherwise in a credit line to the material. If material is not included in the article's Creative Commons licence and your intended use is not permitted by statutory regulation or exceeds the permitted use, you will need to obtain permission directly from the copyright holder. To view a copy of this licence, visit <http://creativecommons.org/licenses/by/4.0/>.

© The Author(s) 2020

Supplementary Information of

Assessing the Protective Effects of Different Surface Coatings on NaYF₄:Yb³⁺, Er³⁺ Upconverting Nanoparticles in Buffer and DMEM

Maysoon I. Saleh^{a,b}, Bastian Rühle^a, Shu Wang^{a,b}, Jörg Radnik^c, Yi You^d and Ute Resch-Genger^{a,*}

- a.* Federal Institute for Materials Research and Testing, Division 1.2 Biophotonics, Richard-Willstätter-Str. 11, 12489 Berlin, Germany.
Email: ute.resch@bam.de
- b.* Institut für Chemie und Biochemie, Freie Universität Berlin, Takustrasse 3, D-14195 Berlin, Germany.
- c.* Federal Institute for Materials Research and Testing, Division 6.1, Unter den Eichen 44-46, 12203 Berlin, Germany.
- d.* Federal Institute for Materials Research and Testing, Division 6.3, structural analysis, Richard-Willstätter-Str. 11, 12489 Berlin, Germany.

Table of Contents

1. Synthesis of Upconversion Nanoparticles (UCNP)	2
2. Surface Modification of UCNP	3
3. Components of DMEM	5
4. Characterization of UCNP (TSEM, XRD, DLS, Absorption and Emission)	6
5. Analytical Measurements for the Detection of the Released Ions	9
6. Luminescence Lifetime Measurements	12
7. X-ray Photoelectron Spectroscopic Measurements Results	15
8. References	16

1. Synthesis of Upconversion Nanoparticles (UCNP)

Upconversion nanoparticles (UCNP) were prepared via a thermal decomposition method, with some modification to published procedures.¹⁻³ This synthesis was done in two steps: Preparation of the nanoparticle precursors, and then high temperature growth of the nanoparticles.

1. Synthesis of the precursor: In a round-bottom flask, sodium oleate (9.146 g, 30.00 mmol) was dissolved in a mixture of 20 ml of H₂O and 30 mL of ethanol. In a centrifuge tube YCl₃·6H₂O (2.442 g, 8.04 mmol), YbCl₃·6H₂O (0.716 g, 1.84 mmol) and ErCl₃·6H₂O (0.078 g, 0.2 mmol) were dissolved in a mixture of 30 mL of H₂O, 70 mL of ethanol and 70 mL of cyclohexane. The two solutions were mixed and heated under reflux for 4h. After cooling the resulting yellow homogeneous solution to RT, the product was dried and collected using a rotary evaporator.

2. Synthesis of NaYF₄:20%Yb³⁺,2%Er³⁺ (UCNP): The lanthanide precursor was dissolved in a solution of 150 mL of 1-octadecene and 70 mL of oleic acid. The solution was heated to 100°C to degas, and then allowed to cool to 50°C under argon. Then, 30 mL of a methanolic solution containing NaOH (1.00 g, 25.000 mmol) and NH₄F (1.48 g, 39.960 mmol) were added slowly to the precursor and the reaction mixture was stirred for 30 min at 50°C to ensure that all the fluorides were dissolved. The solution was heated to 100°C to remove methanol, then it was heated to 300°C and the reaction was kept at this temperature for 2.0 h under an inert atmosphere of Ar. After that, the reaction solution was allowed to cool, and the nanoparticles were precipitated with ethanol and isolated by centrifugation.

Modification to the first procedure

Throughout the course of work, the synthesis of UCNP was modified.^{4,5} The modified approach also produced monodisperse, bright nanoparticles, but the reproducibility in obtaining the desired size of the nanoparticles was improved by controlling the reaction time based on the use of a portable 980 nm diode laser. Both procedures shared the first step of preparing the precursor, with some changes to the formation of the nanoparticles in the second procedure.

The dry precursor was dissolved in 70 mL of oleic acid and 150 mL of 1-octadecene and heated to 160 °C under argon. After 30 minutes, a clear solution was formed and then the reaction solution was degassed under vacuum using a Schlenk line. The reaction mixture was cooled to room temperature and then 35 mL of a methanolic solution of NaOH (13 mmol) and NH₄F (20 mmol) were added slowly. The suspension was stirred for 30 minutes at 120 °C under a flow of argon and then heated to 325°C (a reflux condenser was connected at the very high temperature to avoid any possible evaporation of the solvents).

The reaction was then monitored by a 980 nm laser. A green emission was observed within 10 minutes after reaching 325°C. In the beginning of the reaction, weakly emitting α-particles will form which then grow further through Ostwald ripening and form β-particles that show a very intense green emission that can readily be observed with the naked eye after 15 minutes at 325°C. At this point, the mixture was cooled to room temperature, the oleate-capped UCNP were precipitated by addition of an appropriate amount of ethanol, and the dispersion was centrifuged at 1000 g for 5 minutes. The product was redispersed three times in chloroform and reprecipitated in ethanol, and then washed with cyclohexane and acetone. The purified UCNP were stored in cyclohexane.

2. Surface Modification of UCNP

Coating of UCNP with a Mesoporous Silica Shell

a. Preparation of CTAB-stabilized UCNP

The procedure for coating the UCNP with a mesoporous silica shell was based on an approach reported in literature.⁶ In this coating process, the UCNP are first transferred to water by stabilization with CTAB (cetyltrimethylammonium bromide) prior to silica growth. 0.4 g of CTAB was dissolved in 80 mL of water, then 2 mL of UCNP suspension in cyclohexane (20 mg/mL) was added to the aqueous CTAB solution keeping the total concentration of UCNP in water at 0.5 g/mL. The mixture was stirred for 48 h at room temperature to evaporate cyclohexane and obtain the CTAB-stabilized UCNP.

b. Coating of UCNP with a mesoporous silica shell using different basic catalysts:

For the coating process, 20 mL of water, 3 mL of EtOH and 24 μ L of ammonia solution (25% w/w) were mixed in a 100 mL flask. Then, 10 mL of the CTAB-stabilized UCNPs (see above) were added to the mixture and heated to 70°C under stirring at 600 rpm. Subsequently, a mixture of 75 μ L of TEOS in 4 mL of ethanol was added by the aid of a peristaltic pump (addition rate 0.5 mL/min). The reaction was kept at 70°C for 1 h. The resulting UCNP@mSiO₂ nanoparticles were washed three times with ethanol. For the washing step, ethanol was added to the dispersion to sediment the nanoparticles and then the dispersion was centrifuged at 1108 g for 30 min.

Finally, the surfactant (CTAB) was removed from the silica shell by an ion exchange process. The mesoporous silica coated upconversion nanoparticles (UCNP@mSiO₂) were added to a solution of 50 mL of ethanol and 0.3 g of NH₄NO₃ and kept at 60°C for 2 h. The resulting UCNPs@mSiO₂ were then washed by centrifugation and stored in ethanol.

For the sample UC-mSiO₂-NaOH, the same procedure was used but 1.5 mL of 2 M sodium hydroxide was used instead of ammonia solution.

Coating of UCNP with a microporous silica shell

A microporous silica shell was synthesized using an oil-in-water microemulsion synthesis. In a centrifuge tube, upconversion nanoparticles in cyclohexane (4.74 mL, 6.6 mg/ml), 5.26 mL of cyclohexane and 0.6 mL of Igepal CO-520 were mixed by shaking, then 0.142 mL of ammonia solution (25% w/w) were added, and the mixture was mixed again by shaking the tube. The silica precursor, tetraethyl orthosilicate (TEOS, 0.142 mL; 0.637 mmol) was added into the mixture, and the mixture was kept on a vortex shaker overnight. Upconversion nanoparticles with a microporous silica shell were then sedimented and washed three times with ethanol by redispersion and centrifugation at 1108 g for 30 minutes.

Silica re-growth to form a thicker microporous silica shell

The re-growth of the silica shell on the surface of the upconversion nanoparticles was done in several steps following a published protocol.⁷⁻⁹ First, thin silica shells were grown by oil-in-water microemulsion processes as described in the previous section. In each step, the reaction mixture was kept stirring after adding TEOS for at least 12 hours, and then the next shell was formed by adding the required amount of cyclohexane, ammonia solution, Igepal CO-520 and TEOS without purification or breaking the microemulsion. Five thin shells were applied following this procedure until the final diameter of the core/shell nanoparticles was 123 nm. At this point, the nanoparticles were sedimented by ethanol and washed three times with EtOH by centrifugation, dispersed in absolute ethanol, and further coated with silica through a modified Stöber process using published protocols with some changes. Reactants amounts are listed in Table S1:

Table S1: The amounts of reactants used to produce the microporous silica shells on the surface of the upconversion nanoparticles. All syntheses of the silica shells were performed at room temperature.

Oil-in-water microemulsion synthesis of the silica shell					
Upconversion nanoparticles core diameter: 30 nm, mass: 32 mg, no. of particles: 5.45×10^{14}					
Silica shell	Cyclohexane (mL)	Igepal (mL)	NH ₃ (25%) (μL)	TEOS (μL)	Shell thickness (nm)
1	10	0.60	124	124	10
2	10	1.00	248	248	18
3	19	1.65	428	428	26
4	28	2.65	676	676	32
5	54	2.52	1420	1420	47

Modified Stöber synthesis the silica shell					
UC@SiO ₂ core diameter: 123 nm, mass: 96 mg, no. of particles: 4.78×10^{13}					
Silica shell	Ethanol (mL)	NH ₃ (25%) (μL)	TEOS (μL)	TEOS addition rate (μL/min)	Shell thickness (nm)
6	20	940	1169	700	73

Removal of the oleate ligand with NOBF₄/DMF

Upconversion nanoparticles were treated with NOBF₄ to strip off the oleate ligand according to a ligand exchange strategy reported by Dong et al.¹⁰ In detail, 10 mL of dimethylformamide (DMF) were transferred into a round bottom flask. Then, 50 mg of the oleate coated nanoparticles dispersed in 10 mL of cyclohexane were added. This resulted in a two-phase system consisting of an upper layer of cyclohexane (containing the oleate coated nanoparticles) and a lower layer of DMF. Subsequently, 120 mg (1.0 mmol) of NOBF₄ were added to the dispersion and sonicated for 20 minutes at 20°C until the DMF layer became turbid, indicating a phase transfer with the original hydrophobic oleic acid coating of the upconversion nanoparticles replaced by a layer of hydrophilic BF₄⁻. The nanoparticles within the slightly turbid DMF phase were precipitated by chloroform and collected by centrifugation (1000 g for 10 minutes). The obtained oleate-free, BF₄⁻ stabilized nanoparticles were dispersed in 10 mL of DMF.

Ligand exchange with citrate

Citrate-coated upconversion nanoparticles were prepared according to a method reported by Carron et al.¹¹ 0.2 M citric acid buffers with pH values of 3 and 6 were prepared. Then, 20 mg of the oleate capped nanoparticles were dispersed in 20 mL of a 0.2 M citric acid buffer (pH = 3) and stirred for three hours at 800 rpm to remove the oleic acid ligand. After that, the solution was extracted 3 times with cyclohexane and another 3 times with diethyl ether. The ligand-free nanoparticles were precipitated by adding an excess of acetone and collected by centrifugation (1000 g, 30 min). Afterwards, they were re-dispersed in 20 mL of a 0.2 M citric acid buffer (pH = 6) and stirred at 800 rpm for 12h. The solution was extracted three times with cyclohexane and another three times with diethyl ether. The citrate capped nanoparticles were obtained by precipitation with acetone, followed by centrifugation (1000 g, 30 min) and then redispersed in 5 mL of absolute ethanol and stored at room temperature.

Polyacrylic acid coating on UCNPs

Coating the nanoparticles with polyacrylic acid was carried out following a protocol from Juan et al.¹² 303 mg of polyacrylic acid (PAA, MW = 1800) was added to 30 mL of diethylene glycol (DEG) in a three-neck flask, and the mixture was heated to 110°C to form a clear solution. Then, 5 mL of a toluene dispersion containing 100 mg of the upconversion nanoparticles was added slowly into the PAA solution under an inert atmosphere of nitrogen while maintaining the temperature at 110 °C for 1 h.

The solution was then heated to 240°C for another 1 h. After cooling down to room temperature, the nanoparticles were precipitated by addition of ethanol, washed several times with an ethanol/water mixture (1: 1 v/v), and finally stored in absolute ethanol.

3. Components of DMEM

Table S2: Components of DMEM

DMEM Product No. D5546			
Component	g/L	Component	g/L
Inorganic Salts		L-Threonine	0.095
CaCl ₂	0.2	L-Tryptophan	0.016
Fe(NO ₃) ₃ .9H ₂ O	0.0001	Amino Acids	
MgSO ₄	0.09767	L-Tyrosine.2Na.2H ₂ O	0.10379
KCl	0.4	L-Valine	0.094
NaHCO ₃	3.7	Vitamins	
NaCl	6.4	Choline Chloride	0.004
NaH ₂ PO ₄	0.109	Folic Acid	0.004
Amino Acids		myo -Inositol	0.0072
L-Alanyl-L-Glutamine	-	Niacinamide	0.004
L-Arginine.HCl	0.084	D-Pantothenic Acid.½Ca	0.004
L-Cystine.2HCl	0.0626	Pyridoxal.HCl	-
L-Glutamine	-	Pyridoxine.HCl	0.00404
Glycine	0.03	Riboflavin	0.0004
L-Histidine.HCl.H ₂ O	0.042	Thiamine.HCl	0.004
L-Isoleucine	0.105	Other	
L-Leucine	0.105	D-Glucose	1.0
L-Lysine.HCl	0.146	HEPES	-
L-Methionine	0.03	Phenol Red.Na	0.0159
L-Phenylalanine	0.066	Pyruvic Acid.Na	0.11
L-Serine	0.042		

4. Characterization of UCNP (TSEM, XRD, DLS, Absorption and Emission)

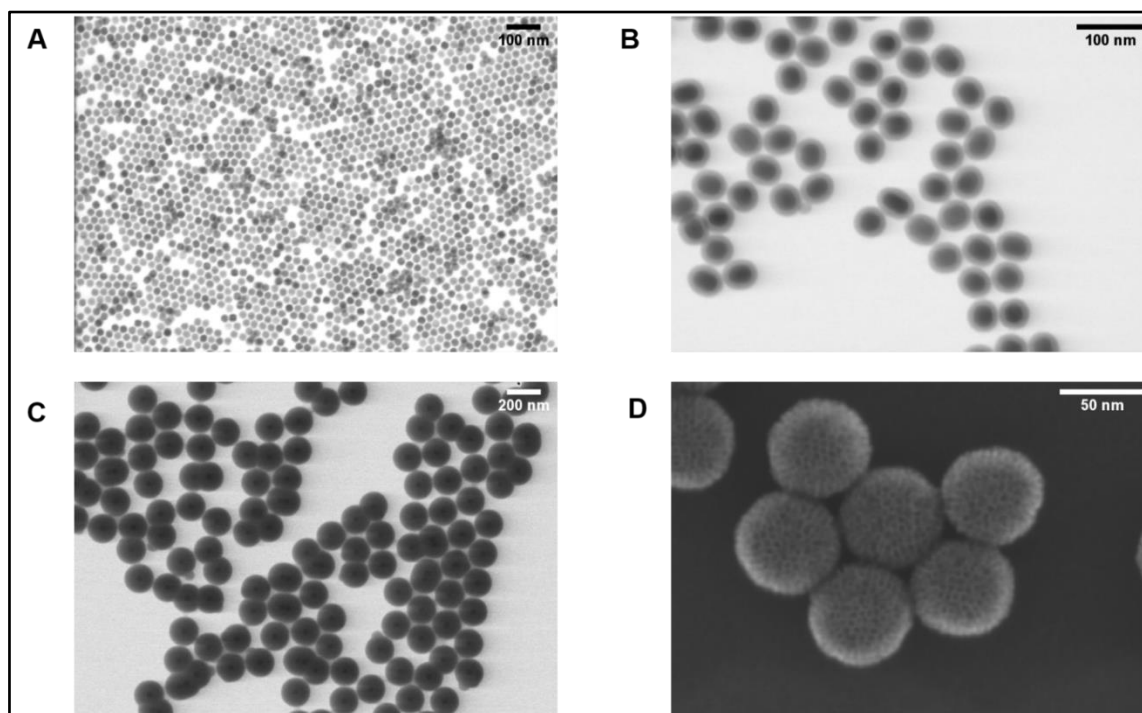


Figure S1: TSEM images of **A)** Oleate coated $\text{NaYF}_4: 20\% \text{Yb}^{3+}, 2\% \text{Er}^{3+}$ (UCNP) redispersed in cyclohexane, average diameter: 20 nm. **B)** UCNP coated with a thin silica shell of average shell thickness of 10 nm. **C)** UCNP coated with a thick silica shell of average shell thickness of 73 nm. **D)** UCNP coated with a mesoporous silica shell of average shell thickness of 23 nm.

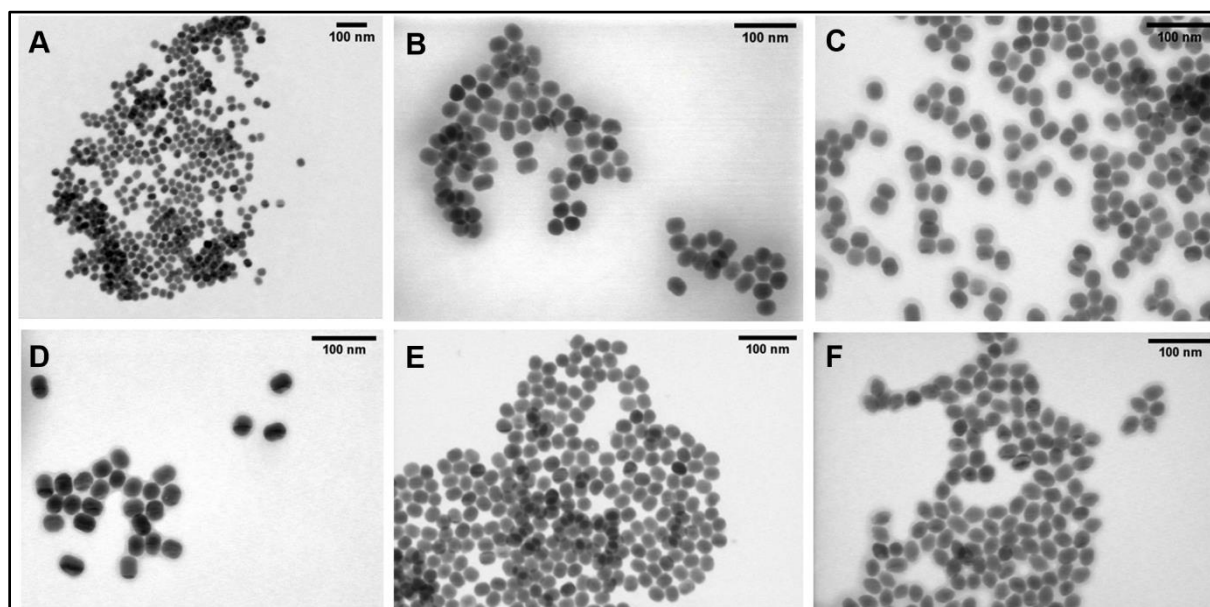


Figure S2: TSEM images of UCNP after surface modification. UCNP coated with polyacrylic acid and redispersed in water, average diameter of UCNP: 20 nm **(A)** and 30 nm **(B)**. Bare UCNP after treatment with NOBF_4 and redispersion in DMF, average diameter of UCNP: 20 nm **(C)** and 30 nm **(D)**. UCNP coated with citrate and redispersed in water, average diameter of UCNP: 20 nm **(E)** and 30 nm **(F)**.

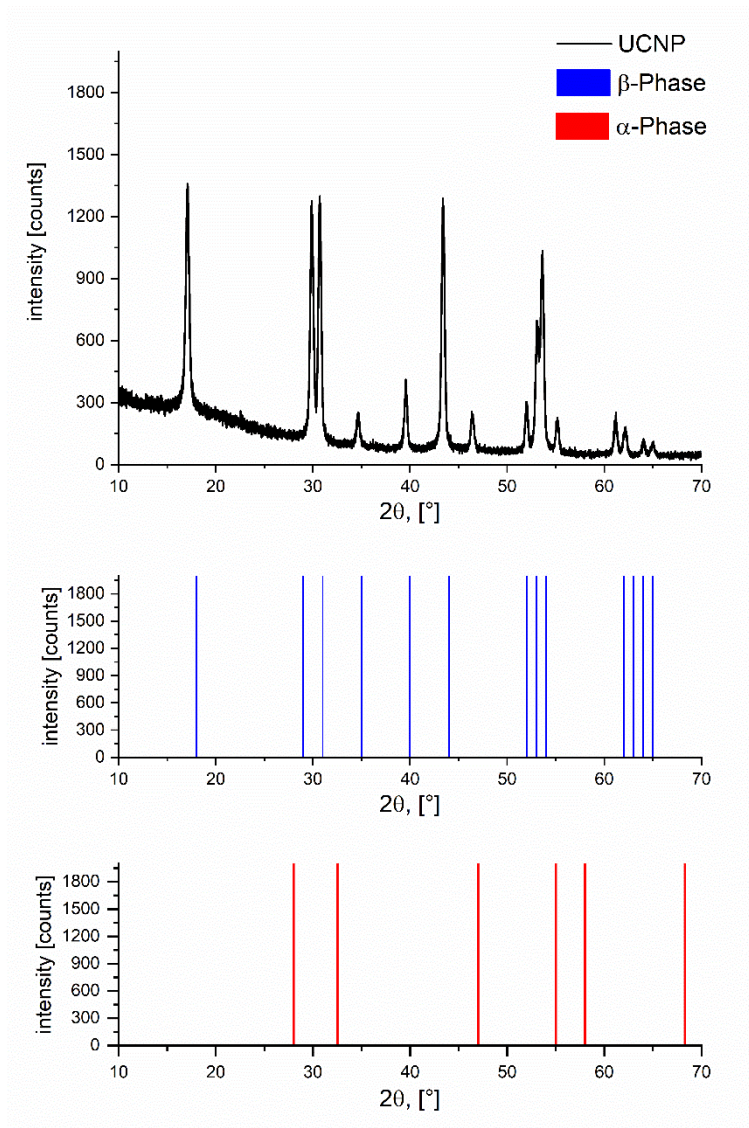
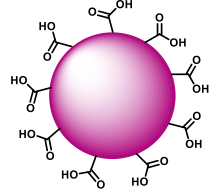
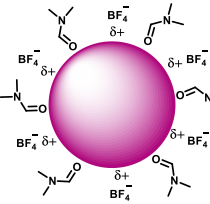
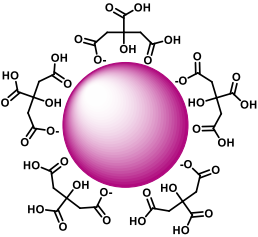


Figure 3: XRD diffractogram of the oleate stabilized upconversion nanoparticles, black spectrum. The blue bars refer to the reference values of the hexagonal β -phase crystal structure (JCPDS No. 28-1192), and the red bars refer to the reference values of the cubic α -phase crystal structure (JCPDS No. 77-2042) crystal structure of undoped NaYF_4 .

Table S3: Average surface zeta potential of the upconversion nanoparticles of the different surface functionalizations

Sample ID	Zeta potential (mV)	Pdl	Schematic representation
UC-PAA-20	-22.1 ± 0.9	0.36 ± 0.01	
UC-PAA-30	-20.0 ± 0.46	0.24 ± 0.04	
UC-bare-20	32.8 ± 0.11	0.34 ± 0.01	
UC-bare-30	35.8 ± 0.55	0.40 ± 0.02	
UC-citrate-20	-18.9 ± 1.96	0.33 ± 0.04	
UC-citrate-30	-14.5 ± 2.03	0.79 ± 0.18	

The sensitizer, Yb^{3+} has a maximum absorption peak at 976 nm (Figure S3, A). Upon 976 nm excitation, $\text{NaYF}_4: 20\% \text{Yb}^{3+}, 2\% \text{Er}^{3+}$ has three main emission peaks, two peaks in the green region of the visible spectrum (525 and 541 nm) and one peak in the red region (655 nm; Figure S3, B).

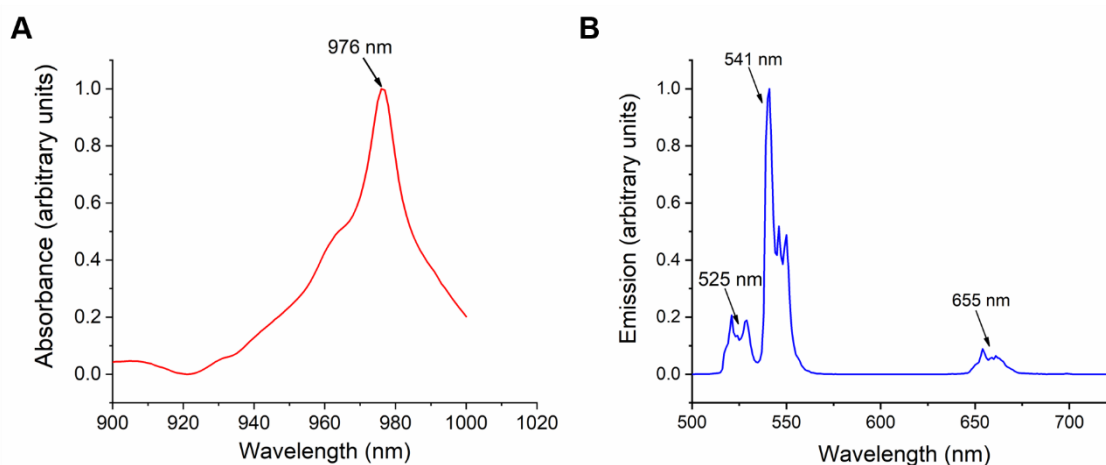


Figure S4: **A)** Absorbance of the upconversion nanoparticles showing an absorption maximum at 976 nm. **B)** UCL spectrum of the UCNP upon excitation at 976 nm revealing the green and red Er^{3+} emission bands.

5. Analytical Measurements for the Detection of the Released Ions

Table S4: Percentages of lanthanide ions released upon dissolution of UCNP in water. The concentration of the starting UCNP dispersion was 50 $\mu\text{g/L}$ in water

Sample ID	% Y^{3+}	% Yb^{3+}	% Er^{3+}
UC-PAA-20	75.77	21.58	2.65
UC-PAA-30	75.60	21.58	2.82
UC-bare-20	75.25	21.58	3.17
UC-bare-30	79.51	17.36	3.12
UC-citrate-20	77.51	19.35	3.13
UC-citrate-30	75.36	21.64	2.99

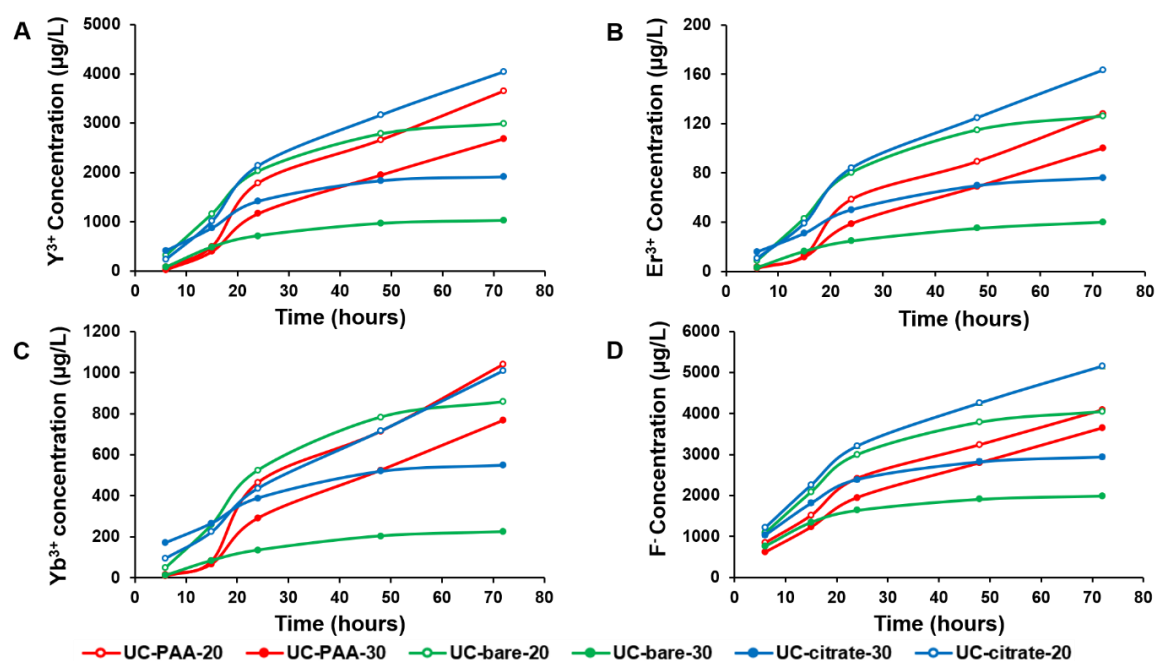


Figure S5: Concentrations of the ions released from upconversion nanoparticles of different particle sizes and surface functionalizations in water at room temperature. The starting concentration of the nanoparticles was 50 mg/L . Lanthanide ion concentrations were obtained from ICP/OES measurements of the supernatants after aging studies, while the fluoride ion concentrations were analyzed using a fluoride ion selective electrode. The solid lines are a guide to the eye.

Table S5: Results of the ISE measurements revealing the amount of fluoride ions released from the differently sized UCNP of varying surface chemistries upon aging in water for 72 hours. Two concentrations of UCNP in water were used, 5 and 50 mg/L.

Sample name	released F ⁻ conc. [ppb]	Start conc.	X _F [mol%]
UC-PAA-20	1399	5 ppm	76.67
	4090	50 ppm	22.42
UC-PAA-30	1067	5 ppm	58.48
	3650	50 ppm	20.00
UC-bare-20	1576	5 ppm	86.37
	4050	50 ppm	22.20
UC-bare-30	1139	5 ppm	62.42
	1990	50 ppm	10.90
UC-citrate-20	1251	5 ppm	68.56
	5160	50 ppm	28.28
UC-citrate-30	1252	5 ppm	68.61
	2940	50 ppm	16.11

Table S6: Concentration and mole fraction of fluoride ions released upon aging of UCNP in water for 72 hours. The concentration of the starting UCNP dispersions were always 50 mg/L.

Sample ID	F ⁻ (μg/L)	T	X _F (mol%)
UC-bare-20	4050	RT	22.20
	6640	37°C	36.39
UC-citrate-20	7210	RT	39.51
	7780	37°C	42.64
UC-SiO ₂ -thick	200	RT	1.096
	102	37°C	0.559
UC-SiO ₂ -thin	1830	RT	10.03
	4281	37°C	23.46
UC-mSiO ₂ -NH ₃	2150	RT	11.78
	2694	37°C	14.76
UC-mSiO ₂ -NaOH	2990	RT	16.39
	3966	37°C	21.74

Table S7: Mole fraction of fluoride ions released upon UCNP aging in different aqueous environments. Starting concentration of UCNP: 50 mg/mL.

Sample ID	T	Aqueous medium	X _F [mol%]
UCNP-bare-20	RT	PBS	46.39
	RT	H ₂ O	22.20
	37 °C	DMEM	4.165
UCNP-citrate-20	RT	PBS	49.08
	RT	H ₂ O	39.51
	37 °C	DMEM	4.05
UCNP-SiO ₂ -thin	RT	PBS	19.03
	RT	H ₂ O	10.03
	37 °C	DMEM	1.261
UCNP-mSiO ₂ -NH ₃	RT	PBS	17.45
	RT	H ₂ O	11.78
	37 °C	DMEM	1.096
UCNP-mSiO ₂ -NaOH	RT	PBS	21.66
	RT	H ₂ O	16.39
	37 °C	DMEM	1.315
UCNP-SiO ₂ -thick	RT	PBS	2.263
	RT	H ₂ O	1.096
	37 °C	DMEM	2.192

6. Luminescence Lifetime Measurements

Table S8: Yb³⁺ and Er³⁺ and luminescence lifetimes of UCNP-citrate-20 and UCNP-SiO₂-thin samples. Both samples were aged in water for different time intervals. The UCNP were then collected and redispersed in water for the lifetime measurements. Lifetime measurements were carried out in MilliQ water with a spectrofluorometer (Edinburgh Instruments, FLS-980) equipped with an electrically pulsed, 8 W 976 nm laser diode. The lifetimes of the Yb³⁺ and Er³⁺ emission bands were obtained from the decay profiles recorded at 1010 nm and 545 nm using tail fitting with a biexponential decay function.

Sample name	Aging time [hours]	Lifetime Er UC [μ s]	Lifetime Yb DC [μ s]
UCNP-citrate-20	0 h	66	47
UCNP-citrate-20	6 h	62	47
UCNP-citrate-20	24 h	63	41
UCNP-citrate-20	48 h	60	33
UCNP-SiO ₂ -thin	0 h	94	87
UCNP-SiO ₂ -thin	6 h	73	66
UCNP-SiO ₂ -thin	24 h	71	60
UCNP-SiO ₂ -thin	48 h	72	57

Table S9: Er³⁺ and Yb³⁺ luminescence lifetimes of sample UCNP-bare-20 aged in DMEM for different time intervals. The nanoparticles were collected and redispersed in water for measurements. Lifetime measurements were carried out with a spectrofluorometer (Edinburgh Instruments, FLS-980) equipped with an electrically pulsed, 8 W, 976 nm laser diode. The lifetimes of the Yb³⁺ and Er³⁺ emission bands were obtained from the decay profiles recorded at 1010 nm and 545 nm using tail fitting with a biexponential decay function.

Sample name	Aging time [hours]	Solvent	Lifetime Er UC [μ s]	Lifetime Yb DC [μ s]
UCNP-bare-20	0 h	H ₂ O	87	65
UCNP-bare-20	0 h	DMEM	87	77
UCNP-bare-20	12 h	DMEM	86	81
UCNP-bare-20	24 h	DMEM	85	81
UCNP-bare-20	48 h	DMEM	85	85

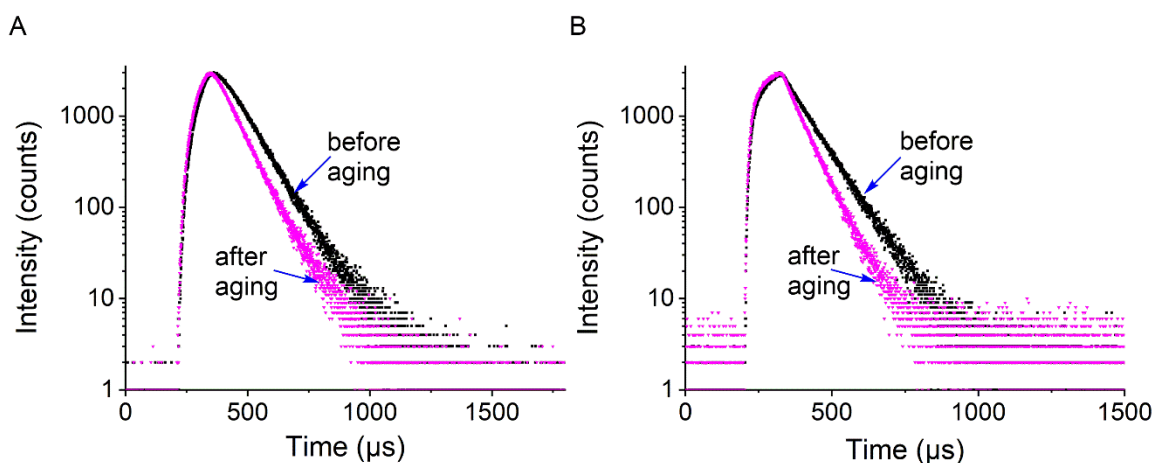


Figure S6: A) Er^{3+} and **B)** Yb^{3+} luminescence decay curves of unaged (magenta) and aged (black) UCNP- SiO_2 -thin sample. UCNPs were aged for 72 hours in water, then collected by centrifugation, and redispersed in MilliQ water for the measurements. Excitation wavelength: 976 nm. Yb^{3+} and Er^{3+} decays were detected at 1010 nm and 545 nm.

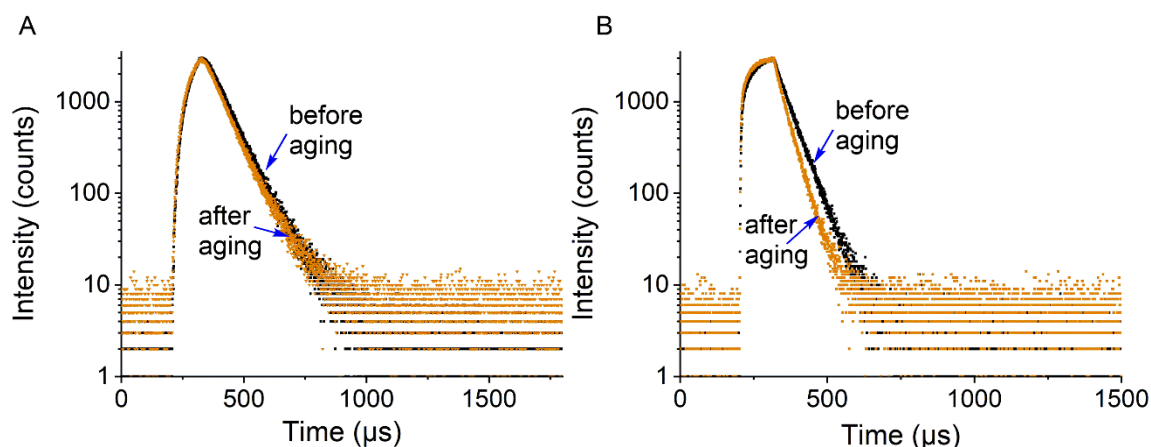


Figure S7: A) Er^{3+} and **B)** Yb^{3+} luminescence decay curves of aged (black curves) and unaged (orange curves) sample UCNPs-citrate-20. Nanoparticles were aged for 72 hours in water, collected after aging, and redispersed in water for the measurements. Excitation wavelength: 976 nm, Yb^{3+} and Er^{3+} decays were detected at 1010 nm and 545 nm.

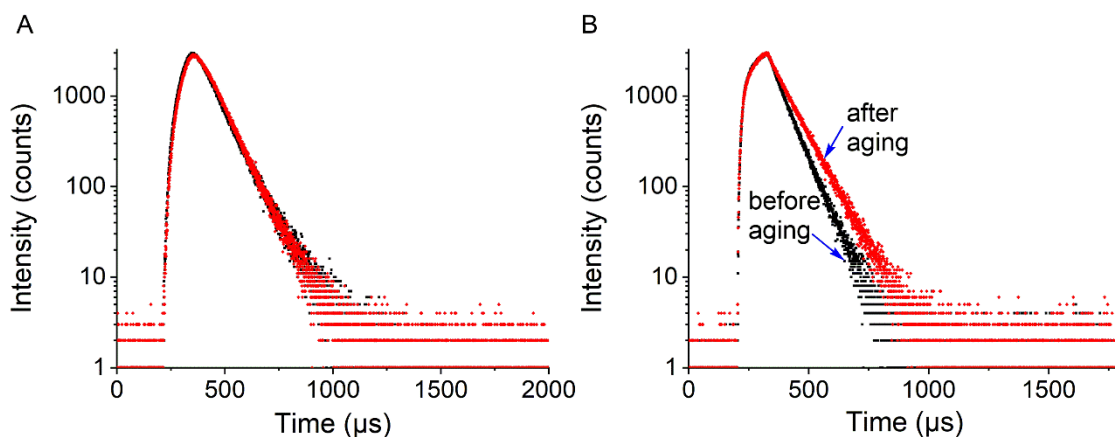


Figure S8: A) Er³⁺ and **B)** Yb³⁺ luminescence lifetime curves of aged (black curves) and unaged (orange curves) sample UCNP-citrate-20. Nanoparticles were aged for 72 hours in DMEM, collected after aging, and redispersed in water for the measurements. Excitation wavelength: 976 nm, Yb³⁺ and Er³⁺ decays were detected at 1010 nm and 545 nm.

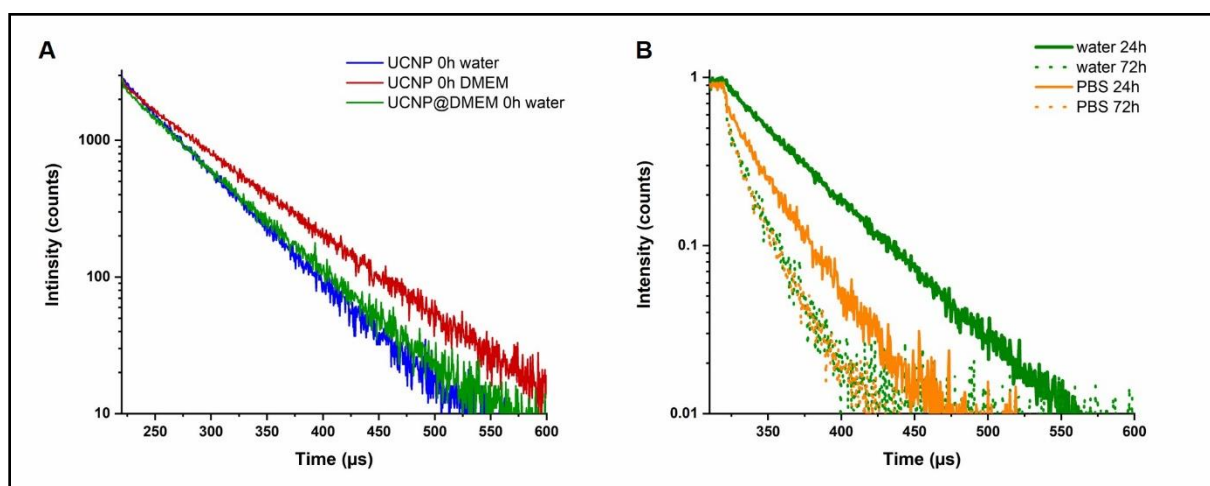


Figure S9: A) Normalized decay curves of the DC emission of Yb³⁺ of UCNP in water (blue), UCNP after immediate transfer to DMEM (UCNP@DMEM, red), and UCNP@DMEM after immediate transfer to water (green curve). **B)** Normalized decay curves of the Yb³⁺ DC emission of UCNP@DMEM aged in water for 24 hours (green line) and 72 hours (green dotted line) and in PBS for 24 hours (orange line) and 72 hours (orange dotted line). Excitation wavelength: 976 nm, Yb³⁺ and Er³⁺ decays were detected at 1010 nm and 545 nm.

7. X-ray Photoelectron Spectroscopic Measurements Results

Table 10: XPS results of unaged UC-bare-20 showing the elemental composition of the surface of the UCNP and the types of chemical bonding as suggested by the binding energies

Peak name	E _B /eV	Area/cps.eV	Sens. Fact.	Norm. Area	Quant./at.%	
Y 3d	159	313473.3	106180	2.952271	17	
C1s	285	29942.26	18783	1.594038	9.18	
O1s	524	15905	57121	0.2784399	1.6	
F1s	684	783160	81590	9.598722	55.27	
Na 1s	1071	250385.9	85092	2.942518	16.94	
Peak name	Peak hight/ Counts	Lorentzian	Position/eV	FWHM/eV	Abs. Area/ Counts eV	Rel. Area/ %
C-C, C-H	8229.1	0.1	284.921	1.4	12712	78.31
C-OR	1393.5	0.1	286.3808	1.4	2153	13.26
C=O	831.842	0.1	288.5549	1.4	1282	7.89
O-C=O	57.215	0.1	289.6822	1.4	87.72	0.54

Table 11: XPS results of UC-bare-20 after incubation in DMEM showing the elemental composition of the surface of the UCNP and the types of chemical bonding as suggested by the binding energies

Peak name	E _B /eV	Area/cps.eV	Sens. Fact.	Norm. Area	Quant./at.%	
Si 2p	99	66576.48	14080	4.728426	33.88	
C2p	200	17209.21	41363	0.4160509	2.98	
C1s	285	71412.04	18760	3.802558	27.25	
Ca1s	348	10017.33	972277	0.1029765	0.74	
N 1s	401	10884.16	34960	0.3113233	2.23	
O 1s	532	230073.1	57091	4.0299	28.88	
Na 1s	1072	48052.79	85062	0.5649132	4.05	
Peak name	Peak hight/ Counts	Lorentzian	Position/eV	FWHM/eV	Abs. Area/ Counts eV	Rel. Area/ %
C-C, C-H	13032.8	0.1	284.8346	1.4	20176	51.02
C-OR	6644.5	0.1	286.3934	1.4	10298	26.04
C=O	2271.6	0.1	288.2208	1.4	3523	8.91
O-C=O	1604.4	0.1	289.8536	1.4	2488	6.29
K 2p3	1345.4	0.1	293.2611	1.4	2083	5.27
K 2p1	633.882	0.1	295.9938	1.4	976.26	2.47
Peak name	Peak hight/ Counts	Lorentzian	Position/eV	FWHM/eV	Abs. Area/ Counts eV	Rel. Area/ %
-NR2	2091.6	0.2	399.4478	1.7	4061	73.65
-N-C=O	748.075	0.2	401.1823	1.7	1453	26.35

8. References

- 1 Li, Z., Zhang, Y. & Jiang, S. Multicolor Core/Shell-Structured Upconversion Fluorescent Nanoparticles. *Advanced Materials* **20**, 4765-4769, doi:10.1002/adma.200801056 (2008).
- 2 Wang, F., Banerjee, D., Liu, Y., Chen, X. & Liu, X. Upconversion nanoparticles in biological labeling, imaging, and therapy. *Analyst* **135**, 1839-1854, doi:10.1039/c0an00144a (2010).
- 3 Wang, F. *et al.* Simultaneous phase and size control of upconversion nanocrystals through lanthanide doping. *Nature* **463**, 1061-1065, doi:10.1038/nature08777 (2010).
- 4 Radunz, S. *et al.* Evolution of Size and Optical Properties of Upconverting Nanoparticles during High-Temperature Synthesis. *The Journal of Physical Chemistry C* **122**, 28958-28967, doi:10.1021/acs.jpcc.8b09819 (2018).
- 5 Wilhelm, S. *et al.* Water dispersible upconverting nanoparticles: effects of surface modification on their luminescence and colloidal stability. *Nanoscale* **7**, 1403-1410, doi:10.1039/c4nr05954a (2015).
- 6 Li, C., Liu, J., Alonso, S., Li, F. & Zhang, Y. Upconversion nanoparticles for sensitive and in-depth detection of Cu²⁺ ions. *Nanoscale* **4**, 6065-6071, doi:10.1039/c2nr31570j (2012).
- 7 Kembuan, C., Saleh, M., Rühle, B., Resch-Genger, U. & Graf, C. Coating of upconversion nanoparticles with silica nanoshells of 5–250 nm thickness. *Beilstein Journal of Nanotechnology* **10**, 2410–2421, doi:doi:10.3762/bjnano.10.231 (2019).
- 8 Stöber, W., Fink, A. & Bohn, E. Controlled growth of monodisperse silica spheres in the micron size range. *Journal of Colloid and Interface Science* **26**, 62–69, doi:10.1016/0021-9797(68)90272-5 (1968).
- 9 Nozawa, K. *et al.* Smart control of monodisperse Stöber silica particles: effect of reactant addition rate on growth process. *Langmuir : the ACS journal of surfaces and colloids* **21**, 1516–1523, doi:10.1021/la048569r (2005).
- 10 Dong, A. *et al.* A generalized ligand-exchange strategy enabling sequential surface functionalization of colloidal nanocrystals. *J Am Chem Soc* **133**, 998-1006, doi:10.1021/ja108948z (2011).
- 11 Carron, S. *et al.* Assembly of near infra-red emitting upconverting nanoparticles and multiple Gd(III)-chelates as a potential bimodal contrast agent for MRI and optical imaging. *Dalton Trans* **44**, 11331-11339, doi:10.1039/c5dt00919g (2015).
- 12 Juan, J., Cheng, L., Shi, M., Liu, Z. & Mao, X. Poly-(allylamine hydrochloride)-coated but not poly(acrylic acid)-coated upconversion nanoparticles induce autophagy and apoptosis in human blood cancer cells. *Journal of Materials Chemistry B* **3**, 5769-5776, doi:10.1039/c5tb00646e (2015).

7. Publications: Minor Contributions

7.1 Coating of upconversion nanoparticles with silica nanoshells of 5-250 nm thickness

Title	Coating of upconversion nanoparticles with silica nanoshells of 5-250 nm thickness
Authors	Cynthia Kembuan, Maysoon Saleh , Bastian Rühle, Ute Resch-Genger and Christina Graf
Journal	Beilstein Journal of Nanotechnology
DOI	https://doi.org/10.3762/bjnano.10.231
Links	https://www.beilstein-journals.org/bjnano/articles/10/231
Detailed scientific contribution	The concept of this manuscript was elaborated by C. Kembuan, M. Saleh and C. Graf. Experiments were designed, planed and carried out by C. Kembuan and M. Saleh. All co-authors participated in the interpretation and evaluation of the results. The manuscript was mainly written by C. Kembuan and C. Graf, then revised and discussed with M. Saleh, B. Rühle and U. Resch-Genger.
Estimated own contribution	~ 30 %
Date of publication	09. December. 2019



Coating of upconversion nanoparticles with silica nanoshells of 5–250 nm thickness

Cynthia Kembuan¹, Maysoon Saleh^{1,2}, Bastian Rühle², Ute Resch-Genger² and Christina Graf^{*3}

Full Research Paper

Open Access

Address:

¹Institut für Chemie und Biochemie, Physikalische und Theoretische Chemie, Freie Universität Berlin, Takustraße 3, D-14195 Berlin, Germany, ²Bundesanstalt für Materialforschung und -prüfung (BAM), Richard-Willstätter-Str. 11, D-12489 Berlin, Germany and ³Hochschule Darmstadt - University of Applied Sciences, Fachbereich Chemie- und Biotechnologie, Stephanstr. 7, D-64295 Darmstadt, Germany

Email:

Christina Graf^{*} - christina.graf@h-da.de

* Corresponding author

Keywords:

reverse microemulsion; silica coating; stepwise growth; thick shells; upconversion nanoparticles

Beilstein J. Nanotechnol. **2019**, *10*, 2410–2421.

doi:10.3762/bjnano.10.231

Received: 07 July 2019

Accepted: 19 November 2019

Published: 09 December 2019

Associate Editor: S. Giordani

© 2019 Kembuan et al.; licensee Beilstein-Institut.

License and terms: see end of document.

Abstract

A concept for the growth of silica shells with a thickness of 5–250 nm onto oleate-coated NaYF₄:Yb³⁺/Er³⁺ upconversion nanoparticles (UCNP) is presented. The concept enables the precise adjustment of shell thicknesses for the preparation of thick-shelled nanoparticles for applications in plasmonics and sensing. First, an initial 5–11 nm thick shell is grown onto the UCNPs in a reverse microemulsion. This is followed by a stepwise growth of these particles without a purification step, where in each step equal volumes of tetraethyl orthosilicate and ammonia water are added, while the volumes of cyclohexane and the surfactant Igepal[®] CO-520 are increased so that the ammonia water and surfactant concentrations remain constant. Hence, the number of micelles stays constant, and their size is increased to accommodate the growing core-shell particles. Consequently, the formation of core-free silica particles is suppressed. When the negative zeta potential of the particles, which continuously decreased during the stepwise growth, falls below –40 mV, the particles can be dispersed in an ammoniacal ethanol solution and grown further by the continuous addition of tetraethyl orthosilicate to a diameter larger than 500 nm. Due to the high colloidal stability, a coalescence of the particles can be suppressed, and single-core particles are obtained. This strategy can be easily transferred to other nanomaterials for the design of plasmonic nanoconstructs and sensor systems.

Introduction

Lanthanide-based nanocrystals have gained importance as inorganic optical reporters in recent years [1-3]. The doping of inorganic host NaYF_4 matrices with different optically active lanthanide ions can result in so-called upconversion nanoparticles (UCNP) which can absorb photons of lower energy (e.g., near-infrared (NIR) light) and emit photons of higher energy (e.g., visible light) via a two- or multiphoton upconversion mechanism involving several energy transfer steps [2-5]. Advantages of UCNPs compared to organic dyes or other inorganic nanoscale reporters are the emission of a multitude of characteristic narrow emission bands in the ultraviolet/visible/NIR upon excitation in the NIR range where light absorption and scattering from biological tissues is minimal as well as long fluorescence lifetimes in the microsecond range that are insensitive to oxygen, a high chemical stability and a low cytotoxicity [6,7]. This makes UCNPs attractive for applications in the life sciences [8-11]. Some of the most frequently used UCNPs are NaYF_4 -based nanoparticles (NPs) with Yb^{3+} as the light absorbing sensitizer and Er^{3+} as the emitting activator [12-15]. Monodisperse UCNPs with relatively high quantum yields are typically prepared in organic solvents at high temperatures using hydrophobic capping agents such as oleic acid [16,17]. Life sciences applications of these NPs require to render them water-dispersible using either ligand exchange or encapsulation procedures [2,13,18,19]. This can be similarly necessary for applications in plasmonics or chemical sensing [20,21].

One of the most versatile ways to protect the surface of NP, making hydrophobic particle surfaces hydrophilic and simultaneously providing functional groups for subsequent covalent attachment of, e.g., biomolecules, is the coating of their surface with silica shells [22,23]. Additionally, optically transparent silica shells have many other advantages such as chemical inertness, high thermal stability, low cytotoxicity, high biocompatibility and tunable porosity [22-24]. An important parameter for all shelling procedures is the precise control of the shell thickness while preventing or at least minimizing the formation of additional seeds from the shelling material. Numerous approaches have been investigated for the growth of silica shells on inorganic NPs like the Stöber synthesis and the reverse microemulsion method. The Stöber method refers to the process of preparing silica via the hydrolysis and condensation of tetraethyl orthosilicate (TEOS) within an alcohol–ammonia–water system [25]. Related methods are widely used for coating NPs that are dispersible in polar media [26,27]. Modified Stöber processes, in which TEOS is continuously added to seeds in a growth solution, allow for the growth of large, monodisperse NPs in a single step, provided the seed NPs are well dispersed in the growth solution [28,29]. A versatile approach for growing silica shells onto inorganic NPs that cannot

be dispersed in polar media is the reverse microemulsion technique [22,23,30-43]. In a reverse microemulsion, the aqueous solution is confined in uniform, nanosized droplets that are stabilized by a surfactant such as a polyoxyethylene (5) nonylphenylether (trade name Igepal® CO-520) and distributed in the continuous nonpolar phase [44]. The ratio between the aqueous components and the surfactant determines the size of these droplets [30], which act as nanoreactors. For the polycondensation of precursors such as TEOS, ammonia usually acts as a catalyst [43]. This technique allows for the formation of uniform silica shells on individual particle cores [23,40,41].

Up to now, syntheses of UCNPs with relatively thin silica shells (mostly 1–10 nm) have mostly been reported. Li et al. presented the first approach to coat oleate-stabilized UCNPs via the reverse microemulsion technique in 2008 [42,43]. However, for certain applications such as sensing and plasmonics, a thicker silica shell is desired that can be loaded with sensor molecules or used as spacer for the plasmonic enhancement of the emission of UCNPs by gold or silver shells [45]. Moreover, since UCNPs can release rare earth metal and fluoride ions to some extent into the surrounding medium [46], which can cause toxic effects, a thick silica shell could act as protective coating [46].

For silica shells grown onto iron oxide NPs using an inverse microemulsion, it was shown that the thickness of the shell increases as the amount of TEOS increases, while core-free silica NPs appear when the TEOS content exceeds the threshold of homogeneous nucleation [36,39,47-49]. Typically, a maximum diameter <50 nm can be reached with this technique [23]. Microemulsion growth processes are usually slow and laborious as one has to control the water-to-surfactant ratio to prevent the formation of core-free silica NPs. In this respect, combining this technique with Stöber growth can be advantageous [50]. For example, Katagiri managed to further grow silica-coated Fe_3O_4 particles with a thin shell to a diameter >100 nm by a similar procedure [23].

In this work, we present an approach for growing a silica shell with an adjustable thickness between 5 and 250 nm onto oleate-coated $\text{NaYF}_4:\text{Yb}^{3+}/\text{Er}^{3+}$ UCNP. This coating procedure comprises the growth of a silica shell via a reverse microemulsion method to shell thicknesses of about 40–50 nm, followed by the growth of a thick silica layer by continuously adding TEOS in a Stöber-like growth step. Thereby, particle aggregation, which can occur during a Stöber-like growth process, and the formation of NPs from the shell material can be elegantly prevented, and monodisperse particles with just one UCNP core in the center coated by a thick silica shell are obtained. This method should also be suitable for other NPs with hydrophobic

surfaces dispersed in an apolar solvent independent of their chemical composition.

Results and Discussion

The core particles used in this study, i.e., oleate-capped UCNPs with a NaYF_4 host structure and doped with 18% Yb and 2% Er, were synthesized by a thermal decomposition method [16] yielding spherical particles of low polydispersity. A typical scanning transmission electron microscopy (STEM) image is shown in Figure 1A. The diameter of the UCNP@SiO_2 core-shell particles was obtained from these STEM images, and the corresponding hydrodynamic diameters were measured by dynamic light scattering (DLS, see below in Table 1). Although large, core-free silica particles can easily be obtained by Stöber-like growth processes [28], and the controlled growth of silica particles to large monodisperse particles with a precisely predetermined diameter is well-established, a direct Stöber

growth of silica shells on hydrophobic particles in a nonpolar solvent is not feasible. Aiming at the development of a synthesis providing maximum growth of a silica layer in a single step without producing UCNP-free silica particles as side products, a thin silica layer was grown first onto the particles via a reverse microemulsion process in cyclohexane with Igepal CO-520 as surfactant and ammonia as a catalyst. In such a reverse microemulsion, the size and the number of the aqueous domains, i.e., the water pools inside the micelles, are determined by the ratio of ammonia water to Igepal CO-520, often denoted as the R-value [30,36,51,52]. Several authors suggested that for an optimal growth process where particles with multiple cores as well as coreless particles are absent, the number of micelles has to ideally match the number of particles [36,47]. If in the course of this process the silica shell becomes thicker, ammonia water and surfactant must be added accordingly in order to balance the particle growth, while suppressing the formation of new

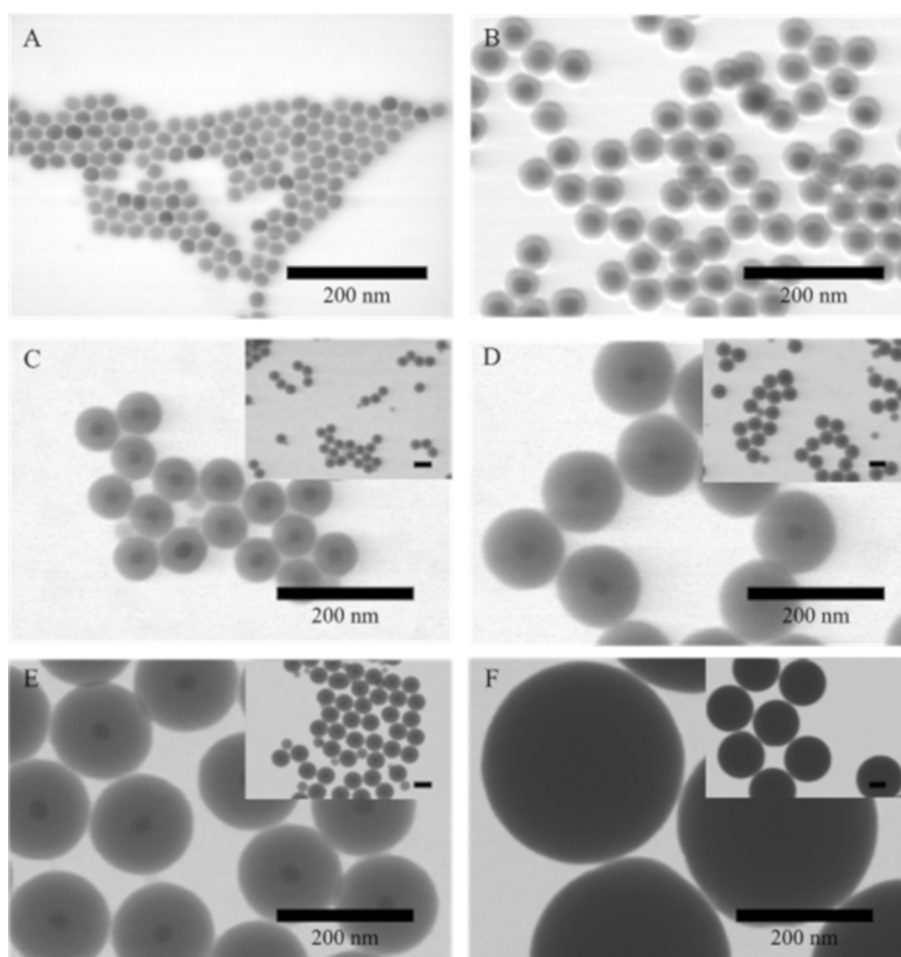


Figure 1: TEM images of (A) $\text{NaYF}_4:(\text{Yb},\text{Er})$ cores (C1; diameter: 24 ± 1 nm) and (B) the same core after coating with the first thin silica shell (C1_1S, shell thickness: 7 ± 1 nm). Image (C) shows the same UCNP cores after the second silica coating step (C1_2S, shell thickness: 18 ± 2 nm), (D) after the third silica coating (C1_3S, shell thickness: 35 ± 2 nm), (E) after the fourth shell silica coating (C1_4S, shell thickness: 44 ± 2 nm) and (F) after the fifth silica growth step (C1_5S, shell thickness: 149 ± 8 nm). The first to the fourth silica shell were grown with the reverse microemulsion method, whereas the fifth shell was grown using a modified Stöber growth. The scale bar in the insets of panels (C–F) represents 100 nm.

micelles [23]. Ding et al. linked these considerations to the theory of LaMer [36]. According to the LaMer theory, heterogeneous nucleation occurs when the supersaturation of the growth species is below the homogeneous nucleation threshold but above the heterogeneous nucleation threshold, while a higher supersaturation (above the homogeneous nucleation threshold) leads to simultaneous heterogeneous and homogeneous nucleation. In general, the processes leading to homogeneous and heterogeneous nucleation and growth in such reverse microemulsion systems are complex and depend on numerous factors. Our considerations for the growth of thick silica shells on UCNPs are based on the models presented by Ding et al. [36] and Katagiri et al. [23] for silica-coated iron oxide NP.

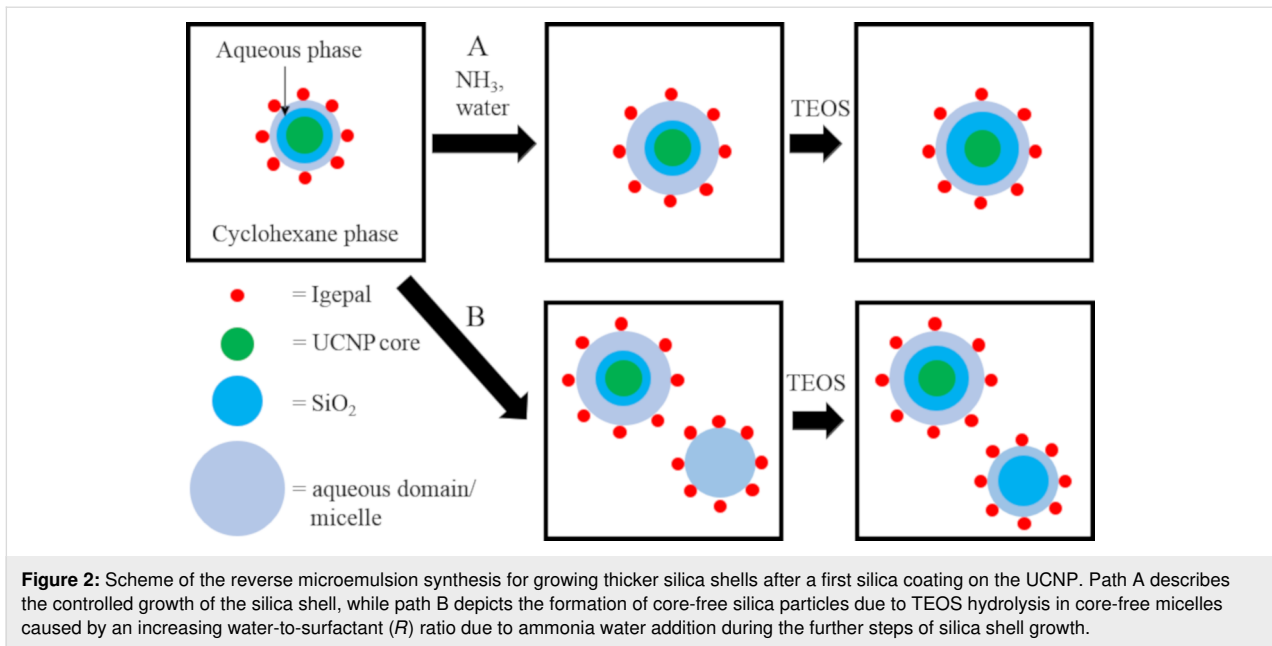
For UCNPs with a diameter of 24 ± 2 nm and a particle concentration of 3 g/L, with an ammonia water-to-surfactant weight ratio of 1:9.5 or a molar ratio of 1:2.7 and an ammonia water concentration of 1.7 ± 0.5 wt % in cyclohexane almost no core-free particles (<1%) are formed. For the desired control of the growth process and hence shell thickness, a relatively low ammonia water-to-surfactant ratio was used as this slows down the hydrolysis of TEOS and thus shell growth. A general scheme of the growth of the initial silica layer on the UCNPs with this reverse microemulsion process is shown in Figure S1 in Supporting Information File 1. According to the mechanism of silica growth reported for oleate-functionalized iron oxide NP, the oleate ligands on the NP surface are at least partly exchanged for the surfactant as well as the hydrolyzed TEOS upon addition of the oleate-functionalized NPs to the Igepal CO-520–cyclohexane system [36,47]. A similar process is assumed for the oleate-capped UCNPs. As the size of our UCNPs was 2–3 times larger than the size of the iron oxide NPs [23,36], and their number concentration was 8 and 1.6 times higher than the ones used in [36] and [23], respectively, we used a higher concentration of Igepal CO-520. In our case, even with a significantly lower ratio of surfactant to particle surface (1.6 mol/m^2 in the present case, 9.5 mol/m^2 and 5.2 mol/m^2 in the cases of Ding et al. [36] and Katagiri et al. [23], respectively) no silica particles with multiple UCNP cores were formed. Based on these considerations, we also used a lower value of the ammonia water-to-surfactant (*R*) weight ratio for the first silica shell growth steps (1:9.4 in the present case; compared to 1:2.7 in the work of Ding et al. [36] and 1:6.1 in the work of Katagiri et al. [23]).

For further shell growth, even a slightly lower Igepal CO-520 concentration in cyclohexane (from 16 wt % for the first to 14 wt % for the subsequent shell growth steps) and an increased ammonia water concentration (from 1.7 wt % for the first and 3.3 wt % for the subsequent shell growth steps) were employed, raising the *R*-value from 1:9.5 to 1:4.3. In this way,

the number of micelles was kept constant, and their diameters were adjusted so that they are large enough to host the growing core–shell particles.

After an initial silica shell of 5–10 nm was coated onto the UCNP, a further growth by a Stöber-like growth process was attempted, i.e., the particles were redispersed in ethanol, and ammonia water, water and TEOS were added. However, these attempts resulted in samples where most of the particles are grown together as well as in the formation of core-free silica particles. Figure S2 in Supporting Information File 1 shows UCNPs with a diameter of 20 ± 2 nm (sample C2_1S) initially coated with an 11 ± 1 nm silica shell followed by the Stöber-like regrowth. Similar findings were also obtained for larger UCNP. It turned out in several preliminary experiments conducted by the same procedure that the zeta potential of the particles after the initial silica growth in the reverse microemulsion was always only around -20 mV, which explains the low colloidal stability of these particles. The latter was also confirmed by the rather high hydrodynamic diameter of the particles derived from DLS compared to the diameter obtained by STEM (see below in Table 1). A similarly low colloidal stability of the NPs coated with silica in reverse microemulsions was reported before [53–56] and attributed to the presence of the Igepal CO-520 on the NP surface. However, extensive purification of the particles after the growth of the first silica shell by repeated centrifugation and redispersion in ethanol did not significantly alter their zeta potential.

For this reason, further silica shell growth was performed in a reverse microemulsion. For this procedure, initially, the concept for growing larger silica shells on oleate-coated iron oxide NPs introduced by Ding et al. was adapted for the UCNPs [36] and used for a step-wise growth process (Figure 2). According to this model, the controlled addition of ammonia water along with increasing the amount of surfactant corresponding to the size of the (silica-coated) core should lead to slow hydrolysis of TEOS and consequently a well-controlled growth of the silica shell yielding a thin silica shell (Figure 2, path A) [30]. In contrast, if the ammonia water concentration is quickly raised from a low *R*-value, the volume of the water domain in the micelles increases. This causes an increase in the hydrolysis rate and the formation of new empty micelles and promotes the formation of new silica particles and uncontrolled silica growth (see Figure 2 path B) [36]. In the STEM image in Figure S3 in Supporting Information File 1, a sample is shown where the *R*-value was only 1:2.2, and consequently, many core-free silica particles were formed. Hence, for the further shell growth, especially for a silica shell thickness exceeding 10 nm, the *R*-value was adjusted to 1:4.3 to keep the aqueous domain large enough for the growth of thicker silica shells but small enough to



suppress the formation of core-free silica particles. In the following, the amount of each chemical for the further steps of the silica shell growth is discussed. For a second silica shell with the thickness t_2 , the volume of TEOS (V_T) was calculated for a given mass m_{UCNP} of uncoated UCNP cores with diameter d_U according to Equation 1 assuming 100% conversion of TEOS to SiO_2 and the absence of any secondary nucleation:

$$V_T = \left(\frac{\left(\frac{d_U}{2} + t_1 + t_2 \right)^3 - \left(\frac{d_U}{2} + t_1 \right)^3}{\left(\frac{d_U}{2} \right)^3} \right) \frac{\rho_S \cdot m_U \cdot M_T}{\rho_U \cdot M_S \cdot \rho_T}, \quad (1)$$

where t_1 is the thickness of the first silica shell, ρ_S is the density of colloidal silica (2 g/cm^3), ρ_U is the density of the UCNP cores (4.21 g/cm^3), M_T is the molar mass of TEOS (208.32 g/mol), M_S is the molar mass of SiO_2 (60.08 g/mol) and ρ_T is the density of TEOS (0.94 g/cm^3). The added volume of ammonia water always matched that of the added TEOS. The volume of cyclohexane was calculated for each growth step such that the ammonia water concentration in cyclohexane was $3.3 \pm 0.1 \text{ wt } \%$. The concentration of Igepal CO-520 was kept constant at $14 \pm 1 \text{ wt } \%$ in cyclohexane throughout all growth steps in the reverse microemulsion, resulting in an *R*-value for the further shell growth of 1:4.3 (weight ratio) or 1:6.0 (molar ratio). The *R*-value was increased compared to the growth of the first shell to keep the water domain large enough for the increasing size of the particles while maintaining a constant ratio of the number of micelles and the number of particles. The control of the Igepal CO-520 concentration prevents the forma-

tion of core-free micelles and provides the particles with sufficiently large water domains for further TEOS hydrolysis. If the surfactant concentration is too high while the concentrations of the other reactants is constant or too low, new micelles are formed, which can facilitate the formation of core-free silica particles. Ding et al. used a slightly lower concentration of ammonia water ($1 \text{ wt } \%$ compared to $1.7 \pm 0.5 \text{ wt } \%$ in the present work) and a lower surfactant concentration ($5.6 \text{ wt } \%$ compared to $16 \text{ wt } \%$) for the growth of a single shell, corresponding to an *R*-value of 1:5.5 for iron oxide core particles with diameters of 12.2 nm . Under these conditions, they were able to vary the added amount of TEOS in a range of $75\text{--}600 \text{ }\mu\text{L}$ so that they could adjust the thickness of the silica shell. Katagiri et al. used ammonia water and surfactant concentrations of $0.83 \text{ wt } \%$ and $5.1 \text{ wt } \%$, respectively, for iron oxide particles with diameters of 10 nm ($R = 1: 6.1$ in weight ratio). They used the same concentration of both components also for the stepwise growth of a thicker silica shell. This concentration was significantly lower than the concentration ($16 \text{ wt } \%$) used in this work, especially in the case of Igepal CO-520. This difference could explain why the maximum size of the core-shell particles did not exceed 50 nm before core-free particles started to form in the experiments conducted by Katagiri and co-workers [23]. These studies and their comparison underline the many possibilities of varying the parameters of the shell growth in the reverse microemulsion approach. However, we could show that the reported *R*-value can be utilized to synthesize a wide range of silica shells with different thicknesses.

In a typical example, a UCNP core (NaYF_4 doped with Yb and Er; core sample C1) with a diameter of $24 \pm 1 \text{ nm}$ was coated

with silica shells through a stepwise reverse microemulsion synthesis. The silica shell thickness increased here in four growth steps from 7 to 44 nm (Figure 1). The terminology used for each shell is C1_1S for the first shell, C1_2S for the second shell and so on.

For all growth steps, the measured shell thicknesses from STEM agree relatively well with the calculated shell thicknesses (Table 1 and Table S1, Supporting Information File 1). This supports that all TEOS grows as SiO₂ on the existing core particles. The observation that the measured shell thickness was slightly larger than the calculated one can be explained by the fact that the total mass of the particles, including the oleate ligands, was used for the calculations. The oleate ligands are, however, exchanged during shell growth in the inverse microemulsion [36,47]. The oleate content for particles of this size was in the range of 5–10 wt % as shown by thermogravimetric analysis [57]. The z-average values of the samples after the first and second shell indicate low colloidal stability of the particles, which is also supported by the high PDI values suggesting partial aggregation (Table 1). Repeated centrifugation and redispersion in ethanol were carried out in an attempt to improve the colloidal stability by removing the remaining surfactant from the surface. However, this procedure did not increase the stability of the particles. This colloidal instability of NPs with thin silica shells obtained from the reverse microemulsion syntheses was also reported by several other authors before [53–56]. In contrast to these findings, after the third and fourth steps of shell growth, the particles have a relatively low PDI, and the z-average diameters match the radii obtained from STEM much more closely, indicating their high colloidal stability. The zeta potential becomes increasingly more negative with the growth of thicker silica shells. The particles after the second step of the silica growth (C1_2S) have a zeta potential of -32 ± 1 mV (Table 1), which decreases to -41 ± 1 mV after the formation of the third shell. The samples after the fourth silica shell growth step have a zeta potential of -45 ± 1 mV, which is in the range typically found for particles from Stöber-like growth processes [58]. This increasingly more

negative zeta potential likely arises from a decrease of the surface concentration of Igepal CO-520 on the growing silica-coated particles and was repeatedly found in this work. Due to the increased colloidal stability, it was then possible to continue to further grow the shells in a Stöber-like growth process. Under these conditions, the silica growth itself is much faster than in a reverse microemulsion [59]. Moreover, modified Stöber processes where TEOS is continuously added allow for the growth of silica layers that are several hundred nanometers thick at high precision in one step [28]. The particles were transferred into ethanol with a rather high ammonia water concentration (14.4 wt %). A fifth shell was then grown on sample C1_4S by continuously adding TEOS. In this way, the particles could be grown directly from 112 ± 4 nm diameter to a size of 321 ± 16 nm (sample C1_5S). A z-average value that is similar to the diameter measured in STEM and a relatively low PDI of this sample (Table 1) indicate the formation of monodisperse particles (Figure 1F). This result shows that the Stöber method allowed for a significant increase in the particle size within one step. In the case of sample C1_4S, the particle volume could be grown more than 23-fold.

Core-free silica particles were formed in one growth step during the stepwise growth process (Figure 1C). To obtain further shells of the same thickness as the initial silica shell, several smaller growth steps were carried out in the later syntheses described in the following. Smaller amounts of TEOS were added per step, and the other chemicals were also added in correspondingly smaller steps (Figure S4 in Supporting Information File 1). The ammonia water and Igepal CO-520 concentrations as well as the R-values were the same as used for the initial syntheses. Smaller growth steps helped to prevent possible minor new nucleation of silica due to a locally too high TEOS concentration. Moreover, smaller growth steps have the advantage that accidentally formed secondary nuclei can be removed more easily by centrifugation since the difference between newly formed particles and the core-shell particles is larger. When the zeta potential was sufficiently negative (-50 ± 8 mV), the microemulsion was broken, and the particles were transferred to

Table 1: Overview of the size, silica shell thickness, z-average, PDI and zeta potential of each silica-coated sample. DLS of the core was performed in cyclohexane, while the silica-coated samples were measured in ethanol, and the zeta potential was measured in water.

sample	shell	total diameter (STEM) [nm]	silica shell thickness (STEM) [nm]	z-average [nm]	PDI	zeta potential [mV]
C1	core	24 ± 2	0	44 ± 2	0.360 ± 0.020	n.d.
C1_1S	1st	38 ± 2	7 ± 2	89 ± 2	0.090 ± 0.020	n.d.
C1_2S	2nd	59 ± 3	18 ± 4	98 ± 2	0.110 ± 0.030	-32 ± 1
C1_3S	3rd	93 ± 4	35 ± 4	116 ± 2	0.013 ± 0.005	-41 ± 1
C1_4S	4th	112 ± 4	44 ± 4	137 ± 2	0.040 ± 0.010	-45 ± 1
C1_5S (Stöber)	5th	321 ± 16	149 ± 16	376 ± 9	0.095 ± 0.020	-37 ± 1

an ethanol solution containing ammonia water. Subsequently, a modified Stöber growth was performed where TEOS was continuously added over several hours with a peristaltic pump. In this way, particles with a diameter exceeding 500 nm and a narrow size distribution could be grown within one step (Figure S4H–J in Supporting Information File 1).

Overall, the growth of a silica shell with the reverse microemulsion method initially decreased the colloidal stability of the particles, as shown by the diameter of the UCNP as determined by TEM and the deviating z-average and low zeta potential values. The particle stability could be increased by growing a thicker silica shell through a further stepwise use of the reverse microemulsion method. The silica shell growth using the Stöber method did not significantly change the colloidal properties of the dispersion, which is shown by the z-average value and the relatively narrow PDI value of sample C1_5S. The z-average value exceeds the average diameter derived from TEM by $(17 \pm 5)\%$. The dispersion has a high colloidal stability due to the highly negative zeta potential of the particles, which is typical for silica dispersions from Stöber-like growth processes containing particles of similar sizes [58,60,61]. Since the surface of the particles corresponds to that of particles from a standard Stöber synthesis, the colloids can be functionalized with the same diverse methods as Stöber silica particles [58].

Figure S5 in Supporting Information File 1 shows X-ray diffraction (XRD) measurements of the oleate-coated UCNP cores C1 and the same particles after the growth of two, three, four and five additional silica shells (samples C1_2S, C1_3S, C1_4S, and C1_5S). These data exclude a possible influence of the silica shell on the crystallinity of the UCNP core. The cores have a predominantly hexagonal crystal structure. Minor peaks at 47° (220) and 55° (311) 2θ indicate a small fraction of the cubic phase. The XRD patterns of the silica-coated UCNPs show the same peaks (mainly the hexagonal phase) with decreasing intensity as the silica shell thickness increases. Accordingly, the broad signal of the amorphous silica at $2\theta = 20\text{--}25^\circ$ becomes more dominant with increasing thickness of the silica shell. These data indicate that the crystal structure of the UCNP cores is not changed during the silica shell formation process.

Figure 3 shows the upconversion luminescence (UCL) spectra of the UCNP cores before the growth of a silica shell (sample C2) and after coating with one (sample C2_1S, shell thickness: 11 ± 1 nm) and seven silica layers (sample C2_7S, shell thickness: 61 ± 1 nm). Sample C2_7S corresponds to the final product with a thick silica layer produced in a modified Stöber growth. All spectra show the typical green and red Er^{3+} emission bands of $\text{NaYF}_4:(\text{Yb},\text{Er})$ UCNPs [62–64]. The silica coating only slightly alters the relative spectral distribution of

the UCL spectra. The most pronounced effect is the slight reduction of the green emission bands at 520 and 540 nm of the UCNPs with the thinnest silica shell (sample C2_1S) compared to the oleate-functionalized particles. Similar effects have been reported previously for silanized UCNPs after their transfer into water [65]. They can be explained by the presence of UCL quenching by high-energy vibrators such as $-\text{OH}$ groups from ethanol and maybe also from silanol or silanolate groups of the silica network. The increase in non-radiative relaxation processes by surface quenching effects caused for example by Igepal CO-520 after silica coating can lead to a decrease of the UCL intensity [66].

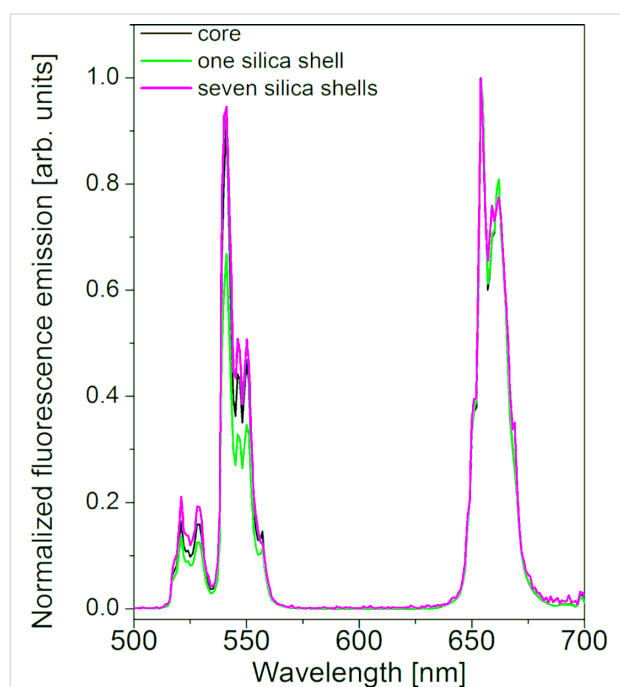


Figure 3: UCL spectra of the oleate coated UCNP cores C2 (20 ± 2 nm diameter, black line) in cyclohexane and after coating with one silica shell (sample C2_1S, shell thickness: 11 ± 1 nm, green line) and seven shells (sample C2_7S, shell thickness: 61 ± 1 nm, pink line) in ethanol. All spectra are normalized at 655 nm for better comparison. The excitation power density was 2 W/cm^2 at 980 nm.

The considerable influence of such quenchers on UCL spectral distribution and UCL quantum yield has been previously shown by us by comparing the excitation power density-dependent UCL of bare UCNPs in organic solvents, water, and D_2O [67]. A further increase in silica shell thickness barely alters the red-to-green intensity ratio. Here it needs to be kept in mind that the different sizes of the silica-coated particles can affect their scattering characteristics and thereby the excitation power density distribution within the optical cell used for the UCL measurements. In the case of UCL, which depends on the excitation power density, this can influence both the UCL intensity and the UCL spectral distribution. In general, the coating with a

thick silica shell is not expected to strongly affect the brightness of the UCNPs as long as the two properties absorption cross section and fluorescence quantum yield, which determine the particle brightness, are not considerably affected. Nevertheless, it must be kept in mind that the increased scattering originating from larger particles can affect the excitation power density that is effective on the dispersed UCNP. As the emission spectra and the relative spectral distribution of UCL both depend on the excitation power density, this can in principle also affect the relative intensity ratios of the green and red emission bands [68,69].

Conclusion

A concept for the growth of silica shells of sizes between 5 and 250 nm on oleate-stabilized UCNPs was developed. This concept comprises (1) the growth of an initial 5–11 nm thick shell on the oleate-stabilized particles in a reverse microemulsion using the surfactant Igepal CO-520 and an ammonia water concentration of 1.7 ± 0.5 wt % and (2) a further stepwise growth of these particles in the same reverse microemulsion without any intermediate isolation or purification steps of the nanoparticles. In each step, the same volumes of TEOS and ammonia water were added, and the volumes of cyclohexane and Igepal CO-520 were increased so that the ammonia water concentration in cyclohexane was 3.3 ± 0.1 wt %, and that of Igepal CO-520 in cyclohexane was kept constant at 14 ± 1 wt %. In this way, the number of micelles remained constant to match the number of UCNP cores. Also, the micelle size was adjusted to ensure that they were large enough to host the growing core-shell particles. Simultaneously, the aqueous domain was kept small enough to prevent the formation of core-free silica particles. In this stepwise procedure, the zeta potential of the particles becomes increasingly more negative. When the zeta potential of the silica-coated UCNPs reached -40 mV, the particles which then had a silica shell thickness of about 40–50 nm could be dispersed in an ammoniacal ethanol solution with a rather high ammonia water concentration (12–13 wt %) and could be grown by continuous addition of TEOS in one step up to a diameter of more than 500 nm in a modified Stöber process. This stepwise procedure was necessary for growing thick silica shells on the UCNPs since a direct growth of silica on oleate-functionalized UCNPs was not possible in a Stöber-like growth process affording NPs with a hydrophilic surface. A Stöber growth of a silica shell on the UCNPs coated with only a thin silica shell leads mainly to coalesced multicore particles. The latter is related to the relatively small zeta potential of these silica-coated UCNPs which are not very stable in ammoniacal ethanol. Despite the rather harsh conditions during the growth process, this procedure does not influence the crystal structure of the UCNPs and the shape of the UCL emission spectra. This stepwise shell growth can

most likely be also utilized for the coating of other NPs with similar hydrophobic surface chemistries of the initial particles such as iron oxide NPs or semiconductor NPs. Further applications can include the covalent attachment of biomolecules such as peptides, antibodies or nucleic acids for bioimaging applications or fluorescence assays. The growth of a mesoporous silica shell on a microporous silica shell can also be applied for the subsequent use of these nanomaterials for drug loading and delivery [69].

Experimental

All syntheses were carried out with standard glass equipment. The reaction vessels were cleaned before use with hydrofluoric acid (8 vol %) and were then repeatedly rinsed with water. The redispersion of the nanoparticles was carried out using an ultrasonic bath (Sonorex RK512H (860 W, 35 kHz) from Bandelin). Alternatively, a sonotrode UP200H (200 W, 24 kHz) from Hielscher was used. Ultrapure water (Millipore; filter size = $0.22 \mu\text{m}$, $\rho = 18.2 \text{ M}\Omega \text{ cm}$) was used for all syntheses. For the controlled addition of TEOS, a peristaltic pump (REGLO Digital MS-2/8-160) from Ismatec with a TYGON R-3603 tubing, type AME-01 or an LA-30 syringe pump from Landgraf Laborsysteme HLL GmbH was used.

Materials

Cyclohexane (tech. 99.5%) and ammonia water (p.a., 25 wt % NH_3) were purchased from Roth. Oleic acid (OA, 90%), erbium chloride hexahydrate ($\text{ErCl}_3 \cdot 6\text{H}_2\text{O}$, 99.9%), ytterbium chloride hexahydrate ($\text{YbCl}_3 \cdot 6\text{H}_2\text{O}$, 99.9%) and yttrium chloride hexahydrate ($\text{YCl}_3 \cdot 6\text{H}_2\text{O}$, 99.9%) were received from ABCR. Sodium hydroxide (NaOH, 99%) was obtained from Grüssing, Ethanol (EtOH, 100%) from Berkel AHK and hydrofluoric acid (HF, 30%) from Riedel de Haën. Polyoxyethylene (5) nonylphenyl ether (Igepal[®] CO-520), ammonium fluoride (NH_4F , 99.8%), 1-octadecene (tech. 95%), sodium oleate (82%), tetraethyl orthosilicate (TEOS, 98%) as well as yttrium-, ytterbium- and erbium standards for inductively coupled plasma optical emission spectroscopy (ICP-OES) measurements (TraceCERT[®], $c = 1000 \text{ mg/mL}$) were purchased from Sigma Aldrich. All chemicals were used without further purification.

Synthesis

$\text{NaYF}_4:(\text{Yb},\text{Er})$ UCNPs were prepared from the corresponding lanthanide oleates [14,70] according to a modified procedure from Na and co-workers [16]. For details, see Supporting Information File 1.

Growth of the silica shell

Shell growth in a reverse microemulsion

The synthesis of the silica coating was based on a modified microemulsion method [24,71]. The following describes a

typical microemulsion synthesis for the silica coating of UCNPs.

For the first silica shell growth with a calculated thickness of 5 ± 1 nm, a dispersion of UCNPs (diameter = 24 ± 2 nm; $c = 3$ g/L in 11 mL of cyclohexane) was mixed with 0.154 mL of Igepal CO-520. After sonication for 10 min, 1.213 mL of Igepal CO-520 was added, and after brief mixing with sonication, 0.159 mL of ammonia water were added, and the dispersion was sonicated for another 20 min. Finally, 0.159 mL of TEOS were added, and the whole mixture was sonicated for at least 1 h. Generally, a concentration of 16 ± 1 wt % in cyclohexane was used for Igepal CO-520, and the ammonia water concentration was 1.7 ± 0.7 wt % (density of ammonia water was 0.90 ± 0.09 g/mL for a concentration of 25 wt % NH_3) in cyclohexane for the growth of the first shell. Finally, the dispersion was stirred for 12 h at 1200 rpm at room temperature.

For the further stepwise growth of the silica shells, additional cyclohexane, Igepal CO-520 and ammonia water were added sequentially to the non-purified dispersion to obtain a constant surfactant concentration of 14 ± 1 wt % in cyclohexane and a maximal ammonia water concentration of 3.3 ± 0.1 wt % in cyclohexane. TEOS was added gradually with a rate of $20.8 \mu\text{L}/\text{min}$ through a peristaltic pump while the dispersion was stirred for 12 h at 1200 rpm at room temperature. Alternatively, a vortex shaker from Scientific Industries, Inc. (Model no. G560E) was used.

It was important that the microemulsion was not broken during the entire synthesis, i.e., the last layer of silica was grown before the particles were precipitated with ethanol. In Table S1 in Supporting Information File 1, an example of the amounts of solvent and reactant for a typical multi-step silica shell synthesis with the reverse microemulsion method is given. Table S2 summarizes the surfactant concentration ($c(\text{Igepal})$), ammonia water concentration ($c(\text{ammonia water})$) and the ammonia water-to-Igepal CO-520 mass ratio in each growth step of the silica shell.

After the last growth step, the particles were precipitated by adding 5–10 mL of EtOH and washed three times by repeated centrifugation (1200g, 1 h) and redispersion in 10 mL of EtOH and finally redispersed in 10–15 mL of EtOH.

Shell growth via a modified Stöber approach

The growth of silica shells on UCNPs via a modified Stöber method [25,28] was carried out after the multistep growth of silica shells (shell thickness = 40–50 nm) with the reverse microemulsion approach. At this point, the zeta potential of the silica particles reached a value below -40 mV in water at pH 7.

In a typical reaction (growth from 112 ± 4 nm diameter to an intended diameter of 300 nm), 2 mL of ammonia water were added to 16.25 mL of an ethanolic dispersion of silica-coated UCNPs ($c = 1$ g/L). Subsequently, 1.1 mL of TEOS were added dropwise with the help of a peristaltic pump ($v = 20.8 \mu\text{L}/\text{min}$) to this mixture under magnetic stirring (600 rpm). After the addition was completed, the reaction mixture was stirred for another 12 h. Then, the particles were washed three times by centrifugation (3300g, 1 h) and redispersion in 10–20 mL of EtOH with the help of an ultrasonic bath and were finally redispersed in 10 mL of EtOH.

Characterization

Scanning transmission electron microscopy (STEM)

STEM images were recorded with a Hitachi SU 8030 scanning electron microscope in STEM mode with an electron acceleration voltage of 30 kV and a current of 20 μA . A droplet of a dispersion ($c = 0.5$ –1 g/L) of the particles in either cyclohexane for oleate-functionalized UCNP cores or ethanol for silica-coated UCNPs was dried on a carbon-coated copper grid (Cu 400 mesh, Quantifoil®: 100 carbon support films). The images analysis was carried out with the software FIJI.

Dynamic light scattering (DLS) and electrophoretic light scattering

The DLS measurements were carried out with a Zetasizer Nano ZS from Malvern Instruments at 25 °C using a wavelength of 633 nm. The uncoated cores were dispersed in cyclohexane, and the silica-coated particles were dispersed in ethanol and filtered with a sterile syringe filter (pore size: 0.2 μm ; materials: nylon or polytetrafluoroethylene (PTFE) for particles dispersed in cyclohexane and nylon or regenerated cellulose for particles dispersed in ethanol, Rotilab). Zeta potential measurements of the aqueous dispersions were carried out with a Zetasizer Nano ZS in capillary zeta cells DTS 1070 from Malvern Instruments. The concentration of the samples in all measurements was between 0.5 and 1 mg/mL.

Measurements of the upconversion luminescence (UCL)

The UCL measurements were carried out with a FluoroMax-4 spectrometer from Horiba Jobin Yvon equipped with a 2 W 980 nm laser diode from Insaneware-Robert Nowak and an Edinburgh Instruments spectrofluorometer FLS-980 equipped with an electrically modulated 8 W 978 nm laser diode (950 μs long square pulses) and a red-extended photomultiplier tube (Hamamatsu R2658P). Quartz glass cuvettes (QS Suprasil, 5 mm, Hellma or VWR) were used in all measurements performed at room temperature. The concentration of the samples was 1–2 g/L in cyclohexane for oleate-capped UCNPs or ethanol for silica-coated UCNP.

Inductively coupled plasma-optical emission spectroscopy (ICP-OES)

For the determination of the elemental composition of the UCNP samples, 1 mL of the dispersions ($c = 5$ g/L in cyclohexane for the oleate-coated UCNPs or in ethanol for the silica-coated UCNP) was dried. The dried particles were dissolved in 1 mL of aqua regia for at least 30 min and diluted with at least 5 mL of ultrapure water. The measurements were carried out using an iCAP 6000 Series ICP Spectrometer from Thermo Scientific with a radial optical approach. A series of solutions with different concentrations were prepared separately for calibration from an yttrium standard for ICP ($c(\text{Y}^{3+}) = 10, 20$ and 40 ppm), ytterbium standard for ICP ($c(\text{Yb}^{3+}) = 10, 20$ and 40 ppm) or erbium standard for ICP ($c(\text{Er}^{3+}) = 1, 5$ and 10 ppm).

X-ray diffraction (XRD) measurements

A minimum amount of 10 mg of dried particles were used for the XRD measurements. The XRD device was a Rigaku SmartLab 3 kW with a DTex Ultra 250 detector (40 kV, 30 mA) equipped with a Cu $\text{K}\alpha_1$ radiation source and a radiation wavelength of 0.15405 nm. The angle range of the measurements was $10\text{--}60^\circ$ 2θ , measurement time was 60 s/ 0.3° .

Supporting Information

Supporting Information File 1

Synthesis details, additional STEM images, and XRD data.

[<https://www.beilstein-journals.org/bjnano/content/supplementary/2190-4286-10-231-S1.pdf>]

Acknowledgements

This research was supported by the Deutsche Forschungsgemeinschaft (DFG) within the ERA-NET program (grants RE 1203/20-1 and GR 2113/6-1), the EU (COST 1403) and the Freie Universität Berlin. We thank Dr. S. Berends from the research group of Prof. Dr. M. Lerch (Technische Universität Berlin) for the XRD measurements, Prof. Dr. R. Haag (Freie Universität Berlin) for access to the Dynamic Light Scattering setup and Prof. Dr. E. Rühl (Freie Universität Berlin) for access to the fluorescence spectrometer.

ORCID® iDs

Cynthia Kambuan - <https://orcid.org/0000-0002-9415-0952>

Ute Resch-Genger - <https://orcid.org/0000-0002-0944-1115>

Christina Graf - <https://orcid.org/0000-0002-3308-5640>

Preprint

A non-peer-reviewed version of this article has been previously published as a preprint doi:10.3762/bxiv.2019.62.v1

References

- Bünzli, J.-C. G. *Chem. Rev.* **2010**, *110*, 2729–2755. doi:10.1021/cr900362e
- Wang, F.; Liu, X. *Chem. Soc. Rev.* **2009**, *38*, 976–989. doi:10.1039/b809132n
- Auzel, F. *Chem. Rev.* **2004**, *104*, 139–174. doi:10.1021/cr020357g
- Heer, S.; Lehmann, O.; Haase, M.; Güdel, H.-U. *Angew. Chem., Int. Ed.* **2003**, *42*, 3179–3182. doi:10.1002/anie.200351091
- Soukka, T.; Rantanen, T.; Kuningas, K. *Ann. N. Y. Acad. Sci.* **2008**, *1130*, 188–200. doi:10.1196/annals.1430.027
- Wang, X.; Li, Y. *Chem. Commun.* **2007**, 2901–2910. doi:10.1039/b700183e
- Wang, M.; Mi, C.-C.; Wang, W.-X.; Liu, C.-H.; Wu, Y.-F.; Xu, Z.-R.; Mao, C.-B.; Xu, S.-K. *ACS Nano* **2009**, *3*, 1580–1586. doi:10.1021/nn900491j
- Heer, S.; Kömpe, K.; Güdel, H.-U.; Haase, M. *Adv. Mater. (Weinheim, Ger.)* **2004**, *16*, 2102–2105. doi:10.1002/adma.200400772
- Zhao, J.; Sun, Y.; Kong, X.; Tian, L.; Wang, Y.; Tu, L.; Zhao, J.; Zhang, H. *J. Phys. Chem. B* **2008**, *112*, 15666–15672. doi:10.1021/jp805567k
- Ehlert, O.; Thomann, R.; Darbandi, M.; Nann, T. *ACS Nano* **2008**, *2*, 120–124. doi:10.1021/nn7002458
- Kowalik, P.; Elbaum, D.; Mikulski, J.; Fronc, K.; Kamińska, I.; Morais, P. C.; Eduardo de Souza, P.; Nunes, R. B.; Veiga-Souza, F. H.; Gruzel, G.; Minikayev, R.; Wojciechowski, T.; Sienkiewicz-Szablewska, E.; Szewczyk, M.; Pawlyta, M.; Sienkiewicz, A.; Łapiński, M.; Zajdel, K.; Stępień, P.; Szczepkowski, J.; Jastrzębski, W.; Frontczak-Baniewicz, M.; Paszkowicz, W.; Sikora, B. *RSC Adv.* **2017**, *7*, 30262–30273. doi:10.1039/c6ra25383k
- Yi, G. S.; Chow, G. M. *Adv. Funct. Mater.* **2006**, *16*, 2324–2329. doi:10.1002/adfm.200600053
- Lu, H.; Yi, G.; Zhao, S.; Chen, D.; Guo, L.-H.; Cheng, J. *J. Mater. Chem.* **2004**, *14*, 1336–1341. doi:10.1039/b315103d
- Wei, Y.; Lu, F.; Zhang, X.; Chen, D. *Chem. Mater.* **2006**, *18*, 5733–5737. doi:10.1021/cm0606171
- Wang, L.; Li, Y. *Chem. Mater.* **2007**, *19*, 727–734. doi:10.1021/cm061887m
- Na, H.; Woo, K.; Lim, K.; Jang, H. S. *Nanoscale* **2013**, *5*, 4242–4251. doi:10.1039/c3nr00080j
- Homann, C.; Krukewitt, L.; Frenzel, F.; Grauel, B.; Würth, C.; Resch-Genger, U.; Haase, M. *Angew. Chem., Int. Ed.* **2018**, *57*, 8765–8769. doi:10.1002/anie.201803083
- Liu, Z.; Yi, G.; Zhang, H.; Ding, J.; Zhang, Y.; Xue, J. *Chem. Commun.* **2008**, *6*, 694–696. doi:10.1039/b715402j
- Andresen, E.; Resch-Genger, U.; Schäferling, M. *Langmuir* **2019**, *35*, 5093–5113. doi:10.1021/acs.langmuir.9b00238
- Resch-Genger, U.; Gorris, H. H. *Anal. Bioanal. Chem.* **2017**, *409*, 5855–5874. doi:10.1007/s00216-017-0499-z
- Zheng, Y.; Wang, Y.; Guo, Y.; Chen, L. *Mater. Res. Bull.* **2019**, *113*, 209–214. doi:10.1016/j.materresbull.2019.01.030
- Koole, R.; van Schooneveld, M. M.; Hilhorst, J.; Castermans, K.; Cormode, D. P.; Strijkers, G. J.; de Mello Donega, C.; Vanmaekelbergh, D.; Griffioen, A. W.; Nicolay, K.; Fayad, Z. A.; Meijerink, A.; Mulder, W. J. M. *Bioconjugate Chem.* **2008**, *19*, 2471–2479. doi:10.1021/bc800368x
- Katagiri, K.; Narahara, M.; Sako, K.; Inumaru, K. *J. Sol-Gel Sci. Technol.* **2017**, *84*, 110–117. doi:10.1007/s10971-017-4479-8

24. Wang, J.; Shah, Z. H.; Zhang, S.; Lu, R. *Nanoscale* **2014**, *6*, 4418–4437. doi:10.1039/c3nr06025j
25. Stöber, W.; Fink, A.; Bohn, E. *J. Colloid Interface Sci.* **1968**, *26*, 62–69. doi:10.1016/0021-9797(68)90272-5
26. Graf, C.; Vossen, D. L. J.; Imhof, A.; van Blaaderen, A. *Langmuir* **2003**, *19*, 6693–6700. doi:10.1021/la0347859
27. Liz-Marzán, L. M.; Giersig, M.; Mulvaney, P. *Langmuir* **1996**, *12*, 4329–4335. doi:10.1021/la9601871
28. Reculusa, S.; Poncet-Legrand, C.; Ravaine, S.; Mingotaud, C.; Duguet, E.; Bourgeat-Lami, E. *Chem. Mater.* **2002**, *14*, 2354–2359. doi:10.1021/cm0116525
29. Kang, S.; Hong, S. I.; Choe, C. R.; Park, M.; Rim, S.; Kim, J. *Polymer* **2001**, *42*, 879–887. doi:10.1016/s0032-3861(00)00392-x
30. Arriagada, F. J.; Osseo-Asare, K. *J. Colloid Interface Sci.* **1999**, *211*, 210–220. doi:10.1006/jcis.1998.5985
31. Arriagada, F. J.; Osseo-Asare, K. *Colloids Surf., A* **1999**, *154*, 311–326. doi:10.1016/s0927-7757(98)00870-x
32. Osseo-Asare, K.; Arriagada, F. J. *J. Colloid Interface Sci.* **1999**, *218*, 68–76. doi:10.1006/jcis.1999.6232
33. Osseo-Asare, K.; Arriagada, F. J. *Colloids Surf.* **1990**, *50*, 321–339. doi:10.1016/0166-6622(90)80273-7
34. Nann, T.; Mulvaney, P. *Angew. Chem., Int. Ed.* **2004**, *43*, 5393–5396. doi:10.1002/anie.200460752
35. Koole, R.; van Schooneveld, M. M.; Hilhorst, J.; de Mello Donegá, C. D.; t Hart, D. C.; van Blaaderen, A.; Vanmaekelbergh, D.; Meijerink, A. *Chem. Mater.* **2008**, *20*, 2503–2512. doi:10.1021/cm703348y
36. Ding, H. L.; Zhang, Y. X.; Wang, S.; Xu, J. M.; Xu, S. C.; Li, G. H. *Chem. Mater.* **2012**, *24*, 4572–4580. doi:10.1021/cm302828d
37. Li, T.; Moon, J.; Morrone, A. A.; Mecholsky, J. J.; Talham, D. R.; Adair, J. H. *Langmuir* **1999**, *15*, 4328–4334. doi:10.1021/la970801o
38. Darbandi, M.; Thomann, R.; Nann, T. *Chem. Mater.* **2005**, *17*, 5720–5725. doi:10.1021/cm051467h
39. Lee, D. C.; Mikulec, F. V.; Pelaez, J. M.; Koo, B.; Korgel, B. A. *J. Phys. Chem. B* **2006**, *110*, 11160–11166. doi:10.1021/jp060974z
40. Yamada, H.; Urata, C.; Ujije, H.; Yamauchi, Y.; Kuroda, K. *Nanoscale* **2013**, *5*, 6145–6153. doi:10.1039/c3nr00334e
41. Yamada, H.; Ujije, H.; Urata, C.; Yamamoto, E.; Yamauchi, Y.; Kuroda, K. *Nanoscale* **2015**, *7*, 19557–19567. doi:10.1039/c5nr04465k
42. Li, Z.; Zhang, Y.; Jiang, S. *Adv. Mater. (Weinheim, Ger.)* **2008**, *20*, 4765–4769. doi:10.1002/adma.200801056
43. Abdul Jalil, R.; Zhang, Y. *Biomaterials* **2008**, *29*, 4122–4128. doi:10.1016/j.biomaterials.2008.07.012
44. Hoar, T. P.; Schulman, J. H. *Nature* **1943**, *152*, 102–103. doi:10.1038/152102a0
45. Penninkhof, J. J.; Moroz, A.; van Blaaderen, A.; Polman, A. *J. Phys. Chem. C* **2008**, *112*, 4146–4150. doi:10.1021/jp710780j
46. Lahtinen, S.; Lyytikäinen, A.; Pääkkilä, H.; Hömppi, E.; Perälä, N.; Lastusaari, M.; Soukka, T. *J. Phys. Chem. C* **2017**, *121*, 656–665. doi:10.1021/acs.jpcc.6b09301
47. Zhang, M.; Cushing, B. L.; O'Connor, C. J. *Nanotechnology* **2008**, *19*, 085601. doi:10.1088/0957-4484/19/8/085601
48. Yi, D. K.; Lee, S. S.; Papaefthymiou, G. C.; Ying, J. Y. *Chem. Mater.* **2006**, *18*, 614–619. doi:10.1021/cm0512979
49. Kostiv, U.; Patsula, V.; Šlouf, M.; Pongrac, I. M.; Škokić, S.; Radmilović, M. D.; Pavičić, I.; Vrček, I. V.; Gajović, S.; Horák, D. *RSC Adv.* **2017**, *7*, 8786–8797. doi:10.1039/c7ra00224f
50. Rancan, F.; Gao, Q.; Graf, C.; Troppens, S.; Hadam, S.; Hackbarth, S.; Kembuan, C.; Blume-Peytavi, U.; Rühl, E.; Lademann, J.; Vogt, A. *ACS Nano* **2012**, *6*, 6829–6842. doi:10.1021/nn301622h
51. Lemyre, J.-L.; Lamarre, S.; Beaupre, A.; Ritcey, A. M. *Langmuir* **2010**, *26*, 10524–10531. doi:10.1021/la100541m
52. Fenn, E. E.; Wong, D. B.; Giammanco, C. H.; Fayer, M. D. *J. Phys. Chem. B* **2011**, *115*, 11658–11670. doi:10.1021/jp206903k
53. Hlaváček, A.; Sedlmeier, A.; Skládal, P.; Gorris, H. H. *ACS Appl. Mater. Interfaces* **2014**, *6*, 6930–6935. doi:10.1021/am500732y
54. Johnson, N. J. J.; Sangeetha, N. M.; Boyer, J.-C.; van Veggel, F. C. J. M. *Nanoscale* **2010**, *2*, 771–777. doi:10.1039/b9nr00379g
55. Jana, N. R.; Earhart, C.; Ying, J. Y. *Chem. Mater.* **2007**, *19*, 5074–5082. doi:10.1021/cm071368z
56. Liu, F.; Zhao, Q.; You, H.; Wang, Z. *Nanoscale* **2013**, *5*, 1047–1053. doi:10.1039/c2nr33046f
57. Bergmann, O. Synthese und Charakterisierung von Upconversion-Nanopartikeln. Master Thesis, Hochschule Darmstadt – University of Applied Sciences, Germany, 2018.
58. Graf, C.; Gao, Q.; Schütz, I.; Noufele, C. N.; Ruan, W.; Posselt, U.; Korotianskiy, E.; Nordmeyer, D.; Rancan, F.; Hadam, S.; Vogt, A.; Lademann, J.; Hauke, V.; Rühl, E. *Langmuir* **2012**, *28*, 7598–7613. doi:10.1021/la204913t
59. Knopp, D.; Tang, D.; Niessner, R. *Anal. Chim. Acta* **2009**, *647*, 14–30. doi:10.1016/j.aca.2009.05.037
60. Graf, C. Silica, Amorphous. *Kirk-Othmer Encyclopedia of Chemical Technology*; John Wiley & Sons, Inc.: Hoboken, NJ, U.S.A., 2018; pp 1–43. doi:10.1002/0471238961.0113151823010404.a01.pub3
61. Branda, F.; Silvestri, B.; Costantini, A.; Luciani, G. *Colloids Surf., B* **2015**, *135*, 840–845. doi:10.1016/j.colsurfb.2015.03.033
62. Chen, G.; Qiu, H.; Prasad, P. N.; Chen, X. *Chem. Rev.* **2014**, *114*, 5161–5214. doi:10.1021/cr400425h
63. Haase, M.; Schäfer, H. *Angew. Chem., Int. Ed.* **2011**, *50*, 5808–5829. doi:10.1002/anie.201005159
64. Fujii, M.; Nakano, T.; Imakita, K.; Hayashi, S. *J. Phys. Chem. C* **2013**, *117*, 1113–1120. doi:10.1021/jp309510s
65. Arppe, R.; Hyppänen, I.; Perälä, N.; Peltomaa, R.; Kaiser, M.; Würth, C.; Christ, S.; Resch-Genger, U.; Schäferling, M.; Soukka, T. *Nanoscale* **2015**, *7*, 11746–11757. doi:10.1039/c5nr02100f
66. Wilhelm, S.; Kaiser, M.; Würth, C.; Heiland, J.; Carrillo-Carrion, C.; Muhr, V.; Wolfbeis, O. S.; Parak, W. J.; Resch-Genger, U.; Hirsch, T. *Nanoscale* **2015**, *7*, 1403–1410. doi:10.1039/c4nr05954a
67. Würth, C.; Kaiser, M.; Wilhelm, S.; Grauel, B.; Hirsch, T.; Resch-Genger, U. *Nanoscale* **2017**, *9*, 4283–4294. doi:10.1039/c7nr00092h
68. Kaiser, M.; Würth, C.; Kraft, M.; Hyppänen, I.; Soukka, T.; Resch-Genger, U. *Nanoscale* **2017**, *9*, 10051–10058. doi:10.1039/c7nr02449e
69. Muhr, V.; Wilhelm, S.; Hirsch, T.; Wolfbeis, O. S. *Acc. Chem. Res.* **2014**, *47*, 3481–3493. doi:10.1021/ar500253g
70. Park, J.; An, K.; Hwang, Y.; Park, J.-G.; Noh, H.-J.; Kim, J.-Y.; Park, J.-H.; Hwang, N.-M.; Hyeon, T. *Nat. Mater.* **2004**, *3*, 891–895. doi:10.1038/nmat1251
71. Arriagada, F. J.; Osseo-Asare, K. Synthesis of Nanometer-Sized Silica by Controlled Hydrolysis in Reverse Micellar Systems. In *Colloid Chemistry of Silica*; Berna, H. E., Ed.; Advances in Chemistry, Vol. 234; American Chemical Society: Washington, DC, U.S.A., 1994; pp 113–128. doi:10.1021/ba-1994-0234.ch005

License and Terms

This is an Open Access article under the terms of the Creative Commons Attribution License (<http://creativecommons.org/licenses/by/4.0>). Please note that the reuse, redistribution and reproduction in particular requires that the authors and source are credited.

The license is subject to the *Beilstein Journal of Nanotechnology* terms and conditions: (<https://www.beilstein-journals.org/bjnano>)

The definitive version of this article is the electronic one which can be found at:
[doi:10.3762/bjnano.10.231](https://doi.org/10.3762/bjnano.10.231)



Supporting Information

for

Coating of upconversion nanoparticles with silica nanoshells of 5–250 nm thickness

Cynthia Kembuan, Maysoon Saleh, Bastian Rühle, Ute Resch-Genger and Christina Graf

Beilstein J. Nanotechnol. **2019**, *10*, 2410–2421. doi:10.3762/bjnano.10.231

Synthesis details, additional STEM images, and XRD data

Synthesis of lanthanide oleates as precursors for the synthesis of upconversion nanoparticles

The synthesis procedure was modified from a literature approach for the preparation of iron oleate as a precursor for the synthesis of iron oxide nanoparticles [1,2]. As an example, the synthesis of NaYF₄ nanoparticles doped with 18% Yb and 2% Er from 1 mmol of lanthanide chlorides is described: A mixture of yttrium chloride hexahydrate (0.242 g; 0.78 mmol), ytterbium chloride hexahydrate (0,069 g; 0.18 mmol), and erbium chloride hexahydrate (0.006 g; 0.02 mmol) was dissolved in 3 mL of ultrapure water, 7 mL of ethanol (EtOH) and 7 mL of hexane. Sodium oleate (1.22 g; 4 mmol) was dissolved in a mixture of 2 mL of ultrapure water and 3 mL of ethanol in a 50 mL one-necked flask, then the solution of the mixed lanthanide chlorides was added under stirring. Another 7 mL of hexane were finally added under stirring, and the solution was heated to reflux at 70 °C for 4 h. The solution was then cooled to room temperature, and the organic phase was extracted three times with 20 mL of ultrapure water. Subsequently, the organic phase was separated, volatiles and hexane were removed in vacuo, and the waxy white product was dried under vacuum ($p = 5 \times 10^{-3}$ mbar) in a 100 mL three-necked flask at room temperature before being used in the next step without further purification.

Synthesis of upconversion nanoparticles

The following method is the typical synthesis procedure for 1 mmol NaYF₄:(Yb,Er) nanoparticles from rare earth oleates [3]. The rare earth oleates from the above described method were dissolved in a mixture of 15 mL 1-octadecene and 7 mL oleic acid in a three-necked flask with a heating mantle with an automatic temperature controller under an inert atmosphere of argon, heated under vacuum until the reaction mixture reached 100 °C and kept at 100 °C for 1 h to evaporate all water and hexane. The mixture was cooled down to 50 °C under argon flow. NaOH (100 mg; 2.5 mmol) and NH₄F (148 mg; 4 mmol) were dissolved in 5 mL of MeOH and added to the oleates with a syringe. The mixture was stirred for 30 min at 50 °C at 300 rpm. Afterward, MeOH was evaporated under reduced pressure ($p = 5 \pm 1 \times 10^{-3}$ mbar). After three vacuum degassing and argon flushing cycles to ensure that all MeOH has been evaporated, the reaction mixture was heated to 300 °C and stirred at 500 rpm at this temperature under argon for 1.5 h. After the reaction mixture was cooled down, 15–20 mL of EtOH were added to precipitate the particles. The white powder was redispersed in cyclohexane, precipitated with 5–10 mL of EtOH and centrifuged at 1100g for 15 min. This redispersion/reprecipitation process was repeated three times. The particles were finally redispersed and stored in 10 mL of cyclohexane.

Table S1: Amount of reactants for a stepwise silica coating of UCNP cores with the microemulsion method.

Layer	Thickness of the existing SiO ₂ shell (calculated) [nm]	Calculated growth of the SiO ₂ shell [nm]	Total thickness of the SiO ₂ shell [nm]	Volume of initial dispersion [mL]	Added volumes			
					Cyclohexane [mL]	Igepal [mL]	Ammonia water [mL]	TEOS [mL]
1	0	7	7	0.781	11.00	1.364	0.159	0.159
2	7	11	18	13.463	16.85	1.850	0.674	0.674
3	18	14	32	33.511	66.05	7.29	1.887	1.887
4	32	11	43	97.162	93.10	10.272	2.660	2.660

Table S2: Amount of surfactant, ammonia water concentration, and ammonia water-to-Igepal weight ratio used in the microemulsion synthesis for each sample.

Sample	Shell	c (Igepal) [wt % in cyclohexane]	c (ammonia water) [wt % in cyclohexane]	Ammonia water-to-Igepal weight ratio
C1_1S	1st	15.90	1.67	1:9.5
C1_2S	2nd	14.79	3.45	1:4.3
C1_3S	3rd	14.32	3.34	1:4.3
C1_4S	4th	14.22	3.31	1:4.3

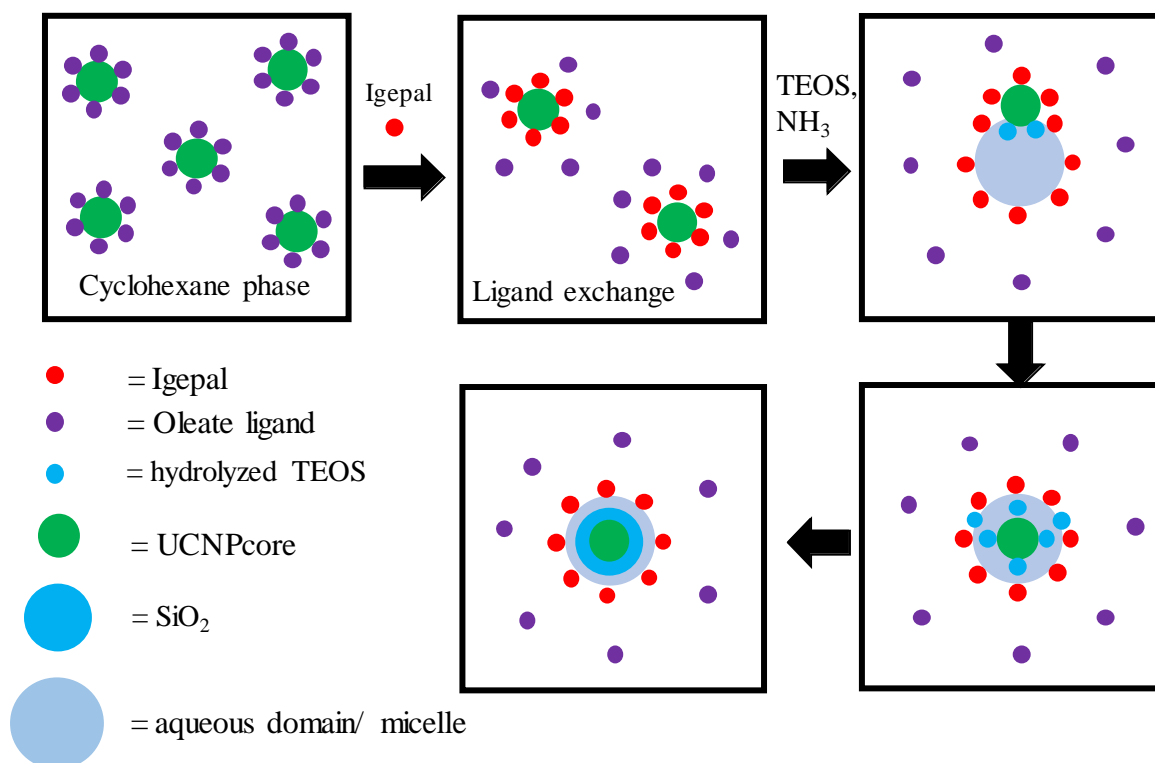


Figure S1: Scheme of microemulsion synthesis for coating oleate-functionalized UCNP cores with a first thin silica shell. Upon addition of surfactant to the UCNP dispersion, a ligand exchange between oleate ligands and the surfactant occurs. Upon addition of TEOS and NH₃, aqueous micelles are formed, and TEOS is hydrolyzed at the interface between the oil (cyclohexane) and the water phase. A second ligand exchange occurs between hydrolyzed TEOS (silica monomers) and Igepal, which transfers the UCNP into the micelles where the condensation reaction of the silica monomers take place, leading to the formation of the final silica shell.

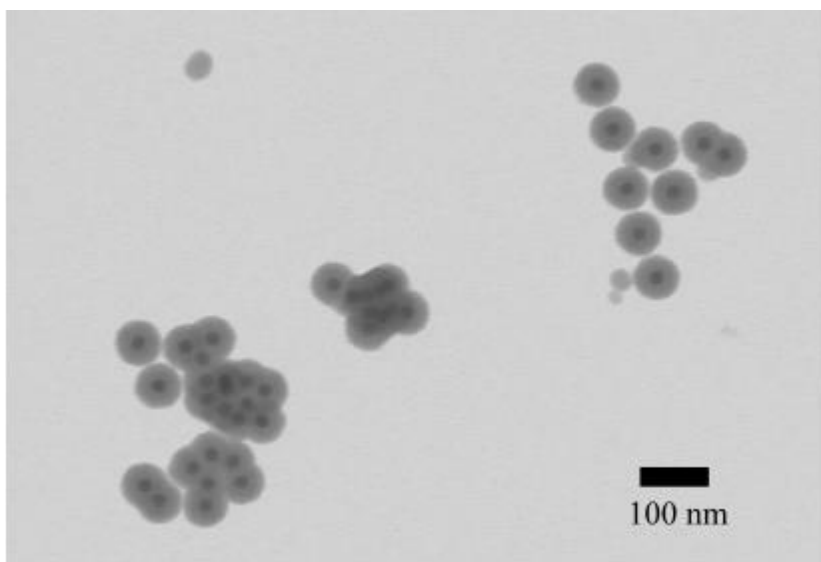


Figure S2: STEM image of UCNPs (sample C2, 20 ± 2 nm diameter) that were coated in a Stöber-like growth process after an initial thin (11 ± 1 nm) silica shell was grown in a reverse microemulsion.

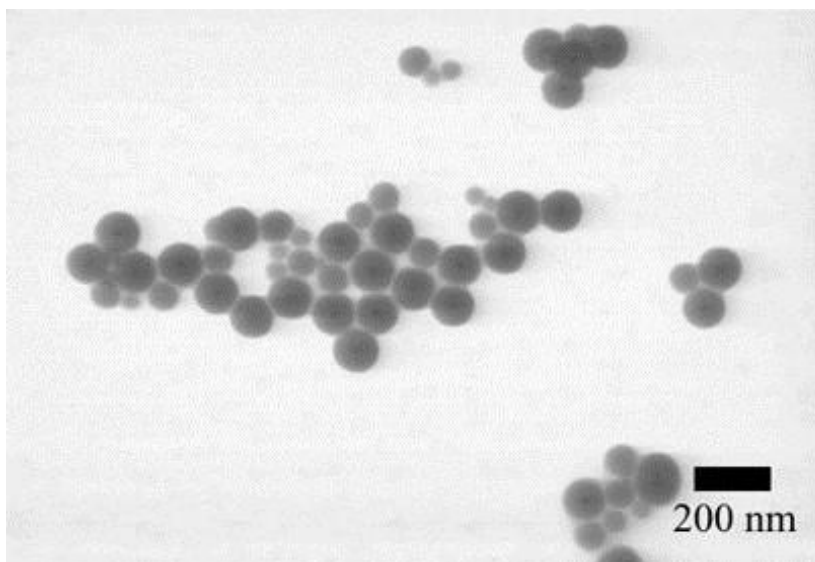


Figure S3: STEM image of UCNPs (sample C1, 24 ± 2 nm diameter) that were coated in a four-step silica shell process in a reverse microemulsion process with an R-value of 1:2.2, which leads to the formation of core-free silica particles due to a too high ammonia water concentration, which accelerates the hydrolysis rate of TEOS. The size of the silica-coated UCNPs was 107 ± 6 nm, and the core-free particles had an average diameter of 60 ± 15 nm.

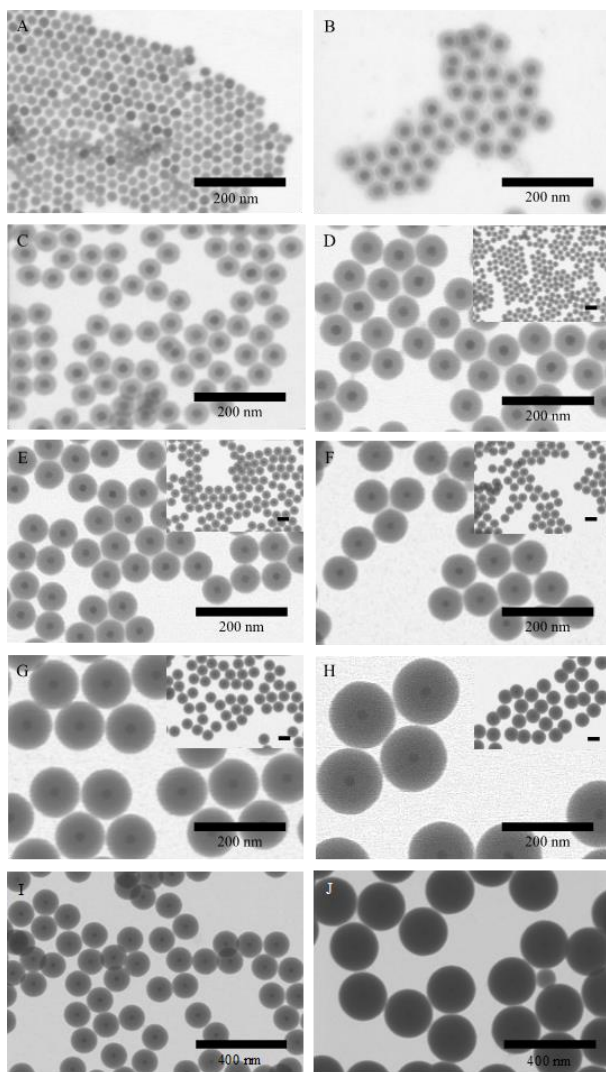


Figure S4: STEM images of oleate-stabilized (A) UCNP cores (sample C2, 20 ± 2 nm diameter) coated by an optimized reverse microemulsion method with (B) one silica shell (sample C2_1S, 11 ± 1 nm thickness), (C) two silica shells (sample C2_2S, 16 ± 1 nm thickness), (D) three silica shells (sample C2_3S, 24 ± 1 nm thickness), (E) four silica shells (sample C2_4S, 31 ± 1 nm thickness), (F) five silica shells (sample C2_5S, 38 ± 1 nm thickness) and (G) six silica shells (sample C2_6S, 43 ± 1 nm thickness). The final seventh layer in the Figures (H), (I) and (J) was grown by a modified Stöber process (sample C2_7Sa, 61 ± 1 nm shell thickness, sample C2_7Sb, 48 ± 3 nm shell thickness, and C2_7Sc, 95 ± 4 nm shell thickness). The scale bar in the insets of panels (D–H) represents 200 nm, while the scale bar in the insets of Figure (I) and (J) represents 400 nm.

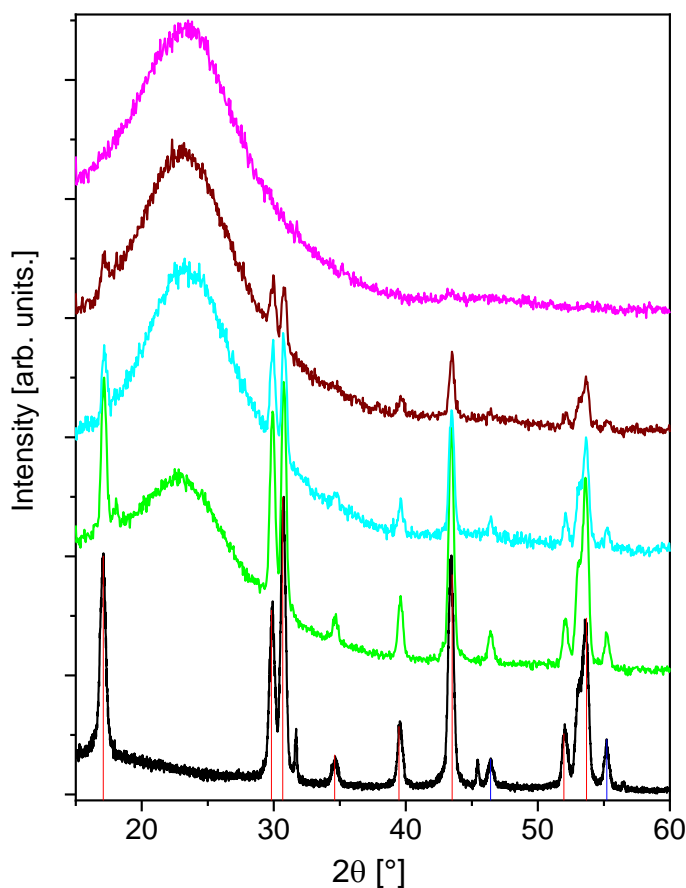


Figure S5: XRD patterns of oleate-coated UNCP cores (24 ± 2 nm diameter, sample C1, black line) where red bars indicate reference values of the hexagonal phase (JCPDS No. 00-028-1192) and blue bars indicate reference values of the cubic phase (JCPDS No. 01-077-2042) and XRD patterns of the same cores after the second silica coating (C1_2S, shell thickness: 18 ± 2 nm, green line), third silica coating (C1_3S, shell thickness 35 ± 2 nm, cyan line), fourth shell silica coating (C1_4S, shell thickness: 44 ± 2 nm, brown line) and fifth silica coating (C1_5S, shell thickness: 149 ± 8 nm, pink line).

References

1. Park, J.; An, K. J.; Hwang, Y. S.; Park, J. G.; Noh, H. J.; Kim, J. Y.; Park, J. H.; Hwang, N. M.; Hyeon, T. *Nat. Mater.* **2004**, *3*, 891–895,
2. Wei, Y.; Lu, F. Q.; Zhang, X. R.; Chen, D. P. *Chem. Mater.* **2006**, *18*, 5733–5737.
3. Na, H.; Woo, K.; Lim, K.; Jang, H. S. *Nanoscale* **2013**, *5*, 4242–4251.

List of Abbreviations

C18TMS	Octadecyltrimethoxysilane
CSU	Cooperative Sensitization Upconversion
CTAB	Cetyltrimethylammonium Bromide
CTAC	Cetyltrimethylammonium Chloride
DLS	Dynamic Light Scattering
DMF	N,N-dimethylformamide
ESA	Excited State Absorption
ETU	Energy Transfer Upconversion
FS	Fluorescence Spectroscopy
ICP-OES	Inductively Coupled Plasma - Optical Emission Spectroscopy
ISA	Ionic Strength Adjuster
ISE	Ion Selective Electrode
IUPAC	International Union of Pure and Applied Chemistry
LEDs	Light Emitting Diodes
MS	Mass Spectrometry
MSN	Mesoporous Nanoparticles
NIR	Near Infrared
PA	Photon Avalanche
PAA	Poly Acrylic acid
PEG-PA	PEO-10-OH-terminated phosphoric acid

SBA-MSN	Santa Barbara Amorphous mesoporous nanoparticles
SEM	Scanning Electron Microscopy
TEM	Transmission Electron Microscopy
TEOS	Tetraethylorthosilicate
TISAB	Total Ionic Strength Adjusted Buffer solution
TMOS	Tertramethoxysilane
UC	Upconversion
UCL	Upconversion Luminescence
UCNP	Upconversion Nanoparticles
UV	Ultra Violet
XPS	X-Ray Photoelectron Spectroscopy
XRD	X-Ray Diffraction

List of Publications

1. **Maysoon I Saleh**, Ihor D Panas, Florian Frenzel, Christian Würth, Bastian Rühle, Yuri L Slominskii, Aleksander Demchenko and Ute Resch-Genger, Sensitization of upconverting nanoparticles with a NIR-emissive cyanine dye using a micellar encapsulation approach. *Methods Appl. Fluoresc.* **2019**, 7, 014003. DOI: 10.1088/2050-6120/aafe1f.
2. Cynthia Kembuan, **Maysoon Saleh**, Bastian Rühle, Ute Resch-Genger and Christina Graf. Coating of upconversion nanoparticles with silica nanoshells of 5–250 nm thickness. *Beilstein J. Nanotechnol.* **2019**, 10, 2410–2421. DOI: 10.3762/bjnano.10.231
3. **Maysoon I. Saleh**, Bastian Rühle, Shu Wang, Jörg Radnik, Yi You and Ute Resch-Genger. Assessing the Protective Effects of Different Surface Coatings on NaYF₄:Yb³⁺, Er³⁺ Upconverting Nanoparticles in Buffer and DMEM. *Sci. Rep.* 10, 19318 (2020). <https://doi.org/10.1038/s41598-020-76116-z>

References

1. U. Resch-Genger and H. H. Gorris, *Anal Bioanal Chem*, 2017, **409**, 5855-5874.
2. F. Wang and X. Liu, *Chem Soc Rev*, 2009, **38**, 976-989.
3. F. Auzel, *Chemical reviews*, 2004, **104**, 139-173.
4. F. C. R. Auzel, *Acad. Sci. (Paris)*, 1966, **262**.
5. N. Menyuk, K. Dwight and J. W. Pierce, *Applied Physics Letters*, 1972, **21**, 159-161.
6. C. S. F. Amitava Patra, Rakesh Kapoor, and Paras N. Prasad, *J. Phys. Chem. B* 2002, **106**, 1909-1912.
7. I. S. a. d. O. a. R Balda, J Fern´andez, J M Fdez-Navarro and M A Arriandiaga, *J. Phys.: Condens. Matter*, 2000, **12**, 10623-10632.
8. A. M. M. D. Barnes, T. Thundat, R. N. Bhargava, V. Chhabra, and B. Kulkarni, *J. Phys. Chem. B* 2000, **104**, 6099-6102.
9. T. Dilbeck and K. Hanson, *J Phys Chem Lett*, 2018, **9**, 5810-5821.
10. S. Hao, Y. Shang, D. Li, H. Agren, C. Yang and G. Chen, *Nanoscale*, 2017, **9**, 6711-6715.
11. Y. Li, L. Zhao, M. Xiao, Y. Huang, B. Dong, Z. Xu, L. Wan, W. Li and S. Wang, *Nanoscale*, 2018, **10**, 22003-22011.
12. J. d. W. Wilfried GJHM van Sark, Jatin K Rath, Andries Meijerink and Ruud El Schropp, *Nanoscale Research Letters*, 2013, **8**.
13. M. Schoenauer Sebag, Z. Hu, K. de Oliveira Lima, H. Xiang, P. Gredin, M. Mortier, L. Billot, L. Aigouy and Z. Chen, *ACS Applied Energy Materials*, 2018, **1**, 3537-3543.
14. J. C. Goldschmidt and S. Fischer, *Advanced Optical Materials*, 2015, **3**, 510-535.
15. B. Zhou, B. Shi, D. Jin and X. Liu, *Nature Nanotechnology*, 2015, **10**, 924-936.
16. C. Zhang, L. Yang, J. Zhao, B. Liu, M. Y. Han and Z. Zhang, *Angew Chem Int Ed Engl*, 2015, **54**, 11531-11535.
17. S. Wen, J. Zhou, K. Zheng, A. Bednarkiewicz, X. Liu and D. Jin, *Nat Commun*, 2018, **9**, 2415.
18. B. J. Park, A. R. Hong, S. Park, K. U. Kyung, K. Lee and H. Seong Jang, *Sci Rep*, 2017, **7**, 45659.
19. S. Plunkett, M. El Khatib, I. Sencan, J. E. Porter, A. T. N. Kumar, J. E. Collins, S. Sakadzic and S. A. Vinogradov, *Nanoscale*, 2020, **12**, 2657-2672.
20. Q. Zhan, H. Liu, B. Wang, Q. Wu, R. Pu, C. Zhou, B. Huang, X. Peng, H. Agren and S. He, *Nat Commun*, 2017, **8**, 1058.
21. A. B. Kostyuk, A. D. Vorotnov, A. V. Ivanov, A. B. Volovetskiy, A. V. Kruglov, L. M. Sencha, L. Liang, E. L. Guryev, V. A. Vodeneev, S. M. Deyev, Y. Lu and A. V. Zvyagin, *Nano Research*, 2019, **12**, 2933-2940.
22. J. Shen, G. Chen, A.-M. Vu, W. Fan, O. S. Bilsel, C.-C. Chang and G. Han, *Advanced Optical Materials*, 2013, **1**, 644-650.
23. H. H. Gorris and U. Resch-Genger, *Anal Bioanal Chem*, 2017, **409**, 5875-5890.
24. J. Liu, C. Li and F. Li, *Journal of Materials Chemistry*, 2011, **21**.
25. S. Alonso-de Castro, E. Ruggiero, A. Lekuona Fern´andez, U. Cossio, Z. Baz, D. Otaegui, V. G´omez-Vallejo, D. Padro, J. Llop and L. Salassa, *Inorganics*, 2019, **7**.
26. B. Del Rosal and D. Jaque, *Methods Appl Fluoresc*, 2019, **7**, 022001.
27. A. N. Generalova, V. V. Rocheva, A. V. Nechaev, D. A. Khochenkov, N. V. Sholina, V. A. Semchishen, V. P. Zubov, A. V. Koroleva, B. N. Chichkov and E. V. Khaydukov, *RSC Advances*, 2016, **6**, 30089-30097.
28. Y. I. Park, K. T. Lee, Y. D. Suh and T. Hyeon, *Chem Soc Rev*, 2015, **44**, 1302-1317.
29. J. Liu, W. Bu, L. Pan and J. Shi, *Angew Chem Int Ed Engl*, 2013, **52**, 4375-4379.
30. F. Wang, D. Banerjee, Y. Liu, X. Chen and X. Liu, *Analyst*, 2010, **135**, 1839-1854.
31. J. Peng, Y. Sun, L. Zhao, Y. Wu, W. Feng, Y. Gao and F. Li, *Biomaterials*, 2013, **34**, 9535-9544.
32. G. Chen, H. Qiu, P. N. Prasad and X. Chen, *Chem Rev*, 2014, **114**, 5161-5214.

33. O. P. Dimitriev, Julia L. Bricks, A. L. Smirnova and Y. L. Slominskii, *RSC Advances*, 2017, **7**, 16126-16130.
34. M. Haase and H. Schäfer, *Angewandte Chemie (International ed. in English)*, 2011, **50**, 5808–5829.
35. A. Speghini, M. Pedroni, N. Zaccheroni, E. Rampazzo and *Synthesis of Upconverting Nanomaterials: Designing the Composition and Nanostructure from: Upconverting Nanomaterials, Perspectives, Synthesis, and Applications*, CRC Press, 2016.
36. G. Chen, H. Qiu, P. N. Prasad and X. Chen, *Chemical reviews*, 2014, **114**, 5161–5214.
37. A. S. Oliveira, M. T. de Araujo, A. S. Gouveia-Neto, J. A. Medeiros Neto, A. S. B. Sombra and Y. Messaddeq, *Applied Physics Letters*, 1998, **72**, 753-755.
38. A. Remillieux and B. Jacquier, *Journal of Luminescence* 1996, **68**, 279-289.
39. S. A. Miller, H. H. Caspers and H. E. Rast, *Physical Review*, 1968, **168**, 964-969.
40. O. S. W. a. H. U. Güdel, *Inorg. Chem.* , 2001, **40**, 5747-5753.
41. S. M. J. a. H. U. GÜDEL, *Journal of Luminescence* 1989, **43**, 125-137.
42. R. Moncorgé, F. Auzel and J. M. Breteau, *Philosophical Magazine B*, 2006, **51**, 489-499.
43. S. García-Revilla, P. Gerner, O. S. Wenger, H. U. Güdel and R. Valiente, *Chemical Physics Letters*, 2005, **401**, 492-496.
44. D. R. G. a. H. U. Güdel, *J. Am. Chem. Soc.* , 1998, **120**, 12143-12144.
45. D. R. G. a. H. U. Güdel, *J. Phys. Chem. B* 2000, **104**, 10222-10234.
46. M. W. a. H. U. Güdel, *J. Phys.: Condens. Matter* 2001, 9583–9598.
47. M. W. a. H. U. Gudel, *Chemical Physics Letters* 1997, **281**, 81–85.
48. S. B. Stefano Polizzi, Adolfo Speghini, Fiorenzo Vetrone, Rafik Naccache, John C. Boyer and John A. Capobianco, *Chem. Mater.* , 2004, **16**, 1330-1335.
49. H. Lai, B. Chen, W. Xu, X. Wang, Y. Yang and Q. Meng, *Journal of Alloys and Compounds*, 2005, **395**, 181-184.
50. S. Heer, K. Kömpe, H. U. Güdel and M. Haase, *Advanced Materials*, 2004, **16**, 2102-2105.
51. X. Wang, R. R. Valiev, T. Y. Ohulchanskyy, H. Agren, C. Yang and G. Chen, *Chem Soc Rev*, 2017, **46**, 4150-4167.
52. G. Chen, W. Shao, R. R. Valiev, T. Y. Ohulchanskyy, G. S. He, H. Ågren and P. N. Prasad, *Advanced Optical Materials*, 2016, **4**, 1760-1766.
53. C. Wurth, M. Kaiser, S. Wilhelm, B. Grauel, T. Hirsch and U. Resch-Genger, *Nanoscale*, 2017, **9**, 4283-4294.
54. M. Kraft, C. Würth, V. Muhr, T. Hirsch and U. Resch-Genger, *Nano Research*, 2018, **11**, 6360-6374.
55. J.-C. G. Bünzli, *Chem. Rev.* , 2010, **110**, 2729–2755.
56. X. Wu, Y. Zhang, K. Takle, O. Bilsel, Z. Li, H. Lee, Z. Zhang, D. Li, W. Fan, C. Duan, E. M. Chan, C. Lois, Y. Xiang and G. Han, *ACS Nano*, 2016, **10**, 1060-1066.
57. H. Soderlund, M. Mousavi, H. Liu and S. Andersson-Engels, *J Biomed Opt*, 2015, **20**, 86008.
58. G. Chen, J. Damasco, H. Qiu, W. Shao, T. Y. Ohulchanskyy, R. R. Valiev, X. Wu, G. Han, Y. Wang, C. Yang, H. Agren and P. N. Prasad, *Nano Lett*, 2015, **15**, 7400-7407.
59. Q. Shao, X. Li, P. Hua, G. Zhang, Y. Dong and J. Jiang, *J Colloid Interface Sci*, 2017, **486**, 121-127.
60. W. Zou, C. Visser, J. A. Maduro, M. S. Pshenichnikov and J. C. Hummelen, *Nature Photonics*, 2012, **6**, 560-564.
61. J. Xu, M. Sun, Y. Kuang, H. Bi, B. Liu, D. Yang, R. Lv, S. Gai, F. He and P. Yang, *Dalton Trans*, 2017, **46**, 1495-1501.
62. G. Shan, R. Weissleder and S. A. Hilderbrand, *Theranostics*, 2013, **3**, 267-274.
63. W. Ren, G. Tian, S. Jian, Z. Gu, L. Zhou, L. Yan, S. Jin, W. Yin and Y. Zhao, *RSC Advances*, 2012, **2**.
64. M. P. Adolfo Speghini, Nelsi Zaccheroni, Enrico Rampazzo and *Synthesis of Upconverting Nanomaterials: Designing the Composition and Nanostructure from: Upconverting Nanomaterials, Perspectives, Synthesis, and Applications*, CRC Press, 2016.
65. Z. Li, Y. Zhang and S. Jiang, *Advanced Materials*, 2008, **20**, 4765-4769.

66. F. Wang, Y. Han, C. S. Lim, Y. Lu, J. Wang, J. Xu, H. Chen, C. Zhang, M. Hong and X. Liu, *Nature*, 2010, **463**, 1061-1065.
67. S. Radunz, A. Schavkan, S. Wahl, C. Würth, H. R. Tschiche, M. Krumrey and U. Resch-Genger, *The Journal of Physical Chemistry C*, 2018, **122**, 28958-28967.
68. S. Wilhelm, M. Kaiser, C. Wurth, J. Heiland, C. Carrillo-Carrion, V. Muhr, O. S. Wolfbeis, W. J. Parak, U. Resch-Genger and T. Hirsch, *Nanoscale*, 2015, **7**, 1403-1410.
69. A. Dong, X. Ye, J. Chen, Y. Kang, T. Gordon, J. M. Kikkawa and C. B. Murray, *J Am Chem Soc*, 2011, **133**, 998-1006.
70. J. Juan, L. Cheng, M. Shi, Z. Liu and X. Mao, *Journal of Materials Chemistry B*, 2015, **3**, 5769-5776.
71. R. Koole, M. M. van Schooneveld, J. Hilhorst, K. Castermans, D. P. Cormode, G. J. Strijkers, C. D. Donega, D. Vanmaekelbergh, A. W. Griffioen, K. Nicolay, Z. A. Fayad, A. Meijerink and W. J. M. Mulder, *Bioconjugate Chem.*, 2008, **19**, 2471-2479.
72. U. Kostiv, O. Janouskova, M. Slouf, N. Kotov, H. Engstova, K. Smolkova, P. Jezek and D. Horak, *Nanoscale*, 2015, **7**, 18096-18104.
73. L. Wang, K. Wang, S. Santra, X. Zhao, L. R. Hilliard, J. E. Smith, Y. Wu and W. Tan, *Anal. Chem.*, 2006, **78**, 646-654.
74. D. P. Ferris, J. Lu, C. Gothard, R. Yanes, C. R. Thomas, J. C. Olsen, J. F. Stoddart, F. Tamanoi and J. I. Zink, *Small*, 2011, **7**, 1816-1826.
75. R. Tapeç, X. J. Zhao and W. Tan, *J Nanosci Nanotechnol*, 2002, **2**, 405-409.
76. D. A. J. Rouquerol, C. W. Fairbridge, D. H. Everett, J. M. Haynes, N. Pernicone, J. D. F. Ramsay, K. S. W. Sing and K. K. Unger, *Pure & Appl. Chem.*, 1994, **66**, 1739-1758.
77. C. Argyo, V. Weiss, C. Bräuchle and T. Bein, *Chemistry of Materials*, 2014, **26**, 435-451.
78. H. S. Qian, H. C. Guo, P. C. Ho, R. Mahendran and Y. Zhang, *Small*, 2009, **5**, 2285-2290.
79. V. K. LaMer and R. H. Dinegar, *J. Am. Chem. Soc.*, 1950, **72**, 4847-4854.
80. H. L. Ding, Y. X. Zhang, S. Wang, J. M. Xu, S. C. Xu and G. H. Li, *Chemistry of Materials*, 2012, **24**, 4572-4580.
81. J. H. Schulman, W. Stoeckenius and L. M. Prince, *J. Phys. Chem.*, 1959, **63**, 1677-1680.
82. T. P. Hoar and J. H. Schulman, *Nature* 1943, **152**, 102-103.
83. F. J. Arriagada and K. Osseo-Asare, *J. Coll. Int. Sci.*, 1999, **211**, 210-220.
84. F. J. Arriagada and K. Osseo-Asare, *Colloid Surf. A-Physicochem. Eng. Asp.*, 1999, **154**, 311-326.
85. K. Osseo-Asare and F. J. Arriagada, *J. Colloid Interf. Sci.*, 1999, **218**, 68-76.
86. K. Osseo-Asare and F. J. Arriagada, *Colloids Surf.*, 1990, **50**, 321-339.
87. T. Nann and P. Mulvaney, *Ang. Chem. Int. Ed.*, 2004, **43**, 5393 - 5396.
88. R. Koole, M. M. van Schooneveld, J. Hilhorst, C. D. Donega, D. C. t Hart, A. van Blaaderen, D. Vanmaekelbergh and A. Meijerink, *Chem. Mater.*, 2008, **20**, 2503-2512.
89. H. L. Ding, Y. X. Zhang, S. Wang, J. M. Xu, S. C. Xu and G. H. Li, *Chem. Mater.*, 2012, **24**, 4572-4580.
90. T. Li, J. Moon, A. A. Morrone, J. J. Mecholsky, D. R. Talham and J. H. Adair, *Langmuir*, 1999, **15**, 4328-4334.
91. M. Darbandi, R. Thomann and T. Nann, *Chem. Mater.*, 2005, **17**, 5720-5725.
92. D. C. Lee, F. V. Mikulec, J. M. Pelaez, B. Koo and B. A. Korgel, *J. Phys. Chem. B*, 2006, **110**, 11160-11166.
93. K. Katagiri, M. Narahara, K. Sako and K. Inumaru, *J. Sol-Gel Sci. Techn.*, 2017, **84**, 110-117.
94. H. Yamada, C. Urata, H. Ujiie, Y. Yamauchi and K. Kuroda, *Nanoscale*, 2013, **5**, 6145-6153.
95. H. Yamada, H. Ujiie, C. Urata, E. Yamamoto, Y. Yamauchi and K. Kuroda, *Nanoscale*, 2015, **7**, 19557-19567.
96. Z. Q. Li, Y. Zhang and S. Jiang, *Adv. Mater.*, 2008, **20**, 4765-+.
97. R. A. Jalil and Y. Zhang, *Biomaterials*, 2008, **29**, 4122-4128.
98. M. A. Malik, M. Y. Wani and M. A. Hashim, *Arabian Journal of Chemistry*, 2012, **5**, 397-417.
99. W. Stöber, A. Fink and E. Bohn, *Journal of Colloid and Interface Science*, 1968, **26**, 62-69.

100. S. Reculosa, C. Poncet-Legrand, S. Ravaine, C. Mingotaud, E. Duguet and E. Bourgeat-Lami, *Chem. Mater.*, 2002, **14**, 2354–2359.
101. K. D. Hartlen, A. P. T. Athanasopoulos and V. Kitaev, *Langmuir*, 2008, **24**, 1714–1720.
102. P. Kipkemboi, A. Fogden, V. Alfredsson and K. Flodström, *Langmuir* 2001, **17**, 5398-5402.
103. D. Zhao, J. Feng, Q. Huo, N. Melosh, G. H. Fredrickson, B. F. Chmelka and G. D. Stucky, *SCIENCE*, 1998, **279**, 548-552.
104. A. Sundblom, A. E. C. Palmqvist and K. Holmberg, *Langmuir*, 2010, **26**, 1983-1990.
105. R. Thahir, A. W. Wahab, N. L. Nafie and I. Raya, *Open Chemistry*, 2019, **17**, 963-971.
106. G. O. d. Magalhães, J. d. O. N. Ribeiro, D. C. L. Vasconcelos and W. L. Vasconcelos, *Materials Research*, 2018, **21**.
107. W. Fan, B. Shen, W. Bu, F. Chen, Q. He, K. Zhao, S. Zhang, L. Zhou, W. Peng, Q. Xiao, D. Ni, J. Liu and J. Shi, *Biomaterials*, 2014, **35**, 8992-9002.
108. J. Liu, W. Bu, S. Zhang, F. Chen, H. Xing, L. Pan, L. Zhou, W. Peng and J. Shi, *Chemistry*, 2012, **18**, 2335-2341.
109. C. Li, J. Liu, S. Alonso, F. Li and Y. Zhang, *Nanoscale*, 2012, **4**, 6065-6071.
110. C. Li, D. Yang, P. Ma, Y. Chen, Y. Wu, Z. Hou, Y. Dai, J. Zhao, C. Sui and J. Lin, *Small*, 2013, **9**, 4150-4159.
111. Q. Xiao, Y. Li, F. Li, M. Zhang, Z. Zhang and H. Lin, *Nanoscale*, 2014, **6**, 10179–10186.
112. W. Feng, X. Zhu and F. Li, *NPG Asia Materials*, 2013, **5**, e75-e75.
113. H. H. Itoh Hisako, Tsuchiya Masashi, Suzuki Yasuo, Asano Yasukazu *Bulletin of the Chemical Society of Japan*, 1984, **57**, 1689-1690.
114. D. Lisjak, O. Plohl, M. Ponikvar-Svet and B. Majaron, *RSC Advances*, 2015, **5**, 27393-27397.
115. O. Dukhno, F. Przybilla, V. Muhr, M. Buchner, T. Hirsch and Y. Mely, *Nanoscale*, 2018, **10**, 15904-15910.
116. O. Plohl, S. Kralj, B. Majaron, E. Frohlich, M. Ponikvar-Svet, D. Makovec and D. Lisjak, *Dalton Trans*, 2017, **46**, 6975-6984.
117. O. Plohl, M. Kraft, J. Kovac, B. Belec, M. Ponikvar-Svet, C. Wurth, D. Lisjak and U. Resch-Genger, *Langmuir*, 2017, **33**, 553-560.
118. E. Palo, S. Lahtinen, H. Pakkila, M. Salomaki, T. Soukka and M. Lastusaari, *Langmuir*, 2018, **34**, 7759-7766.
119. S. Lahtinen, A. Lyytikäinen, H. Päckilä, E. Hömppi, N. Perälä, M. Lastusaari and T. Soukka, *The Journal of Physical Chemistry C*, 2016, **121**, 656-665.
120. O. Barbier, L. Arreola-Mendoza and L. M. Del Razo, *Chemico-biological interactions*, 2010, **188**, 319–333.
121. Q. Xiao, Y. Li, F. Li, M. Zhang, Z. Zhang and H. Lin, *Nanoscale*, 2014, **6**, 10179-10186.
122. R. Arppe, I. Hyppänen, N. Perala, R. Peltomaa, M. Kaiser, C. Wurth, S. Christ, U. Resch-Genger, M. Schaferling and T. Soukka, *Nanoscale*, 2015, **7**, 11746-11757.
123. C. Wurth, S. Fischer, B. Grauel, A. P. Alivisatos and U. Resch-Genger, *J Am Chem Soc*, 2018, **140**, 4922-4928.
124. A. Bogner, P. H. Jouneau, G. Thollet, D. Basset and C. Gauthier, *Micron*, 2007, **38**, 390-401.
125. M. M. Modena, B. Ruhle, T. P. Burg and S. Wuttke, *Adv Mater*, 2019, **31**, e1901556.
126. B. J. Inkson, in *Materials Characterization Using Nondestructive Evaluation (NDE) Methods*, 2016, DOI: 10.1016/b978-0-08-100040-3.00002-x, pp. 17-43.
127. C. Urban and P. Schurtenberger, *JOURNAL OF COLLOID AND INTERFACE SCIENCE* 1998, **207**, 150–158.
128. R. Pecora, *Journal of Nanoparticle Research*, 2000, **2**, 123–131.
129. E. J. Cho, H. Holback, K. C. Liu, S. A. Abouelmagd, J. Park and Y. Yeo, *Mol Pharm*, 2013, **10**, 2093-2110.
130. R. Herrmann and C. Onkelinx, *Pure and Applied Chemistry*, 1986, **58**, 1737-1742.
131. J.R.Albani, in *Structure and Dynamics of Macromolecules: Absorption and Fluorescence Studies*, Elsevier Science, 2004, DOI: <https://doi.org/10.1016/B978-0-444-51449-3.X5000-X>, ch. Chapter 2 pp. 55-98.

132. J. R. Lakowicz, *Principles of Fluorescence Spectroscopy*, Springer Singapore, Third Edition edn., 2006.
133. F. Wang, J. Wang and X. Liu, *Angew Chem Int Ed Engl*, 2010, **49**, 7456-7460.
134. S. Ghosh, V. L. Prasanna, B. Sowjanya, P. Srivani, M. Alagaraja and D. D. Banji1, *Asian J. Pharm. Ana.* , 2013, **3**, 24-33.
135. A. J. Bard and L. R. Faulkner, *ELECTROCHEMICAL METHODS Fundamentals and Applications*, JOHN WILEY & SONS, INC., New York, second edition edn., 2001.
136. M. AG, Ion-selective electrodes (ISE)_Manual, <https://www.metrohm.com/en-us/products-overview/60502150?from>, 2020).